

Incorporation of Mn into Ge Quantum Dots: Growth Strategies to Control Structure and Magnetism

A Dissertation

Presented to
the faculty of the School of Engineering and Applied Science
University of Virginia

in partial fulfillment
of the requirements for the degree

Doctor of Philosophy

by

Christopher A. Nolph

May

2012

APPROVAL SHEET



The dissertation
is submitted in partial fulfillment of the requirements
for the degree of
Doctor of Philosophy


AUTHOR

The dissertation has been read and approved by the examining committee:

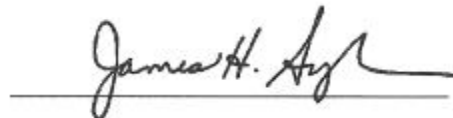

Advisor





Accepted for the School of Engineering and Applied Science:



Dean, School of Engineering and Applied Science

May
2012

Abstract

Dilute magnetic semiconductors are important building blocks towards the realization of low power, low thermal loss spintronics based devices. In this work, group IV based dilute magnetic semiconductors are investigated for their potential to function at temperature above room temperature and compatibility with the current microelectronics industry. The goal of this work is to understand and control the Mn environment within the Si(100), Ge wetting layer and Ge quantum dot (QD) systems and how it influences the magnetic properties. The combination of quantum confinement from the quantum dots and carrier mediated ferromagnetism make these structures of particular interest, but the materials related challenges are considerable and are the focal point of this work.

We investigated three methods for Mn doping of Ge QDs with the goal to overcome low solid solubility of Mn in Ge and suppress unwanted secondary phases, i.e. Mn germanides. The first method investigates the stability and evolution of Mn nanostructures on a Si(100)2x1 reconstructed surface as a function of annealing temperature up to temperatures typical for Ge QD growth. Annealing the Mn-Si(100)2x1 sample to a temperature of $316^{\circ}\text{C} \pm 38^{\circ}\text{C}$ yields a structure characteristic of Mn doping in Si sub-surface substitutional sites. The second method uses a surface driven approach: Mn is deposited on the Ge QD surface, forms well-defined islands on the QD and wetting layer surface and their behavior during *in-situ* annealing is studied in detail. The as deposited Mn structures on Ge QDs were investigated using tunneling spectroscopy techniques and found to strongly interact with the underlying Ge. The third method utilized the co-deposition of Ge and Mn (i) only during the formation of the wetting layer, and (ii) throughout the entire QD growth process. The highest concentration of Mn studied was approximately 23%, which results in only minor perturbations in the Ge QD growth albeit Mn

germanides or Mn-Si-Ge ternary compounds form. All processes are observed with scanning tunneling microscopy, which yields topographic and electronic structure information of the reaction sequence. Room temperature magnetism results from one particular sample ($\text{Mn}_{0.05}\text{Ge}_{0.95}$ QD), obtained with a vibrating sample magnetometer and x-ray circular dichroism, indicates a ferromagnetic material with a Curie temperature above room temperature. Other co-deposited samples with Ge capping layers and increasing Mn concentrations, 8 % and 10 %, had Curie temperatures around 50 K.

Acknowledgements

First and foremost, I'd like to acknowledge the excellent mentorship I received from my advisor, Petra Reinke. Through the years Petra has provided me with fruitful discussions on my research projects, a helping hand in the lab when needed, and helpful commentary on my writing, pointing out my interesting sentence constructions. I feel fortunate for the opportunities for travel that Petra has been able to provide for research and conferences from Berkeley to Sweden. The time I have spent in Petra's research group has turned out to be a wonderful chapter in my life.

I would also like to acknowledge my labmates, some who have since left UVA. My labmates have proven to be excellent colleagues and friends and I appreciate the time I have had to spend with them, whether working or unwinding. My labmates whom I would like to thank are: Harmonie, Kiril, Sarah, Hui, Michael, Wenjing, Jeremy, Gopal, Brandon, Matt, and Rebecca. Being among the few UHV groups in the Materials Science and Engineering Department, the need for copper gaskets and other vacuum parts along with discussing technical issues extends the research family to a few other groups. The colleagues that I would like to thank include: Petz, Joseph, Duska, Matt, Ryan, Cathy, Cope, and Jacob.

In addition, I'd like to acknowledge other friends at UVA and beyond for their support. My family has been a constant presence of support and encouragement and there are few words to describe my gratitude. I'm especially grateful that, throughout the years, I wasn't asked *too* often when I was going to graduate and get a real job.

Table of Contents

Chapter 1. Introduction.....	1
1.1. Motivation.....	1
1.2. Project Overview	3
1.3. Materials Background.....	6
1.3.1. The Si(100) Surface and (2x1) Reconstruction.....	6
1.3.2. Formation of Wire Structures on Si(100)2x1.....	8
1.3.3. Heteroepitaxy and the Formation of Ge Quantum Dots	9
1.3.4. Dilute Magnetic Semiconductors	12
Chapter 2. Experimental Techniques.....	15
2.1. Scanning Tunneling Microscopy	15
2.2. Scanning Tunneling Spectroscopy.....	19
2.3. Ultra-High Vacuum Chamber.....	20
2.4. Si(100) Sample Preparation	22
2.5. Deposition Sources	24
2.6. Synchrotrons and X-ray/Ultraviolet Photoemission Spectroscopy.....	25
2.7. X-ray Absorption Spectroscopy and X-ray Magnetic Circular Dichroism	26
2.8. Vibrating Sample Magnetometry.....	29
2.9. Scanning Auger Microscopy: Scanning Electron Microscopy and Auger Electron Spectroscopy	31
Chapter 3. Mn Wires: Structure and Temperature Stability	35
3.1. Experimental and Modeling Details	36
3.2. Mn Wire Structure	40
3.3. Mn Wire Temperature Evolution.....	46
3.3.1. Silicon Surface	47
3.3.2. Manganese Surface Structures	52
3.4. Discussion	54
3.4.1. Mn Wire Structure.....	54
3.4.2. Temperature Evolution: Silicon Surface	56
3.4.3. Temperature Evolution: Manganese Surface Structures	57
3.5. Summary	59
Chapter 4. X-ray Photoelectron Spectroscopy of Mn Overlayers on Si(100)2x1 and a-Si.....	61
4.1. Experimental Details.....	61
4.2. Mn overlayers on Si(100)2x1	63

4.3.	Mn overlayers on a-Si.....	69
4.4.	Discussion.....	73
4.5.	Summary.....	76
Chapter 5. Mn Islands on Ge Quantum Dots.....		77
5.1.	Experimental Details.....	77
5.2.	GeQDs and Mn Islands: As Deposited	79
5.3.	GeQDs and Mn Islands: Temperature Evolution.....	82
5.4.	GeQDs and Mn Islands: Scanning Tunneling Spectroscopy	86
5.5.	Discussion.....	89
5.6.	Summary.....	92
Chapter 6. $\text{Mn}_x\text{Ge}_{(1-x)}$ Quantum Dots: Co-deposited Nanostructures and Magnetic Properties		94
6.1.	Experimental Details.....	94
6.2.	STM Results of Growth.....	96
6.3.	SAM Results of Growth.....	99
6.4.	Magnetism Results: VSM and XMCD	104
6.5.	Discussion.....	105
6.6.	Summary.....	108
Chapter 7. Concluding Remarks.....		110
7.1.	Conclusions.....	110
7.2.	Suggested Work.....	112
References.....		115

List of Figures

Figure 1.1. Schematic of (a) an ideal Si(100)1x1 surface and (b) a Si(100)2x1 surface. The topmost atoms are shaded grey and the unit mesh for each configuration is highlighted by the dotted line.....	6
Figure 1.2. STM image of a thermally cleaned Si(100) displaying the 2x1 reconstruction, alternating directions of dimer rows, terraces and step edges. Image acquired with a sample bias of -1.5 V.	7
Figure 1.3. Schematic representing three growth modes of a film as a function of coverage (θ). (a) Layer-by-layer growth or Frank-van der Merve. (b) Layer-plus island growth or Stranski-Krastanov. (c) Island growth or Volmer-Weber). [44].....	10
Figure 1.4. STM images of a Ge QD (a) pyramid, (b) dome, and (c) superdome. Note the exaggerated z-scale. [45]	11
Figure 2.1. Diagram of a one-dimensional tunneling junction. The wave functions of the tip and sample overlap when separated by a distance, s . With the application of a sample bias, V , electrons are able to tunnel into the empty states of the sample. The potential barrier is in most cases representable by the work function, ϕ . [83].....	16
Figure 2.2. STM images of the GaAs(110) surface acquired at samples biases of (a) +1.9 V (empty states) and (b) -1.9 V (filled states). (c) The top view model of the GaAs(110) surface atoms. In the empty state image the contrast comes from the Ga atoms and in the filled state image the As atoms are the source of the contrast. [19,86]	17
Figure 2.3. Diagram of a scanning tunneling microscope. X-Y piezoelectric scanners move the tip laterally across the surface during imaging. In constant current mode, the Z piezoelectric adjusts the height of the tip from the sample based on the change in current via the feedback loop [83].....	18
Figure 2.4. Images of our Omicron UHV chamber. Shown in the images are the following components: (1) the bell jar which houses the STM, (2) a spherical chamber with the deposition sources attached, (3) 4-axis manipulator which extends into the spherical chamber, (4) turbomolecular pump, (5) rotary vane backing pump, and (6) the passive air legs for vibration dampening. The ion pump, not pictured, is located within the table.	21
Figure 2.5. Images of the direct current sample holder. The sample holder is shown fully assembled. (1) The contact bars used to make electrical contact to the Si sample within the chamber. (2) The ceramic top plate which helps to hold the sample in place with (3) four molybdenum studs and nuts to clamp (4) the sample.	22
Figure 2.6. Schematic depicting the electronic transitions from a $2p_{3/2}$ level of a 3d ferromagnetic material for two opposing magnetization directions and for zero magnetization. [90]	27

Figure 2.7. $L_{3,2}$ -edge XAS and XMCD spectra of iron: (a) XMCD spectra, solid line, of iron along with the integrated data, dotted line. The points where p and q are found is illustrated. (b) XAS spectra, solid line, of iron and the integrated data, dotted line, with r illustrated. [91]	28
Figure 2.8. (a) Schematic of a vibrating sample magnetometer (VSM) and (b) a diagram illustrating the geometry of the VSM within the Dewar. [99]	30
Figure 2.9. (a) A diagram illustrating the interaction volume from an electron beam. The regions where the secondary and backscattered electrons and x-rays is indicated. (b) The energy spectrum of the electrons emitted from a specimen surface. [101]	31
Figure 2.10. Diagram for the Auger process for a (a) $KL_1L_{2,3}$ transition and (b) $L_{2,3}VV$ transition. [19,102]	32
Figure 3.1. Temperature measurement of a sacrificial sample as a function of the current/power supplied to the sample. The sacrificial sample had a resistance across the sample holder of 104.9 Ω , and a visual deep red glow at the sample was observed at 415°C.	37
Figure 3.2. A diagram illustrating a step edge with kinks. A straight, unkinked, section of the step edge is measured and represented by n_0 . A negative kink, one protruding into the step edge, is measured and represented by n_r	39
Figure 3.3. (a) The height of the Mn-wires is depicted as a function of bias voltage [empty (+) and filled states (-)]. The height is given with respect to the plan of the Si-dimers. The graph contains data from images measured in two independent experiments and the deviations between these two datasets is included in the error bar. In the region between 0.7 V and -1.1 V the image quality is insufficient to determine the Mn-wire height. (b) and (c) are representative experimental STM images for 0.7 V and -1.5 V; the wires are outlined with a box. Part (d) shows a larger scale image of Mn-wires on the Si(100)2x1 surface.	40
Figure 3.4. (a) Mn wire and (c) linescans across Si-dimer rows (red) and Mn-wire (green), which illustrates the lack of an offset between the Si-dimer rows and the Mn-wire maxima. (b) STM image of a Mn wire with an offset between the Mn wire and the Si dimers, the corresponding linescan shown in (d). An exceptionally well resolved Mn wire is shown in the inset of (b). All images at an imaging bias of -1.5V.	41
Figure 3.5. Distribution of wire offset for 37 wires from two independent experiment (“wire set 1”, “wire set 2”). The data point at 0 nm offset are Mn wires whose maxima are in registry with the Si dimer rows. The set of data point centered at 0.25 nm corresponds to the mean offset of Mn wire maximas relative the Si dimers. The error in the measurement is estimated to be about ± 0.02 nm.	42
Figure 3.6. Simulated filled state STM images for a sample bias of -1.1 V for two Mn wire structures: (a) Mn in a subsurface and cave positions (sub-cave) and (b) Mn in hollow and cave positions (hollow-cave). The ball-and-stick models with Mn (blue circles) and Si (green circles) are seen as an overlay on the simulated STM images. A side view of the model is shown below (a) and (b) for each structure.	43

Figure 3.7. A schematic of the Si(100) surface (open circles) and the possible binding sites for Mn (filled circles) is illustrated. (a) A top down view of the Si(100)2x1 surface where Mn is located in a dimer vacancy (D), substitutional (S), a dimer long bridge (M), hollow (H) and a dimer short bridge (B) site. (b) A side view of the Si(100)2x1 surface and possible Mn binding sites. The cave site (C) is located between dimer rows and the interstitial site (I_1) sites one layer below the surface. The other two interstitial sites ($I_{2,3}$) are located within the third layer below the surface. (c) Depicts the displacement of a Si atom in the event of Mn entering a substitutional site [118]. 44

Figure 3.8 A summary of line scans across simulated structures are shown here. In (a) the top-down ball and stick model of the hollow-cave structure on Si(100) is shown. The associated line scans run perpendicular to the Mn wire structure and intersect with the respective Mn site. In (b) the line scans intersect with the cave site of the hollow-cave structure. The line scans are shown for different simulated bias voltages (top to bottom) from 1.3 V to 0.5 V in 0.2 V increments. Similarly in (c) line scans intersecting with the hollow site Mn is shown. In (d) the top-down ball and stick model for the sub-cave structure on Si(100) is shown. The line scans intersecting the (e) cave site Mn and (f) subsurface site Mn show varying simulated bias voltage (top to bottom) from 1.1 V to 0.5 V 45

Figure 3.9. (a) Change in defect morphology characterized by defect number density and percent area covered by defects. The area enclosed by the box contains the measurements for the Si(100)2x1 surface before and after room temperature Mn-deposition. (b) Average defect size as a function of annealing temperature. A single dimer vacancy occupies an area of $0.309 \pm 0.028 \text{ nm}^2$. STM images of representative defect structures observed after annealing: (c) S268, (d) S316, and (e) S415. These defect images show the filled states (-1.5 V bias voltage). 47

Figure 3.10. STM images of Si(100)(2x1) - Mn samples (a) before annealing of sample S316, after annealing: (b) S115 (-1.5 V), (c) S268 (-1.5 V), (d) S316 (+1.5 V), and (e) S415 (-1.5 V bias). All images acquired at room temperature. 48

Figure 3.11. Representative STM images of the two high temperature samples (a) S600 and (b) SH600. 49

Figure 3.12. (a) The average number of dimers between kinks along an S_A and S_B type step edge. (b) Step edge formation energy of S_A and S_B steps as a function of the sample annealing temperature. The data point at 25°C corresponds to a representative clean Si(100)(2x1) surface after *in-situ* cleaning. 52

Figure 3.13. (a) STM image of S316 after annealing. The large image shows the empty states (+1.5V), and the inset depicts the filled state (-1.5V) image for the same area. (b) Representative line scan across a high contrast region, where the reconstruction is preserved and the apparent height is modified. The change in apparent height is indicative of subsurface Mn, which acts as an electronically active dopant. (c) Line scans across a region without enhanced contrast: the broken line is perpendicular to the dimer rows, the solid line crosses two dimer vacancy defects. The arrow marks a C-type defect. 53

Figure 4.1. (a) Si 2p core level for the Si(100)2x1 surface, and after the Si2p after the deposition of Mn are shown. The results of the fit procedure are included and the labels of the

peaks are indicated in the figure. The LEED pattern of the Si-surface is shown as an inset and confirms the presence of the (2x1) reconstruction. A second inset shows the STM image measured after the deposition of 1.2 ML of Mn on Si, which was described in detail in a recent publication. (b,c) The area of all fit-curves is shown before and after the deposition of Mn. (d) The respective Mn3p peak is shown at the bottom. 64

Figure 4.2. The VB spectra for the Si(100)(2x1) surface and the surface after the deposition of Mn are shown as a function of the angle between surface normal and analyzer. The inset illustrates the geometry for an angle of 0°. 65

Figure 4.3. The VB spectra after the deposition of Mn as a function of the photon energy. An intense Fermi edge is present and confirms the metallic nature of the overlayer. 66

Figure 4.4. (a) Si 2p spectra and the resulting fitted peaks. The Si 2p peak is shown for 3 different states of the sample: (1) Si-substrate after Ar sputtering, (2) after 1 ML Mn deposition, and (3) after 10 ML Mn deposition. (b) The valence band spectra as a function of Mn coverage at an energy of 160 eV. 68

Figure 4.5. (a) Si 2p core level as a function of Mn deposition. Spectra obtained at 150 eV for the no Mn core level and 160 eV for all others. (b) Mn 3p level as a function of Mn deposition. All spectra obtained at 160 eV. 71

Figure 4.6. VB spectra depicting the energy dependence of the VB for two Mn depositions: (a) 1 ML and (b) 10 ML. 72

Figure 5.1. STM images of the Ge(100) wetting layer (a) prior to Mn deposition and (b) after Mn deposition. (c) Line scans from (a) and (b) were taken from representative areas on each image and are indicated by the black bar within each image. Both line scans are shown on the same scale for comparison. In (c) the dotted line represents the line scan from (b) and the solid line from (a). Both images were obtained with a sample bias of -2.0 V. 79

Figure 5.2. STM images of a single Ge QD (a) prior to Mn deposition and (b) a smaller scale image of a QD facet containing an overlay of the Ge(105) 2x1 rebonded step reconstruction. A second STM image of a Ge QD (c) after Mn deposition containing Mn islands decorating the facets and facet edges of the QD and (d) a smaller scale image of a QD facet with an overlay of the Ge(105) 2x1 rebonded step reconstruction. All images were obtained with a sample bias of -2.0 V. 80

Figure 5.3. (a) The number density of Mn islands on Ge QDs facets and facet edges is plotted and how it varies with increasing annealing temperature from room temperature to 150°C. (b) Mn island average size (left axis) and average height (right axis) are shown as a function of annealing temperature from room temperature to 150°C. (c) Distribution of Mn island size at room temperature compared to the island size distribution between 60°C and 150°C. (d) Distribution of Mn island height at temperature compared to the island height distribution between 120°C and 150°C. 82

Figure 5.4. The volume of the Mn islands represented as (a) distributions at room temperature and 150°C, and (b) as a function of annealing temperature. In (b) the left axis and gives the

average island volume and the right axis gives the total Mn island volume normalized to the image area.	83
Figure 5.5. STM image of sample annealing temperatures at (a) 340°C, (b) 375°C, and (c) 405°C show Ge QDs alongside secondary structures. In (a) secondary structures are noted by an arrow. All images were obtained with a sample bias of -2.0 V.	84
Figure 5.6. A collection of STM images at varying sample biases of the same two Mn islands on a Ge QD (105) facet. The sample biases are as follows: (a) -1.4 V, (b) -1.6 V, (c) -1.8 V, (d) -2.0 V, (e) +1.6 V, (f) +1.8 V, and (g) +2.0 V.	86
Figure 5.7. (a) An STM image with points marked where spectroscopy was measured. Point spectroscopy of (b) Ge QDs and WL before Mn deposition, (c) Ge QDs, WL, and Mn after Mn deposition, and (d) Ge QDs, and Mn islands after anneal.	88
Figure 6.1. Several STM images of co-deposited Ge and Mn after 1.5 ML to 2 ML are shown. Mn concentrations of (a) 5 %, (b) 10 % and (c,d) 23%. All images were acquired with an imaging bias of -2.0 V.	96
Figure 6.2. Several STM images of co-deposited Ge and Mn after 4.5 ML deposition are shown. Mn concentrations of (a) 8 %, (b) 10 % and (c,d) 23%. All images were acquired with an imaging bias of -2.0 V.	97
Figure 6.3. Plot of the average volume of QDs (left axis, green data points) and QD density (right axis, red data points) as a function of Mn concentration.	98
Figure 6.4. SEM images acquired at an acceleration voltage of 10 kV and probe current of 1.0 nA. Two Mn concentrations are shown: (a) 18 % Mn and (b) 28 % Mn.	100
Figure 6.5. SEM image acquired at 10 kV with a probe current of 1.0 nA. The Mn concentration is 28 %. The three points indicated by their markers represent the points of interest selected to perform point Auger electron spectroscopy.	101
Figure 6.6. The (a) Ge LMM and (b) Mn MNN Auger peaks are shown for “point 3.” These two peaks are representative for other peaks used in the calculation of the Mn concentration of secondary structures. (c) The Mn concentration is plotted as a function of the selected point. .	102
Figure 6.7. (a) VSM M-H loops (± 2 T) of 8 %, 10 %, and 23 % Mn capped samples at 5 K. (b) VSM M-H loops for (± 2 T) of 23 % Mn capped sample at 5 K and 300 K. (c) VSM M-H loops (± 0.8 T) of 5 % Mn capped sample at 5 K and 300 K.	103
Figure 6.8. (a) XAS of the Mn 2p absorption peak. (b) XMCD of the Mn 2p absorption peak obtained at 30 K and 300 K.	104
Figure 6.9. (a) Based on the known volume of material deposited and the volume of the QDs from STM images, the fraction of Ge in the secondary phases can be estimated. (b) A comparison between the known number of Mn atoms deposited as a function of Mn concentration and the number of Mn atoms required to form a stoichiometric Mn-Ge intermetallic compound.	107

List of Tables

Table 3-A List of sample parameters.....	38
Table 3-B Dimer interaction energies of S_A and S_B step edges	50
Table 4-A List of peak positions resulting from the fit procedure as a function of Mn deposition coverage. Peaks are denoted by their relative position to the Si 2p $3/2-1/2$ peak.....	70

Chapter 1. Introduction

1.1. Motivation

The world of microelectronics has seen much in the way of rapid growth that is not seen in other industries; Gordon Moore predicted this rapid growth in 1965. Moore's Law has continued to hold since the original publication in 1965. Moore originally noticed that the number of components doubled every two years from a few data points between 1958 and 1965 though it is interesting to note that Moore only expected the trend to hold for 10 years [1]. The transistor is one component in microelectronics that manufacturers and researchers have worked to shrink in feature size and squeeze more transistors into a given area. The field effect transistor (FET) has changed very little until recently when Intel introduced a three-dimensional FET that protrudes from the surface like a fin or FinFET. The FinFET does represent a more radical change in transistor design but feature sizes, such as the insulating layer, have undergone less and less significant changes in recent years. However, the challenges that are present to achieve high yield, improved performance and shrinking features sizes make the continued pursuit of traditional electronics an increasingly costly and difficult endeavor.

Researchers in industry, academia and national labs are pursuing alternatives to traditional electronics. Spin-based electronics or spintronics is one alternative to traditional electronics capable of lowering power requirements and reducing heat contributions of operation while integrating well with charge-based electronics. Spintronics aims to use the spin degree of freedom of the electron to convey information in a logic switch or with memory applications [2–4]. One of the basic components towards the realization of spintronics are dilute magnetic semiconductors (DMS), or semiconductors with magnetic dopants where the ferromagnetism is mediated by carriers [5–7]. Ferromagnetism that is mediated by carriers allows for the control of

the magnetism with an electric field in a highly versatile manner. The research field is more mature for magnetic dopants in group III-V semiconductors as opposed to group IV DMS [5,8–13]; however, group IV based DMS promises better compatibility with the current Si based microelectronics industry. Silicon in particular is an attractive host to a DMS due to long spin lifetimes [14]. In addition, the electronic confinement of quantum dots is theoretically predicted to increase the Curie temperature as opposed to group IV thin film DMS materials [15]. Although theoretical predictions for these confined magnetically doped structures are promising, the experimental realization of these structures and properties meets many challenges in materials science and synthesis. In that regard we seek to understand the interaction between the constituents, Ge-Mn-Si, at conditions required for growing QDs and characterize the magnetic properties of the resulting structures.

In the pursuit of doping Ge QDs with Mn, several approaches have been devised to accomplish this goal. Several challenges have to overcome to accomplish the goal of doping Ge QDs with Mn, and the methods devised in this research were designed to investigate these challenges. One such challenge is achieving substitutional doping of Mn in Ge and ideally doing so only within the QDs and not the wetting layer. Another challenge is the growth temperature required to form quantum dots is sufficiently high enough to produce Ge-Mn intermetallic compounds which are counterproductive to doping. The first method consists of incorporation of Mn into Si sub-surface sites through an understanding of Mn nanostructures and their interaction with Si(100) at elevated annealing temperatures. With Mn entrapped in sub-surface sites, it can be incorporated during the growth of Ge QDs and can act as a surfactant, preferring the newly forming sub-surface sites at the growth front. The underlying hypothesis is that some Mn will remain in the substitutional sites within the wetting layer and quantum dots. The second method

consists of the room temperature deposition of Mn onto *in-situ* grown Ge QDs and low temperature annealing to study behavior of Mn adatoms on the Ge surface and ideally the movement of Mn into the QD. The third method requires the co-deposition of Ge and Mn during the growth of Ge QDs on a Si(100) substrate held at temperatures typically used for Ge QD growth.

1.2. Project Overview

The first route of Mn incorporation discussed is Mn entrapment at the Si-Ge interface through tuning the Mn-Si bonding with annealing of Mn nanostructures. The first part of this investigation consists of Mn self-assembled wires on Si(100)2x1 reconstructed surface as a starting point for experiments. At room temperature, Mn self-assembles into wires perpendicular to the Si dimer rows when deposited onto an optimally clean Si(100)2x1 surface. However, to understand this structure further, a follow up of image analysis is performed to reveal the nature of the sub-structure of the Mn wires and the bonding of Mn to the Si surface, as discussed in Chapter 3. The Mn wires were characterized by the position of apparent height maxima relative to the Si dimer rows and by an abrupt change in apparent height at a specific gap voltage tunneling into the empty states of the sample. A collaborative effort to describe our experimental results using density functional theory (DFT) modeling has not yet been able to capture fully all experimental observations with simulated STM images. However, the models obtained from DFT are the best fit to our experimental data to date. An experiment only structural analysis of the Mn wires is published in Surface Science [16].

With the sub-structure of the Mn wires characterized, the stability of these structures with increasing annealing temperatures is investigated see Chapter 3. The importance of the stability of the Mn wires is investigated to determine the viability for subsequent Ge QD growth. The Mn

wires were found to be unstable at mild increases in temperature and decompose into clusters. The most notable structure observed Mn was no longer evident on the surface but high contrast regions on the Si(100)2x1 surface appeared only in empty state images. These experimental observations strongly indicate that Mn moved into a sub-surface substitutional site as a dopant (acceptor). Further increases in temperature, up to the temperature regime typically used for Ge QD growth, leads to the formation of Mn silicides on the surface. The study of the temperature stability of the Mn wires is published in the Journal of Physical Chemistry C [17].

In addition to STM investigations, Mn layers and their bonding to Si were also investigated using XPS at the National Synchrotron Light Source and Brookhaven National Laboratory (BNL). On two, separate visits to BNL, Mn overlayers on Si(100)2x1 (see Chapter 4) and a-Si were investigated. Mn on Si(100)2x1 XPS results indicated the formation of a Mn-Si interface followed by the appearance of a Mn layer. The results indicated that α -Mn forms on top of the original Mn-Si layer. The study of Mn on Si(100)2x1 by XPS is published in Applied Surface Science [18].

The second route that was pursued to achieve Mn-doped Ge QDs is the room temperature deposition of Mn on top of Ge QDs followed by mild annealing steps to activate Mn sub-surface bonding sites of the Ge QDs (see Chapter 5). On a Ge QD/Si(100) substrate held at room temperature, sub-monolayer deposits of Mn forms flat islands on the QD facets on the order of 2 nm across and only 1.6 to 2.1 Å high which corresponds to 1 – 3 atomic layers. On the Ge wetting layer, the Mn induces increased roughening and some islands can be discerned. Annealing cycles revealed that the Mn islands are stable up to approximately 180°C and only undergo minor ripening processes. At higher annealing temperatures, above 350°C, the Mn

islands are no longer present on either the Ge QD hut facets or the Ge wetting layer. However, new large islands appear on the surface indicated the formation of secondary phases.

The third route investigated is the co-deposition of Mn and Ge during the normal heteroepitaxial growth of Ge QDs (see Chapter 6). The STM investigations consisted of observing the state of the growth at two different steps: (1) partial wetting layer growth (1.5 – 2 ML of $\text{Mn}_x\text{Ge}_{(1-x)}$ deposited) and (2) after a full QD growth consisting primarily of huts. Additional studies utilizing Scanning Auger Microscopy investigated the co-deposition of Ge and Mn and the distribution of Mn among secondary phases. Mn concentrations were varied and revealed that at Mn concentrations below 10% the formation of secondary phases can be suppressed. Even when secondary phases did form, the quality (shape and atomic structure) of the QDs is preserved and the wetting layer was not perturbed. The magnetic properties of most samples prepared had Curie Temperature (T_C) around 50 K; however, two samples displayed room temperature ferromagnetism. The first was a sample with 23% Mn content and showed secondary phases in the STM images. Mn_5Ge_3 and $\text{Mn}_{11}\text{Ge}_8$ are two ferromagnetic phases that could form under our growth conditions. In addition the formation of ternary MnSiGe phases is possible under our growth conditions and is considered as a possibility, the nature of their magnetism is not known. The second was a sample with 5% Mn content which did not display secondary phases in the STM images. The room temperature magnetic response of this sample was confirmed using both VSM and XMCD. XMCD gave use a clear picture that Mn was responsible for the magnetism in the sample.

1.3. Materials Background

1.3.1. The Si(100) Surface and (2x1) Reconstruction

The entirety of this research used Si(100) as a substrate for Mn-wire growth and Ge quantum dot growth. To understand the Si(100) surface, it is important to start with the bulk crystal structure. Si has the diamond cubic structure which is composed of an FCC lattice with a two atom basis at 000 and $\frac{1}{4}\frac{1}{4}\frac{1}{4}$. If the diamond cubic structure is truncated along the (100) plane, the ideal termination that is formed is what is called a 1x1 structure, by Wood's notation [19,20]. Wood's notation for two-dimensional surface superstructures relates the surface superstructure or reconstruction to the lattice of the bulk. The notation is given by $m \times n - R\phi^\circ$ where m and n represent the ratio of translation vectors between the superstructure and the bulk lattice in the equivalent two dimensional plane. $R\phi^\circ$ is used when the superstructure is rotated with to the bulk lattice. As is the case with the surfaces discussed in this dissertation, 0° rotation is assumed when no rotation is noted.

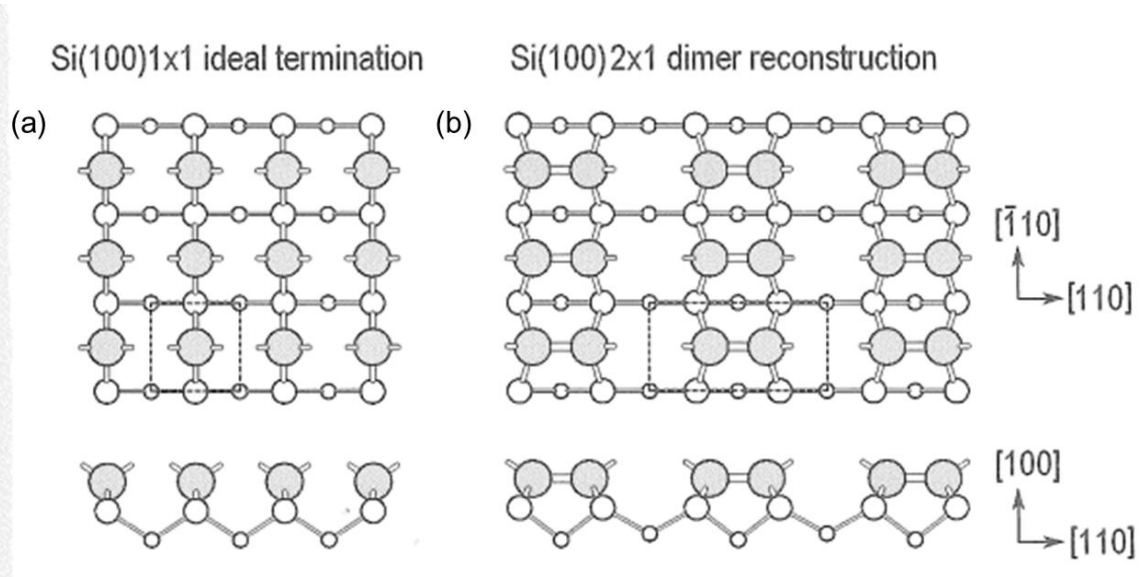


Figure 1.1. Schematic of (a) an ideal Si(100)1x1 surface and (b) a Si(100)2x1 surface. The topmost atoms are shaded grey and the unit mesh for each configuration is highlighted by the dotted line.

As mentioned previously, the truncated surface of Si(100) is 1x1; however, this termination results in two dangling bonds per atom and as a result is not the lowest energy state. Sample preparation of Si(100), as described in Section 2.4, gives the surface atoms enough mobility to rearrange into a configuration which satisfies one of the dangling bonds per atom. The surface atoms form into dimers and the dimers fall into rows running along the surface. This reconstructed surface is noted as Si(100)2x1 and a comparison between a Si(100)1x1 and Si(100)2x1 surface can be seen in Figure 1.1. The dimer structure involves not just the rearrangement of the immediate surface atoms, but to accommodate the structure atoms 5 layers below the surface also shift in position [21,22].

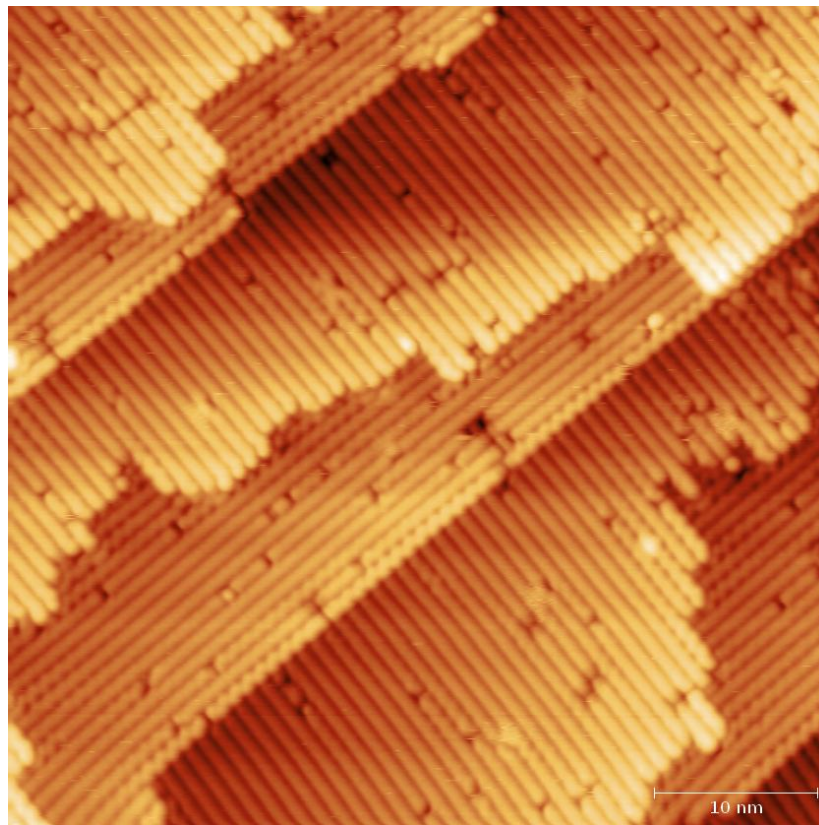


Figure 1.2. STM image of a thermally cleaned Si(100) displaying the 2x1 reconstruction, alternating directions of dimer rows, terraces and step edges. Image acquired with a sample bias of -1.5 V.

A representative STM image of a prepared Si(100)2x1 surface is shown in Figure 1.2. The surface consists of terraces of dimerized Si atoms and one atom high steps. One should note that the direction of the dimer rows rotates by 90° from terrace to terrace. This is simply due to the atomic structure of Si and the rotated arrangement of atoms from layer to layer within the diamond cubic structure. The STM images of the Si(100)2x1 surface was obtained at room temperature, which is also the case for most images included in this thesis unless otherwise specified. At this temperature the individual atoms of the dimers cannot be imaged because the dimers are constantly moving at room temperature. Within the dimer, one atom sits 18° higher than the other atom and at temperatures above 200 K the atoms constantly alternate between these two separate states where another atom sits higher than the other. The characterization and understanding of the Si(100)2x1 surface is important for this work since it serves as the substrate where Ge QDs are grown in Chapter 5 and Chapter 6 or as a structure where the direct interaction of Si and Mn is the focus in Chapter 3 and Chapter 4.

1.3.2. Formation of Wire Structures on Si(100)2x1

The dimer row structure of the Si(100)2x1 surface has lent itself to the formation of structures with a large aspect ratio, wires, and other one dimensional like structures. Some of the structures in this section and in this thesis are referred to as wires; however, these structures do not necessarily behave as wires where the electronic structure is delocalized along the length of the wire. There have been many wire structures that have been synthesized on Si surfaces [2323–37] and other surfaces [38–41]. Often as is the case with rare-earth elements, silicide wires form as a result of anisotropic lattice mismatch between the rare-earth silicide and Si(100). The wires minimize one direction with high lattice mismatch or high strain and elongate along the direction with the lower lattice mismatch or low strain. The wires typically will grow in the [110] direction

and are a 3-10 nm wide and can be up to several hundred nanometers long [28,29,42,43]. In contrast, Bi nanolines form on the Si(100)2x1 surface as a result of local strain relief running perpendicular to the Si dimers. The nanolines are unique since they can be on the order of 300 nm long, 1 nm wide, and possess no kinks or defects along the length of the nanoline [24,36]. Due to this defect free structure, the Bi lines stabilize a different substructure of the Si surface and relieve stress from the Si(100)2x1 reconstructed surface. Many of the wires mentioned above are silicides and were formed by reactive epitaxy, as opposed to the room temperature depositions performed in this research.

1.3.3. Heteroepitaxy and the Formation of Ge Quantum Dots

In this thesis work, Ge QDs were grown on a Si(100) substrate. Ge QDs are grown by heteroepitaxy on a Si(100) substrate. In general, epitaxial growth requires a crystalline substrate and the growing layers must have some degree of registry with the substrate. The growth of a film consisting of the same element as the substrate is homoepitaxy whereas a different element is heteroepitaxy. In addition, there are three different growth modes of a thin film as shown in Figure 1.3. Frank van der Merwe growth consists of layer-by-layer growth. The adsorbed atoms of the growing film more strongly bond to the substrate than to each other. This drives the growth to layer-by-layer growth since the first monolayer will typically be complete before the second layer starts to grow. Due to the highly preferred bonding between the deposited material and the substrate, the second, third, fourth, etc. layers will have weaker bonds.

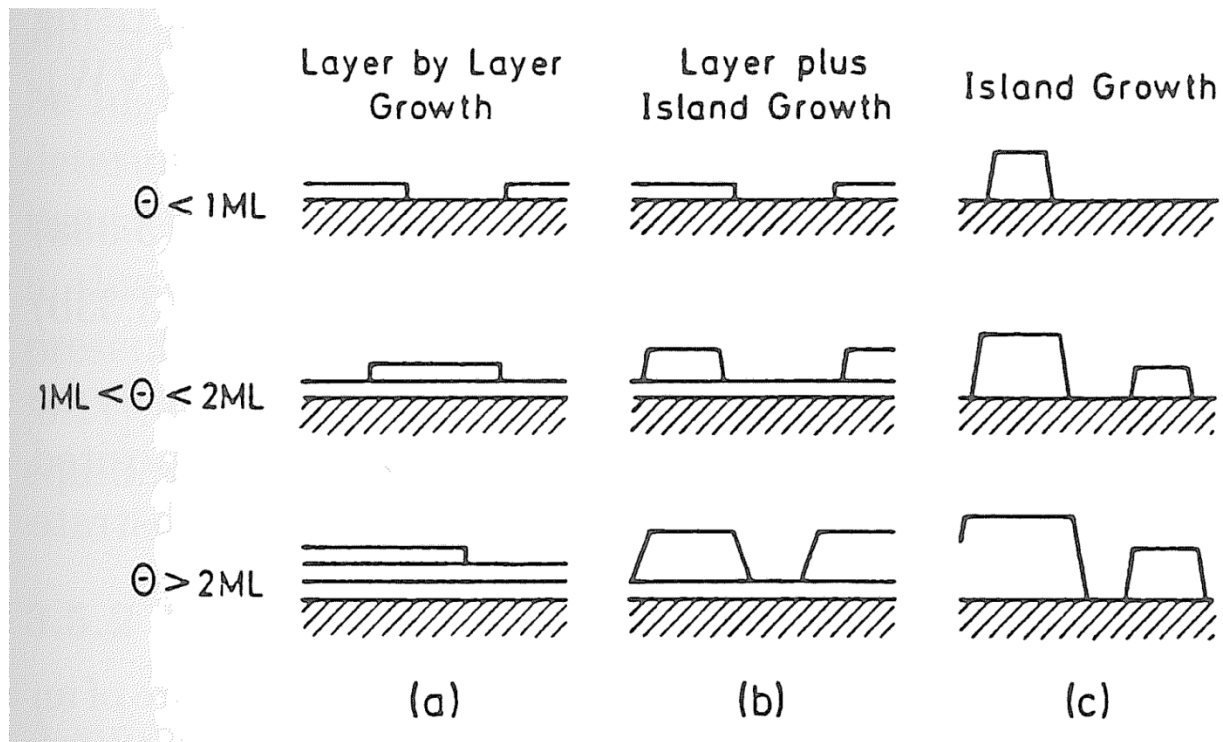


Figure 1.3. Schematic representing three growth modes of a film as a function of coverage (θ). (a) Layer-by-layer growth or Frank-van der Merve. (b) Layer-plus island growth or Stranski-Krastanov. (c) Island growth or Volmer-Weber). [44]

At the other extreme where the incoming adatoms of the growth layer bind more strongly to one another than the substrate is Volmer-Weber growth. Due to the strong self-interaction, this growth mode is characterized by three-dimensional islands and is comparable to a non-wetting type of growth. The third growth mode is Stranski-Krastanov (SK) and is the growth mode that forms Ge QDs. SK growth is the intermediate growth mode between Frank van der Merwe and Volmer-Weber growth. Typically a discrete number of layers will grow layer-by-layer; however, continued growth layer-by-layer becomes unfavorable and further growth switches to Volmer-Weber. The three-dimensional islands that form are the Ge QDs. SK growth requires heteroepitaxy and involves the buildup of stress within the film, which grows layer-by-layer. In the case of Ge on Si(100), the lattice mismatch between the two crystal structures is 4.01%. After three monolayers of Ge are deposited, Ge QDs start to nucleate. At the base of the Ge QDs, the

Ge lattice parameter is close to that of Si and with each subsequent layer the Ge lattice in the QD relaxes to near the unstrained Ge lattice parameter at the apex.

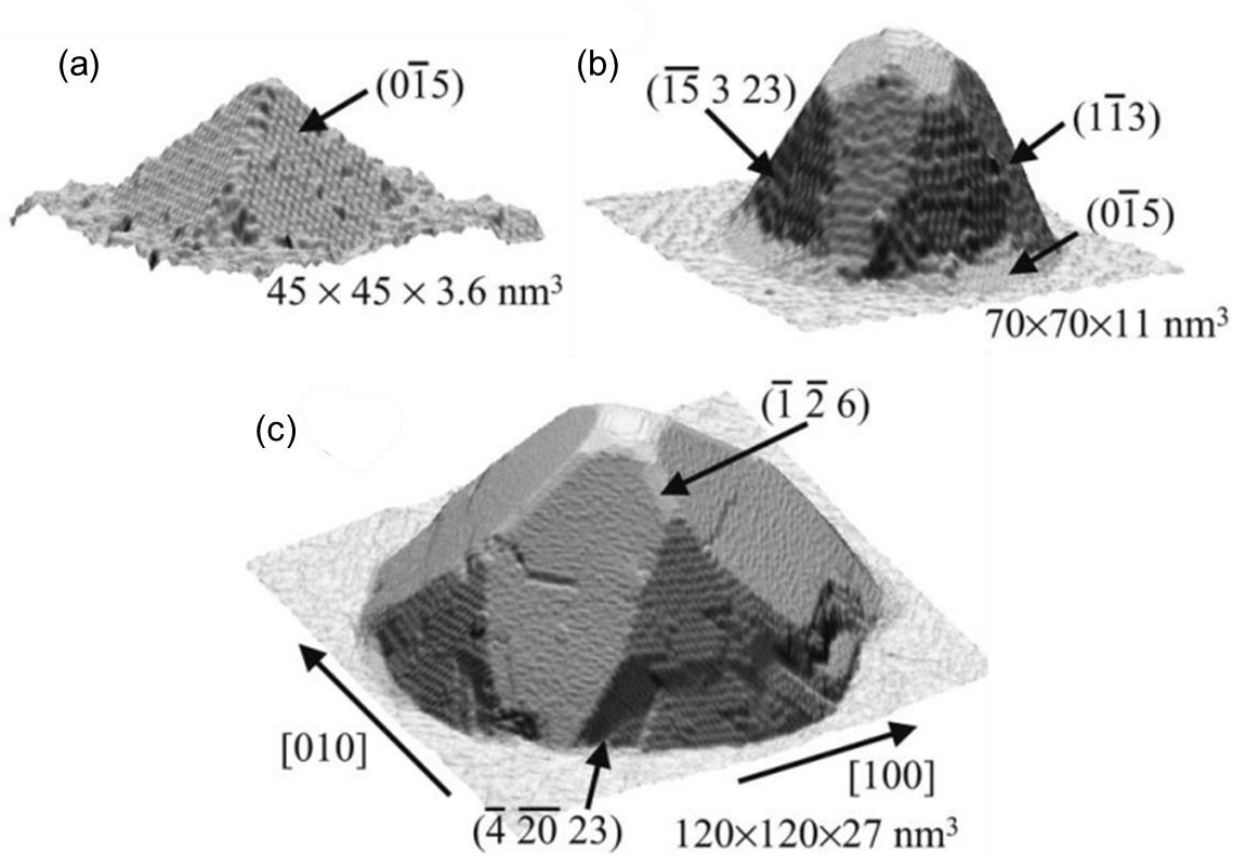


Figure 1.4. STM images of a Ge QD (a) pyramid, (b) dome, and (c) superdome. Note the exaggerated z-scale. [45]

There are three different types of quantum dots that can form during Ge heteroepitaxy on Si(100). The first type of quantum dots are pyramids, otherwise known as huts, which can possess square bases or rectangular, elongated bases. Huts are ideally 11.3° above the surface plane and consist entirely of Ge{105} facets. With increasing deposition of Ge, huts will undergo ripening processes but will eventually transform into a second structure called a dome. Domes are characterized by (113) and (102) facets and a larger angle off the surface plane, 25.2° to 26.6° . Domes and huts are both defect free structures. Huts can range in sizes along the base

from 15 to 50 nm and only a few nanometers high. Domes are larger than huts, ranging from 40 to 100 nm across the base and tens of nanometers tall [46]. The third type of quantum dot does contain dislocation and are larger again than domes, called superdomes. Dislocations form in superdomes to further decrease the strain energy within the volume of the quantum dot.

1.3.4. Dilute Magnetic Semiconductors

Dilute magnetic semiconductors (DMS) are materials where a magnetic ion is incorporated into a semiconductor matrix and as a result the material behaves like a ferromagnetic material. However, where traditional ferromagnetic materials exist due to spin alignment from spin-orbit coupling and small distance interactions, the doping levels of DMS materials cannot achieve ferromagnetism via direct exchange coupling from magnetic ion to magnetic ion. The dilute nature of the magnetic ions requires an intermediary to transfer the alignment of spin and produce long-range magnetic order. DMS materials achieve this long range order via holes. The hole-mediated ferromagnetism of DMS materials makes them particularly attractive for spintronics applications. The presence of long range order can be tuned with the injection or removal of holes via the use of a gate voltage. In other words, a DMS material can be gated and an external electric field can control the ferromagnetism of the material.

There has been much research with several magnetic ions, Mn, Cr, Fe, Ni, and Co, with semiconductors ranging from the group IV elemental semiconductors to compound semiconductors as well. The development of (In, Mn)As gave researchers DMS materials with high Curie temperatures and has spawned many papers and many focusing on Mn as the magnetic dopant [47–49]. Munekata and coauthors were among the first to start incorporating higher concentrations of Mn, beyond normal dopant levels, and exploring the effect of growth temperature on the magnetic properties of films [47]. The low growth temperature, ~200°C,

enabled the researchers to grow metastable structures and incorporate up to 18% Mn into the structure. Researchers have achieved Curie temperatures for (Ga,Mn)As up to 160K [5,9,50,51] and ranging from 290 K to 340K for (In,Mn)As quantum dots [52,53]. The (In,Mn)As QDs grown by researchers provide an interesting case study to compare the Curie temperature of thin films and QDs. As mentioned previously the Curie temperature can be enhanced by carrier confinement in quantum dots [15]. However, researchers have been able to incorporate more Mn into (In,Mn)As QDs as opposed to thin films and this alone could explain the enhancement in Curie temperature [52].

For DMS materials, research in III-V compound semiconductors is arguably more mature than research in group IV DMS materials. For applications of spintronics where compatibility with current Si-based technology is desired, Si and Ge based DMS materials are highly desirable. More than a decade ago, Mn doped Ge structures have been predicted and studied to have field controllable ferromagnetism [54–57]. In the preparation of Ge:Mn films and nanostructures, researchers have to work to suppress the formation of secondary phases, specifically Mn_5Ge_3 and $\text{Mn}_{11}\text{Ge}_8$. Both of these secondary phases are traditional ferromagnets with Curie temperatures ranging from 285 K to 298 K [58]. A range of different preparation methods have been used to create Mn-doped Ge nanostructures and films, and with varying success the Curie temperatures have varied widely from 25 K to above 400 K [56,57,59–71]. Crystalline thin films of Ge:Mn have varied in Curie temperature from 25 K to 235 K in addition to one study with a Curie temperature at 285 K but was later shown to show signatures of Mn_5Ge_3 precipitates within the film [56,57,61–63]. More unique structures have also been studied, such as Mn:Ge nanocolumns with Curie temperatures ranging from 120 K to above 400 K. These films contain areas of Mn enriched columns which segregate during the growth of the films at growth temperatures

typically less than 150°C [63–68]. Amorphous Mn:Ge films have also been studied and researchers have prepared the amorphous films from ion implantation or co-deposition at low growth temperatures. Curie temperatures again vary from 100 K to above 300 K [69–71]. There is a wealth of literature on Ge:Mn films and nanostructures, but a clear consensus on how to form consistently high Curie temperatures while suppressing secondary phases has not been formed.

Aside from Ge:Mn thin films, other investigators have also pursued doping Ge QDs with Mn. Specifically the research group of K. Wang at UCLA have grown Mn (and also Fe) doped Ge QDs [59,60,72]. The authors grew Ge:Mn QDs at a concentration of 5% Mn and produced films with a Curie temperature above 400 K. Transmission electron microscopy and electron loss spectroscopy showed regions of Mn segregation below the QDs and into the substrate. The source of segregation in this case is not well understood and many questions remain on the growth process when a significant concentration of Mn is introduced into the system. Interestingly the authors also were able to cap and gate the structures and control the magnitude of the saturation magnetization with the application of an electric field.

This previous work illustrates the variety of Ge:Mn structures that researchers have pursued but a strong case for a consistent structures with a high Curie temperature is still a work in progress. Notably the effect of Mn on the growth of different structures and how Mn segregates in the Ge system is one point this thesis sets out to further study and discussion.

Chapter 2. Experimental Techniques

2.1. Scanning Tunneling Microscopy

The invention of the STM by Binnig and Rohrer in 1981 [73,74] has brought with it a wealth of data and understanding of surfaces, their structure and reactions taking place on the surface, not to mention a Nobel Prize for its inventors in 1986. The STM allows researchers to resolve the atomic structure of surfaces in real space, observe the atomic-level effects of adsorbates, manipulate atoms [75–77] and even trigger chemical reactions [78–80]. The first real-space STM images were of the Si(111)7x7 reconstructed surface [81]. This reconstructed surface has a large unit cell and previous low-energy electron diffraction experiments and modeling were unable to describe the details of the structure. In addition, the invention of the STM aided researchers to identify an accurate model of the Si(100)2x1 reconstruction, previous models failed to describe in particular the presence of buckled dimers which oscillated at room temperature.

STM operates on the principle of quantum tunneling. If two metals are separated by a thin insulated barrier, whether it be vacuum or an insulating material, there exists a potential barrier, U , between the two metals. In classical mechanics, an electron of energy E can only overcome the potential barrier if the energy of the electron exceeds the potential barrier. However, in quantum mechanics there is a finite probability that an electron with an energy less than the potential barrier can have a position within the barrier. The wave function describing the electron in the potential barrier has the form shown in Equation 2.1. The exponential decay of the function shows that the electron will always have a non-zero probability of penetrating the potential barrier. In order to exploit the tunneling and obtain an appreciable tunneling current, the width of the insulating barrier should be sufficiently small [82]. The configuration of a tunneling junction is illustrated in

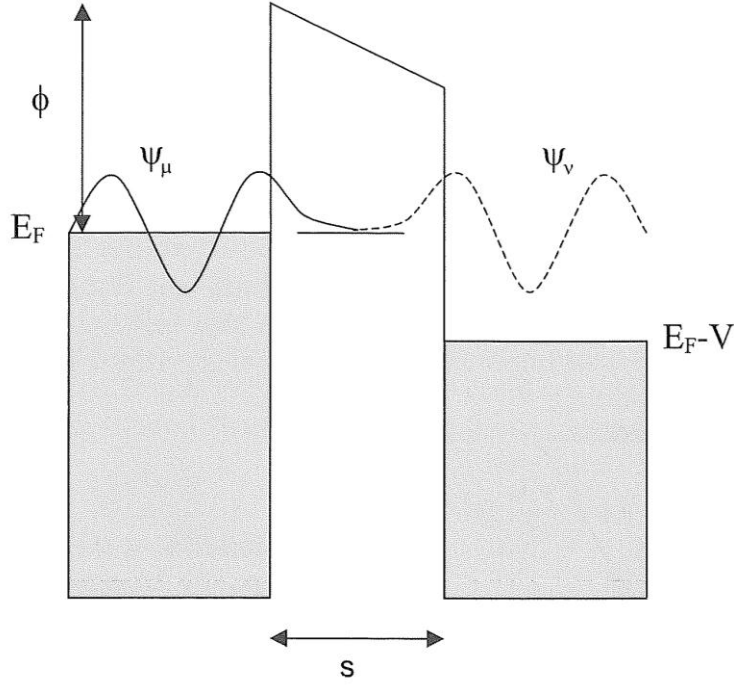


Figure 2.1. Diagram of a one-dimensional tunneling junction. The wave functions of the tip and sample overlap when separated by a distance, s . With the application of a sample bias, V , electrons are able to tunnel into the empty states of the sample. The potential barrier is in most cases representable by the work function, ϕ . [83]

In STM, the vacuum gap between the sample and tip is treated as a potential barrier, U , that the electron must overcome for tunneling to occur. The wave function, ψ , of the electron penetrating the barrier is described by:

$$\psi(z) = \psi(0) \exp \left[-\frac{\sqrt{2m(U - E)}z}{\hbar} \right] \quad 2.1$$

where E is the energy of the electron, m the mass, z is the distance between the tip and sample, and \hbar is Planck's constant divided by 2π [83]. The tunneling current, I_t , can be found by considering the density of states of the sample at the Fermi energy $N(E_F)$:

$$I_t \propto VN(E_F) \exp \left[-2 \frac{\sqrt{2m(U - E)}z}{\hbar} \right] \propto VN(E_F) \exp[-1.025\sqrt{U}z] \quad 2.2$$

The potential barrier of the vacuum gap is given by U in eV and the distance between the tip and sample, z , in units of angstroms [83]. Equation 2.2 originally was developed and applied to the

ideal case of one-dimensional tunneling. It was shown by Tersoff and Hamann that Equation 2.2 can be applied in the three-dimensional case when the wave function of tip is assumed to be an s-wave or spherical in shape [84,85]. The Tersoff-Hamann model has become the standard approximation for STM. However, the Tersoff-Hamann model is a first approximation of STM and does not fully explain images produced from all surfaces. Equation 2.2 indicates the direct dependency of the tunneling current to change with the applied bias voltage, V , and $N(E_F)$, also the exponential dependency of the tunneling current on z . It is important to make this connection when performing scanning tunneling microscopy, or any microscopy, to make a connection between what the contrast in the images you get actually represent on the sample. Here the importance of the bias voltage and the density of states becomes apparent and must always be considered when interpreting images and serve as a reminder that STM images are not always a topographic representation of the surface. A classic example illustrating the bias dependence of the images that can be obtained with STM is the GaAs(110) surface, as seen in .

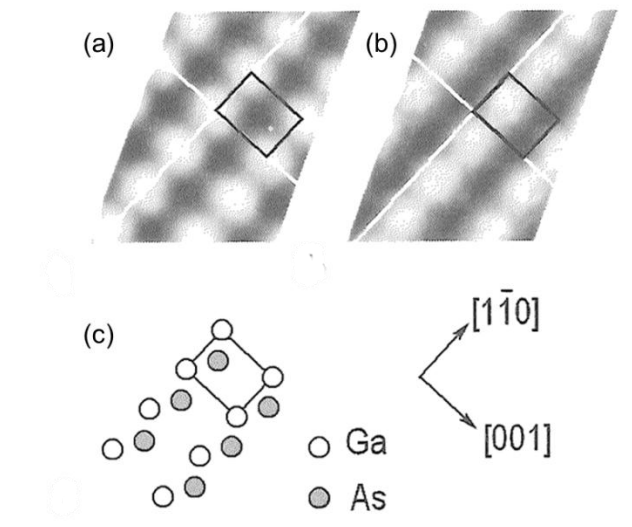


Figure 2.2. STM images of the GaAs(110) surface acquired at samples biases of (a) +1.9 V (empty states) and (b) - 1.9 V (filled states). (c) The top view model of the GaAs(110) surface atoms. In the empty state image the contrast comes from the Ga atoms and in the filled state image the As atoms are the source of the contrast. [19,86]

When an ideally atomically sharp tip/probe is brought within a fraction of a nanometer to a sample surface and a bias voltage is applied between the two, electrons will tunnel across the vacuum gap to the sample or tip depending on the polarity of the bias. The current generated is fed into a feedback loop that controls the distance between the sample and the tip when operated in constant current mode while scanning across the surface. The current measured by the instrument changes roughly by an order of magnitude when the distance between the tip and samples changes by one angstrom. As a tip is scanned over the surface, different features, whether topographic or electronic, can cause the current to change and the system will react by changing the distance to keep the current constant. In order to scan over the surface and make fine (fractions of a nanometer) adjustments, the tip is placed on a piezoelectric scanner which has a sensitivity of 10 V/nm along all axes. A schematic showing the main components of the STM is shown in Figure 2.3.

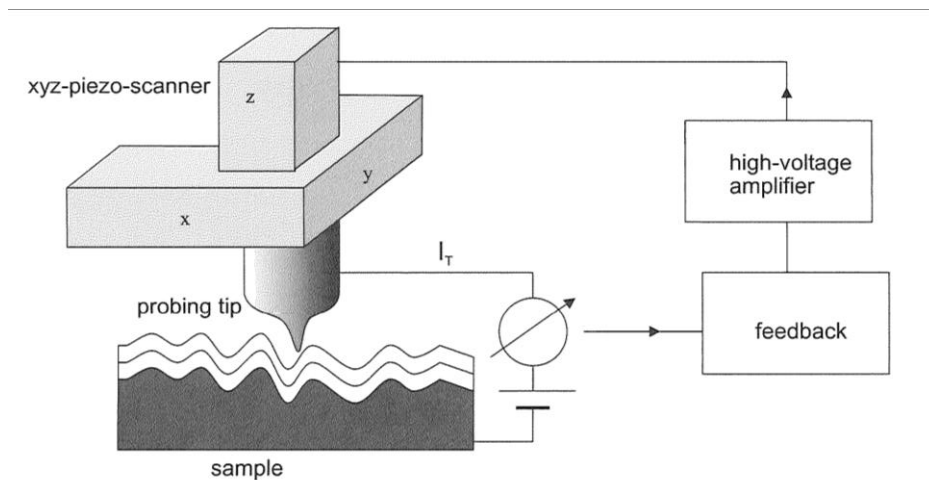


Figure 2.3. Diagram of a scanning tunneling microscope. X-Y piezoelectric scanners move the tip laterally across the surface during imaging. In constant current mode, the Z piezoelectric adjusts the height of the tip from the sample based on the change in current via the feedback loop [83].

Obtaining atomically resolved images with a slow scanning instrument such as the STM can be difficult due to vibrations, among other technical challenges. The first level of vibration isolation are four soft springs that the entire STM stage, including sample and scanner, are

suspended from and the next is the Eddy current damping. On the perimeter of the STM stage, copper fins are mounted and a series of permanent magnets are mounted in a ring with a magnet lying between a pair of copper fins. In addition, the entire STM UHV chamber is mounted to a table that sits on three passive air legs, which assist in damping building vibrations through the floor.

2.2. Scanning Tunneling Spectroscopy

While STM is used to generate an image from a fixed imaging bias, STM instruments are also capable of performing Scanning Tunneling Spectroscopy (STS). Tunneling spectroscopy can be defined as the study of the bias dependence of the tunneling current. Different modes of tunneling spectroscopy are identified within this broad definition. Acquiring STM images at several imaging biases can reveal spectroscopic information, but the convolution of topographic and electronic information can complicate the analysis. Conductivity maps can be obtained by varying the distance between the tip and sample while modulating the bias voltage. In addition, the tip can be held at a constant separation and I-V curves can be acquired at single points or on a predefined grid. In the case of point spectroscopy, the feedback loop described in the previous section is turned off and an I-V curve is obtained at a constant height at a selected point. The I-V curves can then be calculated as $(dI/dV)/(I/V)$ curves which correspond to the local density of states of the sample [19]. It is also common practice in the literature to plot dI/dV in some cases to determine the band gap of the material. When performing tunneling spectroscopy, depending on the bias voltage, the empty or filled states are probed. An ideal metal tip can be assumed to provide an abundance of states to tunnel in and out of. As a result, the local density of states of the sample is probed.

Another type of spectroscopy consists of normal constant current imaging at several different bias voltages, particularly at opposite polarity. Voltage dependent STM imaging has advantages to be able to see the geometric relationship of structures and their electronic states across different bias voltages. However, this method is limited for the same reason since the geometric, topographic contribution to the STM image is always present as the tip-sample distance is adjusted by the feedback loop and does not necessarily represent the true local density of states. If the waveforms of the sample and tip do not overlap because of geometric reasons, even if states are available to tunneling in or out of, there is no tunneling between those particular features. For this reason, voltage dependent STM images can be difficult to interpret due to the ever presence of the topographic component [87].

There are some drawbacks to the interpretation of STS data which prevents direct comparison of the fine structure of the local density of states with calculated density of states or band diagrams. Typically, simulated local density of states will assume that the influence of the tip on the measured density of states is nonexistent; the tip is assumed to have a free electron gas like an ideal metal. More refined calculations require exactly measuring the density of states of the tip which can often be non-ideal and change during the course of a measurement [19]. In the research presented here, voltage dependent STM image type spectroscopy and point spectroscopy are used to further the understanding of the nanostructures formed during experiments.

2.3. Ultra-High Vacuum Chamber

All sample preparation and most sample characterization took place in Ultra-High Vacuum (UHV) chambers. The majority of the experiments were completed in a combination analysis and preparation chamber at UVA, a commercial system from Omicron Nanotechnology GmbH.

The experiments in the Omicron commercial system with a base pressure in the range 6.0×10^{-11} to 1.5×10^{-10} mbar. The system consists of two chambers, one containing the Scanning Tunneling Microscope (STM) itself and the other with a 4-axis sample manipulator and resistive heater and deposition sources. The UHV conditions are maintained by a series of pumps: a Pfeiffer TMU 071 P turbomolecular pump backed by an Edwards RV3 two stage rotatory vane pump with fast acting inlet valve to prevent back streaming of pump oil. The turbomolecular pump and rotary vane pump are used primarily to get the chamber down to UHV conditions during system bakeouts and to pump down a small loadlock used to transfer in samples and STM probes into the chamber. When the microscope is in operation a combination of a Varian StarCell VacIon 150 Plus ion pump and a three filament Ti sublimation pump are used to maintain UHV conditions in the main chamber. Images of the STM chamber depicting the above components are shown in Figure 2.4.

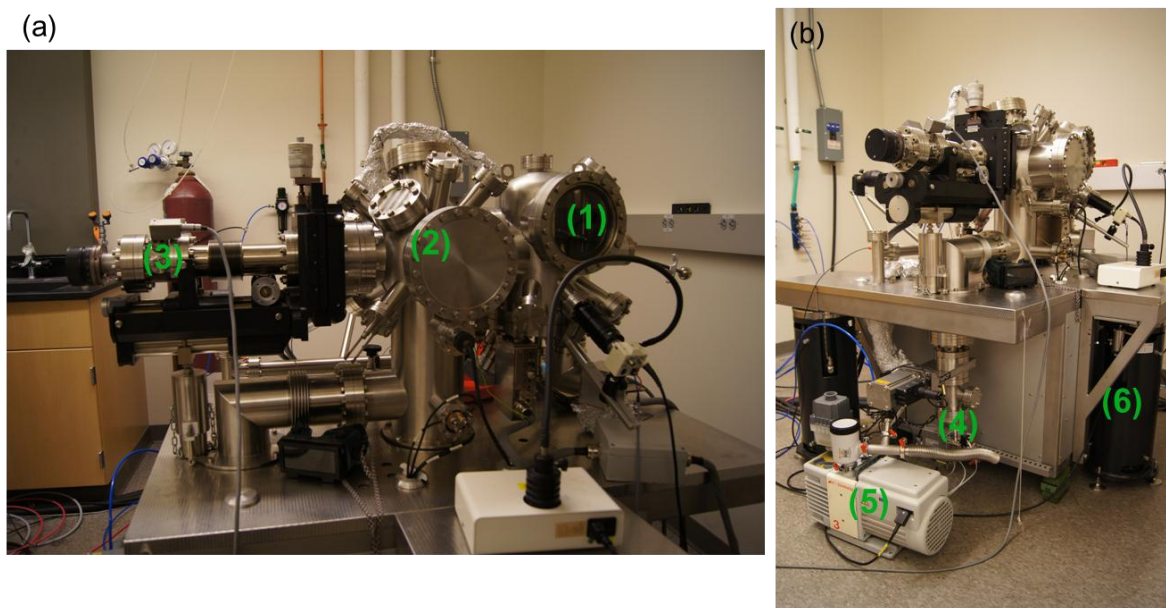


Figure 2.4. Images of our Omicron UHV chamber. Shown in the images are the following components: (1) the bell jar which houses the STM, (2) a spherical chamber with the deposition sources attached, (3) 4-axis manipulator which extends into the spherical chamber, (4) turbomolecular pump, (5) rotary vane backing pump, and (6) the passive air legs for vibration dampening. The ion pump, not pictured, is located within the table.

2.4. Si(100) Sample Preparation

There are several methods available to the experimenter to clean and prepare a Si(100) surface in order to achieve the (2x1) reconstruction, see Section 1.3.1. Much of this depends on the size of the sample. Larger samples typically undergo a chemical clean prior to transferring into vacuum. The typical procedure is to remove any hydrocarbons on the surface, strip the native oxide and replace it with a non-stoichiometric oxide that can be readily desorbed at elevated temperatures in vacuum. Once the oxide is desorbed at approximately 800°C a buffer layer of Si is deposited at 600-700°C to achieve the cleanest surface possible.

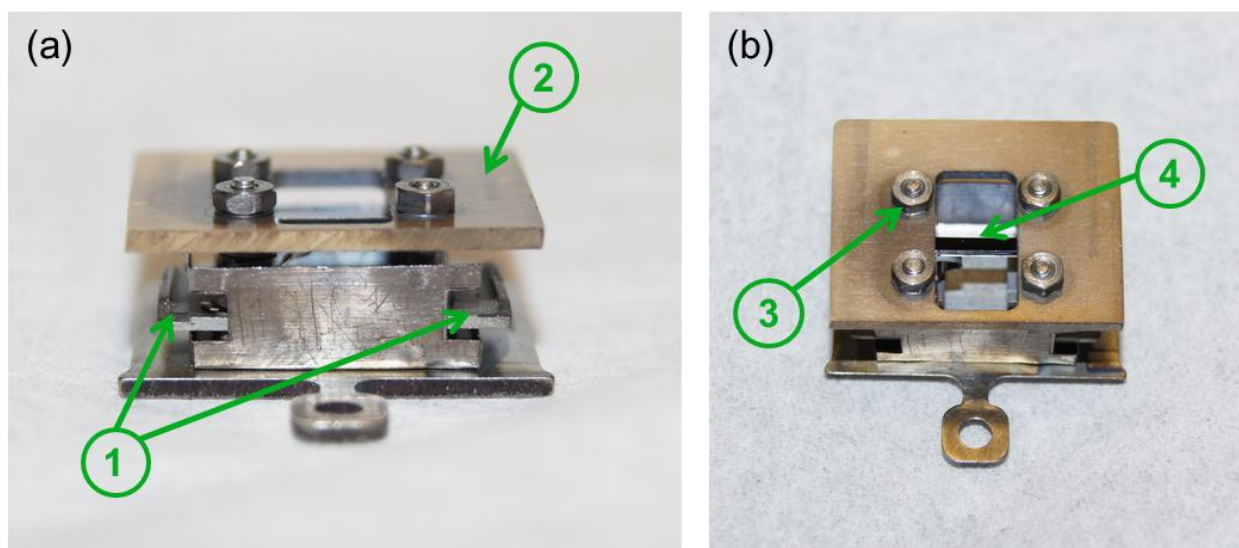


Figure 2.5. Images of the direct current sample holder. The sample holder is shown fully assembled. (1) The contact bars used to make electrical contact to the Si sample within the chamber. (2) The ceramic top plate which helps to hold the sample in place with (3) four molybdenum studs and nuts to clamp (4) the sample.

Smaller samples, which is what this research utilized, can be cleaned chemically as well as described above but can also be cleaned simply with higher annealing conditions. Our method for thermal cleaning of Si is based on procedures outlined in the literature [88,89]. Our samples, 10 mm x 1 mm x 0.5 mm, are mounted on a sample holder designed by Omicron Nanotechnology GmbH that allows for a current to be passed directly through the sample, i.e. direct current heating. The sample holder is pictured in . This setup allows us to heat quickly the

Si sample to temperatures approaching the melting temperature of Si. In addition, samples must be doped to have a resistance low enough in order to drive a sufficient current through the sample. Our samples were boron doped (p-type) within the range $1.2 \times 10^{17} - 1.5 \times 10^{17}$ dopants/cm³ which resulted in a resistance range of 0.065 – 0.074 $\Omega \cdot \text{cm}$.

After transferring the sample through the loadlock into the main chamber, the sample is outgassed overnight at approximately 550°C until the pressure in the main chamber returns to a value close to the original base pressure prior to transfer. Following the overnight anneal, the sample flashed at increasing higher temperatures for short bursts lasting about 3 seconds or briefer while maintaining a pressure ideally better than 1.0×10^{-9} mbar. In detail, the heating protocol is done in current limited mode from 0.5 A to 3.5 A in 0.5 A increments. At each increment, the sample is flashed for 3 seconds or less until the pressure is controllable and does not increase as quickly. Continuing the heating beyond 3.5 A is done in 0.1 A increments since the oxide is removed, around 900°C. The maximum current needed ranges typically from 4.2 A to 4.5 A; the sample essentially needs to be heated up to a temperature high enough obtain sufficient surface atom mobility without causing any melting. Through a viewport on the chamber, the brightly the sample glows during the flashing can be checked. At the final flashing condition, the sample should appear to have a bright nearly white-yellow glow. The final temperature is around 1250°C, and surface Si atoms sublime which aides in achieving a clean surface by simply removing the initial bad surface. At the final flashing condition, the sample is flashed 20 to 30 times. The above procedure is used throughout this research and repeatedly produces surfaces of high quality with point defect concentrations less than 5% by areal coverage.

2.5. Deposition Sources

Two main types of physical vapor deposition sources were used during this research, an effusion cell for Ge evaporation and electron beam (e-beam) evaporator for Mn. The end result of each evaporator is the same, the source material is heated to a point where the vapor pressure of source material exceeds the background pressure of the UHV chamber. Veeco makes the effusion cell evaporator and has a 4 cc crucible made of alumina. The crucible is surrounded in a serpentine fashion by a filament that allows for controllable and consistent heating along the majority of the volume of the crucible and thus the source material. The effusion cell requires careful and slow heating operation (10 – 20°C/min) due to the thermal load and possibility of cracking the alumina crucible. Extra care has to be taken if the material to be evaporated undergoes any phase changes during the heating/cooling operation.

The e-beam evaporators used in our case are small-scale evaporators. Three different e-beam evaporators were used during the course of this research, but the principle of operation are the same for all three. E-beam evaporators heat a conductive crucible (or source material rod) by electron bombardment of thermionic electrons extracted from a hot tungsten filament with a large positive bias voltage applied to the crucible or rod. E-beam evaporators require a water cooling shroud with the filament and crucible or rod located within the shroud. E-beam evaporators offer advantages of being able to evaporate refractory materials such as tungsten and once a material is sufficiently outgassed the material can be heated quickly. The three different e-beam evaporators used were one homebuilt source courtesy of Catherine Dukes, Ph.D., one single pocket evaporator from Mantis Deposition LTD (model: M-EV) and a four pocket evaporator also from Mantis Deposition LTD (model: QUAD-EV-C).

2.6. Synchrotrons and X-ray/Ultraviolet Photoemission Spectroscopy

To explore the bonding between Mn and Si(100), Ultraviolet Photoemission Spectroscopy (UPS) experiments were performed at the National Synchrotron Light Source (NSLS) at Brookhaven National Laboratory (BNL). Synchrotron radiation is attractive for the intensity of light and the tuneability of the photon energy at small increments. The latter in photoemission spectroscopy experiments is often more important, and this does not hold true for x-ray diffraction and other techniques performed at synchrotron light sources.

Synchrotron radiation occurs simply due to the conservation of momentum. When energetic charged particles are redirected, typically with magnetic fields, the change in the tangential component of the velocity vector is compensated with the emission of radiation via the conservation of momentum. Synchrotron light sources take advantage of the radiation to perform different spectroscopies and diffraction experiments. Synchrotron storage rings are designed to give users high intensity radiation for extended periods of time. Electrons are injected into the UHV storage ring at energies of a few GeV and the electron bundles are gathered and deflected around the ring using magnetic fields. Tangentially from the ring, are a series of UHV tube chambers called beamlines where the radiation is focused, passed through slits for filtering, and monochromators before reaching an analysis chamber containing the sample and detection equipment.

X-ray photoemission and ultraviolet photoemission spectroscopy are both based on the photoelectric effect. As a simplified three step process, incoming x-ray or UV photons excite electrons from occupied to unoccupied states, the excited electron proceeds to the surface, and finally the electron is emitted into the vacuum with a characteristic energy. The emitted electrons are analyzed for their kinetic energy by a hemispherical or cylindrical analyzer. As described in

Equation 2.3, the kinetic energy of the emitted electron is dependent on the energy of the incoming X-ray or UV photons less the binding energy and the work function. The peaks of electrons detected around kinetic energies corresponding to Equation 2.3.

$$E_{kin} = \hbar\omega - E_b - \phi \quad 2.3$$

For the purposes of this research, as mentioned above, we used UPS to study samples. The samples investigated consisted of room temperature deposited overlayers of Mn on Si(100)-2x1 and a-Si. UPS was chosen for the energy range covered, 160 eV – 40 eV, and the requirements of our experiment. Using UPS we probed the Si 2p core levels, the Mn 3p level, and the valence band.

2.7. X-ray Absorption Spectroscopy and X-ray Magnetic Circular Dichroism

In X-ray Absorption Spectroscopy (XAS) the change in the absorption coefficient is observed as a function of photon energy. If the photon energy corresponds to an absorption edge the absorption coefficient increases significantly. XAS differs from XPS since instead of probing the band dispersion of materials XAS explores the integral unoccupied density of states as a function of energy. During the X-ray absorption process, for example, an incoming electron interacts and excites an electron in a p-orbital and that electron is excited into an unoccupied d-orbital. The energy required for this transition is characteristic of the material studied. In addition, because of this transition, XAS becomes particularly attractive to probe the magnetic properties of materials. Those materials which are magnetic and have a non-zero net magnetization will display the band splitting in the d-orbitals. Effectively the magnetism of the material generates a preference of a certain electron spin depending on the direction of magnetization. When taking the XAS spectra with polarized light there will be a slightly higher absorption of x-rays when the polarization of the light aligns with the magnetization of the sample. The results from XMCD can be compared

to the results from the more traditional magnetometry techniques such as vibrating sample magnetometry and super quantum interference device (SQUID) magnetometry.

In x-ray magnetic circular dichroism (XMCD), dichroism refers to the difference in absorption of polarized light. When light is absorbed by a material with an energy that satisfies the difference between two electron states, the quantum selection rules (referring to the quantum numbers n , m , l and s) must be satisfied during the transition. One such selection rule that is exploited for XMCD is the conservation of angular momentum and the magnetic quantum number, ΔJ and Δm , respectively. When a d-orbital type magnetic material is under a magnetic field, the degeneracy of the electron states is broken and preferential absorption of light can occur. To observe this effect, circularly polarized light is used and when the light polarization is parallel to the direction of magnetization, absorption is enhanced and slightly depressed with antiparallel alignment. Figure 2.6 illustrates this effect of preferential absorption with circularly polarized light.

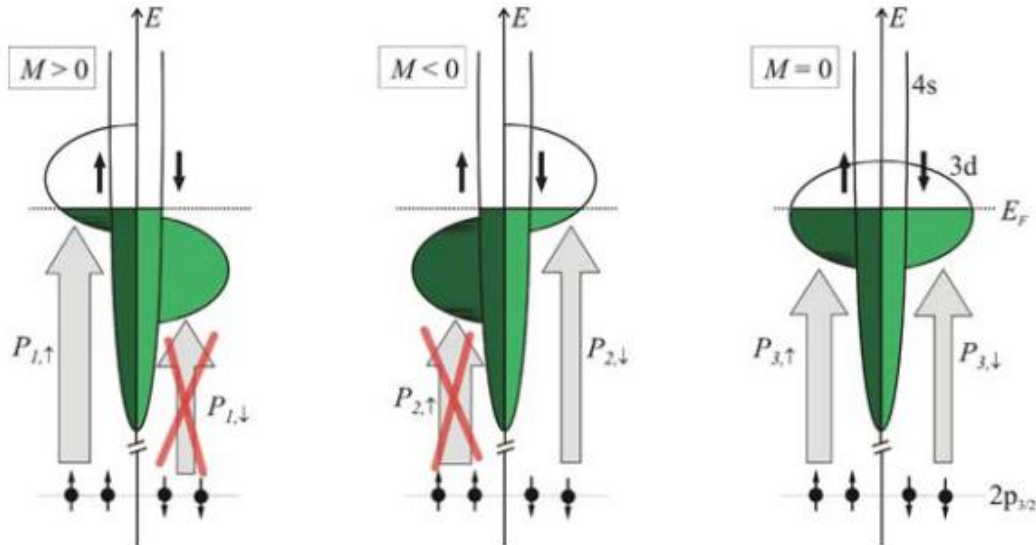


Figure 2.6. Schematic depicting the electronic transitions from a $2p_{3/2}$ level of a 3d ferromagnetic material for two opposing magnetization directions and for zero magnetization. [90]

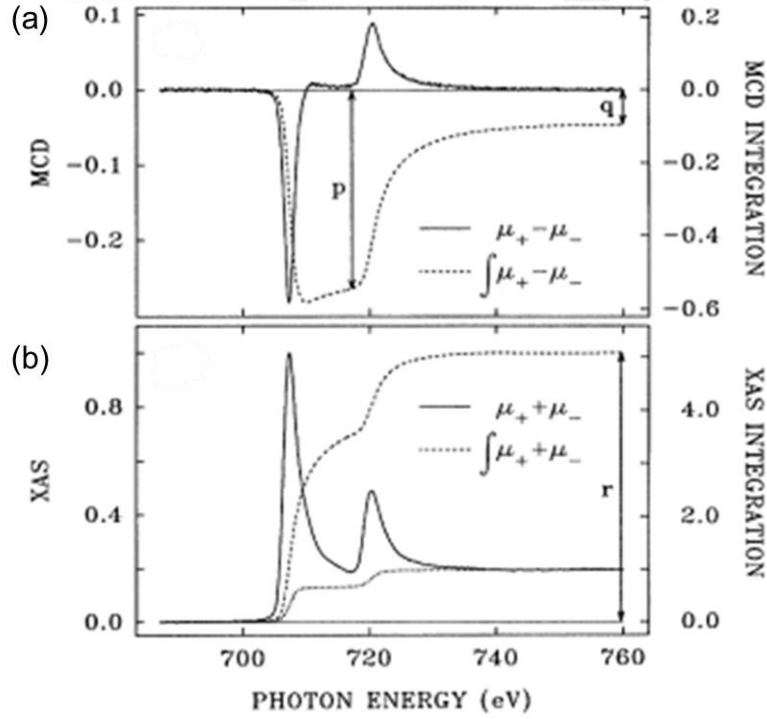


Figure 2.7. $L_{3,2}$ -edge XAS and XMCD spectra of iron: (a) XMCD spectra, solid line, of iron along with the integrated data, dotted line. The points where p and q are found is illustrated. (b) XAS spectra, solid line, of iron and the integrated data, dotted line, with r illustrated. [91]

XMCD reveals not only the elemental and orbital specific magnetization of a material, but can also separate the magnetization of a material into the orbital and spin components, m_{orb} and m_{spin} , respectively. Yonamoto *et. al.* and Goering initially proposed using the integrals of XAS and XMCD spectra to extract μ_{orb} and μ_{spin} using sum rule equations [92,93]. The sum rules were further developed by Chen *et. al.* and confirmed by experiment [91]. It is Chen's sum rules for 3d materials that are used in this research as seen here:

$$m_{orb} = -\frac{4q(10 - n_{3d})}{r} \quad 2.4$$

$$m_{spin} = -\frac{(6p - 4q)(10 - n_{3d})}{r} \quad 2.5$$

The values for p , q , and r are calculated from the integrals of the XAS and XMCD spectra as illustrated in Figure 2.7. The value of p is found at the left edge of the L_2 peak of the integral of

the XMCD spectra. The value of q is the total integral of the XMCD spectra of the $L_{3,2}$ peaks. The value of r is found from the total integral of the x-ray absorption spectra. The number of donor holes of the 3d metal is given by n_{3d} , and for Mn n_{3d} is 4.52 [94,95]. In addition, prior to calculating m_{orb} and m_{spin} using the sum rules, the XMCD intensity must be scaled by a factor of 1.5 due to jj-mixing of the L_3 and L_2 peaks [94,96].

2.8. Vibrating Sample Magnetometry

The macroscopic magnetic properties of samples were examined using a vibrating sample magnetometer (VSM). S. Foner is generally accepted as the inventor of the instrument [97] though the principles for VSM were published earlier by others [98]. VSM operates on the basic principle that a change in flux is measured in a pickup coil when a magnetic sample is vibrated at a constant frequency. The induced voltage in the pickup coil is proportional to the magnetization of the sample. With these principles, the sample and pickup coils can be placed within the gap of an electromagnet and induced magnetization of the sample is measured as function of the applied field.

The VSM used for this research is a system from Quantum Design as part of a physical property measurement system (PPMS). As shown in Figure 2.8, the sample, pickup coil and electromagnet are housed within a cylindrical Dewar with a hollow center which is filled with liquid He. The hollow chamber of the Dewar is evacuated to low vacuum during measurements to help prevent temperature fluctuations during cooling and heating operations. The PPMS is designed to allow for controlled flow of He for precise temperature control and also to reduce unwanted vibrations from spurious He evaporation. The system used here is capable of cooling a sample down to 2 K and heating up to 400 K and fields up to ± 7 T.

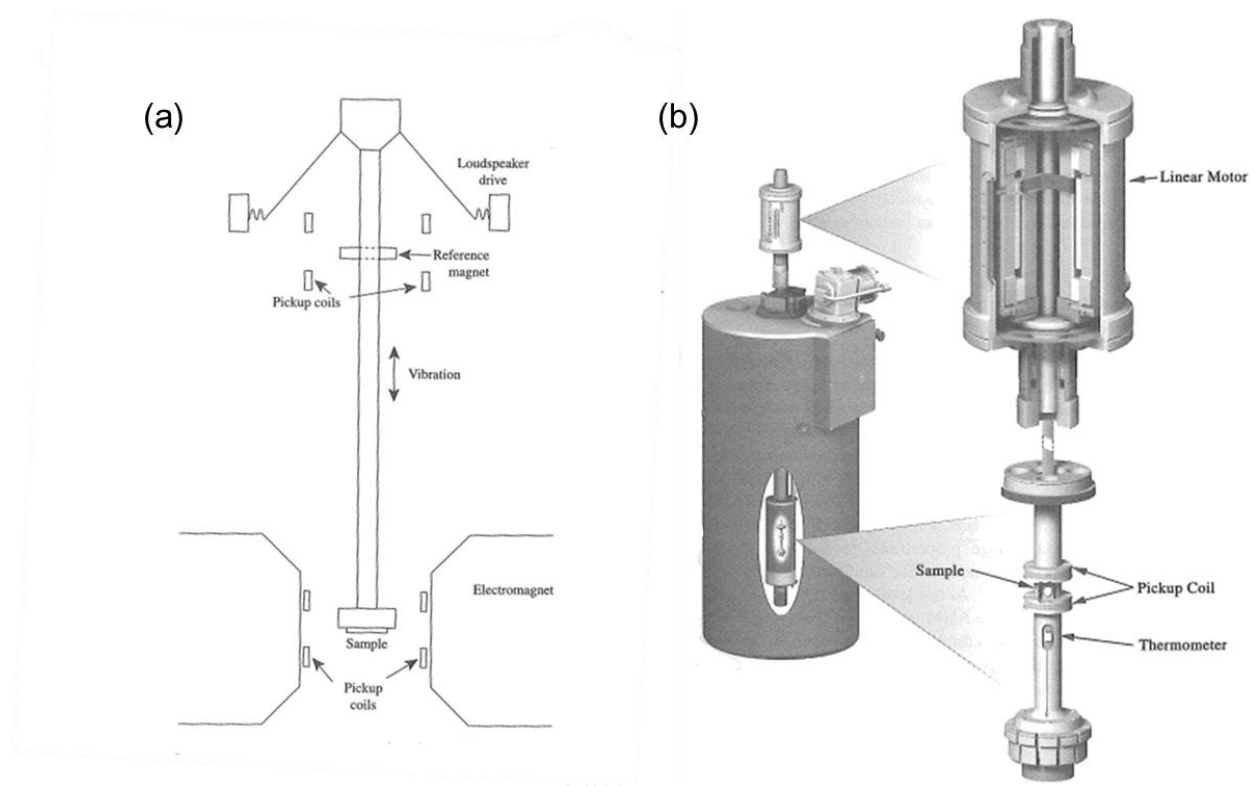


Figure 2.8. (a) Schematic of a vibrating sample magnetometer (VSM) and (b) a diagram illustrating the geometry of the VSM within the Dewar. [99]

Samples grown on the Si(100) substrates were handled with either zirconia ceramic tipped tweezers or Ti tweezers to avoid contamination from the ferromagnetic elements. Samples are mounted on a quartz paddle using wax. The wax is softened at about 100°C and spread out into a thin layer on the quartz paddle. While the wax is still soft, the sample is pressed into the wax gently and observed through the backside of the quartz paddle to ensure there are no trapped air bubbles in the wax. The tools used to handle the sample and the quartz paddle were cleaned before and after use using acetone and ethanol [100]. The importance of eliminating contamination is especially important with the samples in this research. Considering the small sample size (6 mm² deposition area) and low Mn concentration, the magnetic moments expected is on the threshold of detection for the Quantum Design PPMS (magnetic moment <10⁻⁶ emu, noise <10⁻⁷ emu).

2.9. Scanning Auger Microscopy: Scanning Electron Microscopy and Auger Electron Spectroscopy

Spectroscopy

Scanning Auger Microscopy (SAM) is the combination of two other experimental techniques: Scanning Electron Microscopy (SEM) and Auger Electron Spectroscopy (AES). The instrument used for this research is located at the Center for Functional Nanomaterials at Brookhaven National Laboratory. The SAM is part of a commercial system built by Omicron Nanotechnology GmbH. SAM has the capability to spatially resolve composition of samples using the primary electrons from the electron gun. In order to understand the operation of SAM, the basic principles of SEM and AES are first covered in this section.

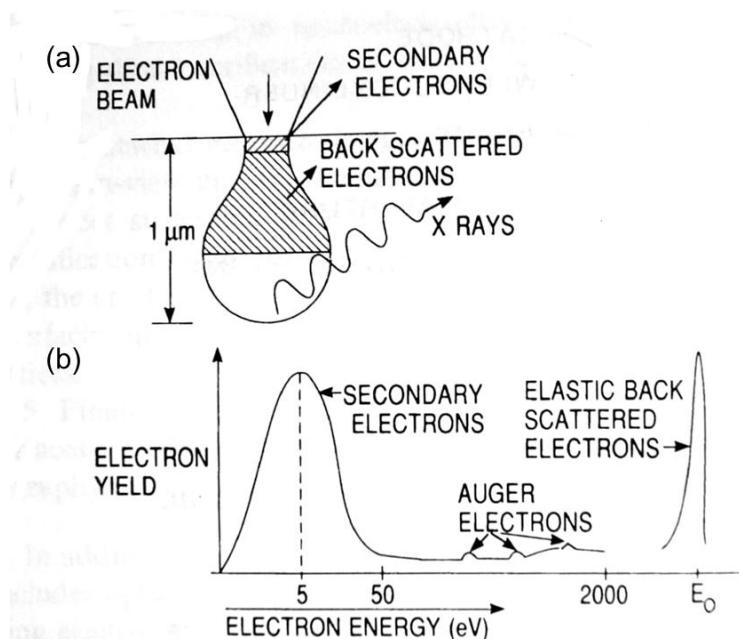


Figure 2.9. (a) A diagram illustrating the interaction volume from an electron beam. The regions where the secondary and backscattered electrons and x-rays is indicated. (b) The energy spectrum of the electrons emitted from a specimen surface. [101]

In a typical SEM, a primary electron beam with energies ranging from 3 keV to 50 keV interacts with a sample and produces secondary and backscattered electrons, x-rays, and Auger electrons. Backscattered electrons are scattered elastically near the surface of the sample and gives z-contrast to the images produced. Secondary electrons are produced from inelastic

scattering and can yield images with highly resolved details without z-contrast. Whether imaging with secondary or backscattered electrons, the primary electron beam is focused down to a small spot size (5 nm) and rastered across the surface with deflection coils within the electron column. When the primary electrons impinge on the sample, scattering events occur with a finite, teardrop shaped, volume beneath the surface. The interaction volume of the electron beam with the sample is illustrated in Figure 2.9. As with other x-ray analysis techniques, in order to obtain Auger spectroscopy the SEM image must be in good focus and well corrected for astigmatism [101].

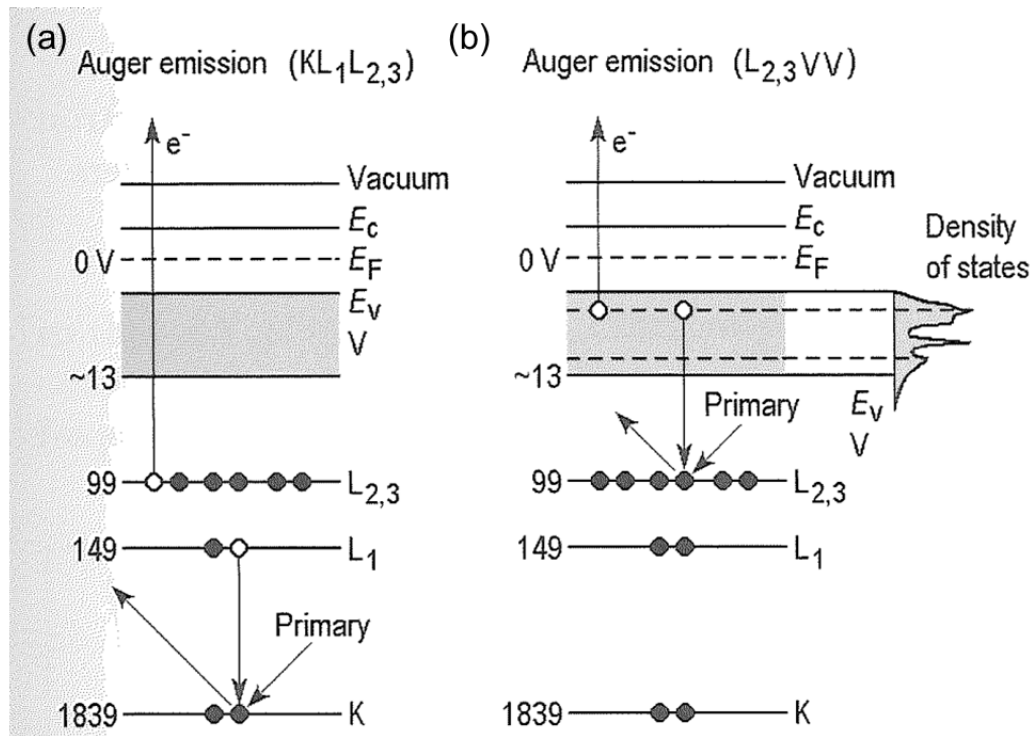


Figure 2.10. Diagram for the Auger process for a (a) $KL_1L_{2,3}$ transition and (b) $L_{2,3}VV$ transition. [19,102]

AES takes advantage of the Auger process to perform elemental analysis of surfaces. As with all electron spectroscopies, AES is highly surface sensitive due to the shallow escape depth of electrons. A typical probe depth, which is dependent on kinetic energy of the Auger electron, is between 10 and 30 Å. A diagram illustrating how Auger electrons are generated is shown in

Figure 2.10. During inelastic scattering interaction with the primary electron beam, a core electron is ejected from the atom. An electron from a higher energy state falls to fill the hole left by the ejected electron and energy can be conserved by radiative or nonradiative process. X-ray emission, which is the radiative process is defined by the emission of a photon with an energy in the x-ray regime, becomes more likely with atoms with a higher atomic number. The nonradiative process is the emission of the Auger electron, another electron is ejected from the atom from a level near or at the same level as the electron that filled the original hole. The atom is then left with two holes. The Auger electron has a characteristic kinetic energy which can be calculated based on the binding energies of the 3 electrons involved in the process [102]. The following equation illustrates this relation for a KL_1L_2 transition Auger electron:

$$E_{KL_1L_2}^Z = E_K^Z - E_{L_1}^Z - E_{L_2}^Z - \Delta E(L_1L_2) \quad 2.6$$

Where E_K^Z is the binding energy of the core electron ejected by the primary electron beam, $E_{L_1}^Z$ is the binding energy of the electron which fills the hole left by the first, and $E_{L_2}^Z$ is the binding energy of the Auger electron. $\Delta E(L_1L_2)$ is a small correction factor due to the fact that the binding energy for the L_2 electron increases when the L_1 electron descends to fill the hole in the K shell. $\Delta E(L_1L_2)$ is a complicated term that can be estimated using the known binding energies at the same levels for an atom one atomic number higher than the one of interest [44], as seen in:

$$\Delta E(L_1L_2) = \frac{1}{2} [E_{L_2}^{Z+1} - E_{L_2}^Z + E_{L_1}^{Z+1} - E_{L_1}^Z] \quad 2.7$$

Auger electron energy analysis, in these experiments, was performed with a 7-channel hemispherical energy analyzer is attached to the chamber with the inlet port facing the sample at an angle of 30° above the sample plane. Primary electron energies of 3 keV, 5 keV, and 10 keV were used to obtain images. The efficiency of Auger electron emission requires that for best

results the primary electron energy should be two to three times greater than the Auger electron peak kinetic energy of interest.

Chapter 3. Mn Wires: Structure and Temperature Stability

This section will explore the room-temperature structure of Mn wires and how the wires evolve in a previously not well studied temperature regime from room temperature up to 400°C. The Mn wires, which form during the room temperature deposition of Mn on a Si(100)2x1 substrate, were described previously by Liu and Reinke [103]. Simov and Reinke performed a more in-depth study of the parameter space required to form Mn wires [104]. Mn wires form when the Mn coverage exceeds about 0.2 ML and the defect concentration is sufficiently low or when defects have condensed into more ordered structures such as dimer vacancy lines. Here the stability of the Mn wires at increasing temperatures is explored, and the behavior of small concentrations of Mn up to temperatures used for Ge QD growth are studied and discussed.

The Mn nanostructure used as a starting point for the annealing experiments were either Mn wires or Mn clusters. Wires are defined here as structures with a high length-to-width aspect ratio, which are in the plane of the substrate surface. This notation refers only to the geometric shape of the nanostructure and does not imply the formation of a 1D electronic or magnetic system with a delocalization of the electrons along the wire. Many different types of wires have been synthesized on semiconductor and metal surfaces, and in general, the driving force for wire formation is an inherent anisotropy in the chosen material combination [28,29,40,42,105–107].

The study of the behavior and interaction of Mn and Si above-room temperature in the literature has focused around temperatures where Mn silicides form, above 400°C [108,109]. We investigated the previously unexplored intermediate temperature regime between room temperature and 400°C. The extent of this section covering the Mn wire temperature evolution has been published in the Journal of Physical Chemistry C [17] and the portion of this section covering the Mn wire structure has been published in part in Surface Science [16].

3.1. Experimental and Modeling Details

Si samples were prepared as described in Section 2.4. This treatment routinely creates a surface with areal defect densities of less than 5%, which are suitable for the formation of Mn-wires [103,104]. All STM images were obtained in constant current mode with a sample bias of -1.5 V (filled states) and +1.5 V (empty states) and a feedback current of 0.03 nA. Electrochemically etched W wire was used as a tip material. Image analysis was performed using ImageJ [110] and WSxM [111] software packages.

Mn was evaporated from a Mo crucible using a home built electron beam evaporation source, and the deposition rate was calibrated using a quartz crystal monitor placed at the sample position and produced a flux of 0.025 Å/s. The Mn coverage (Θ_{Mn}) was obtained from STM image analysis after deposition and determined to be in the sub-monolayer regime. Mn was deposited at room temperature, and the sample was then annealed by direct current heating at temperatures between 100 – 600°C for 5 minutes (a new sample was used for each temperature). The approximate annealing temperature is reached within a few seconds of adjusting the heating current. The temperature calibration for small Si samples (10 x 1 x 0.5 mm) in this intermediate temperature regime is notoriously difficult. The sample size is too small and the annealing temperature too low for a reliable pyrometric measurement. In addition contact with a thermocouple greatly diminishes the quality of the surface due to the presence of transition metal contaminants [112–114]. The temperature was therefore calibrated by establishing the relation between temperature and heating power with a sacrificial sample contacted with a K-type thermocouple. The calibration power/current-temperature curve used to determine the annealing temperature of all samples is shown below in Figure 3.1.

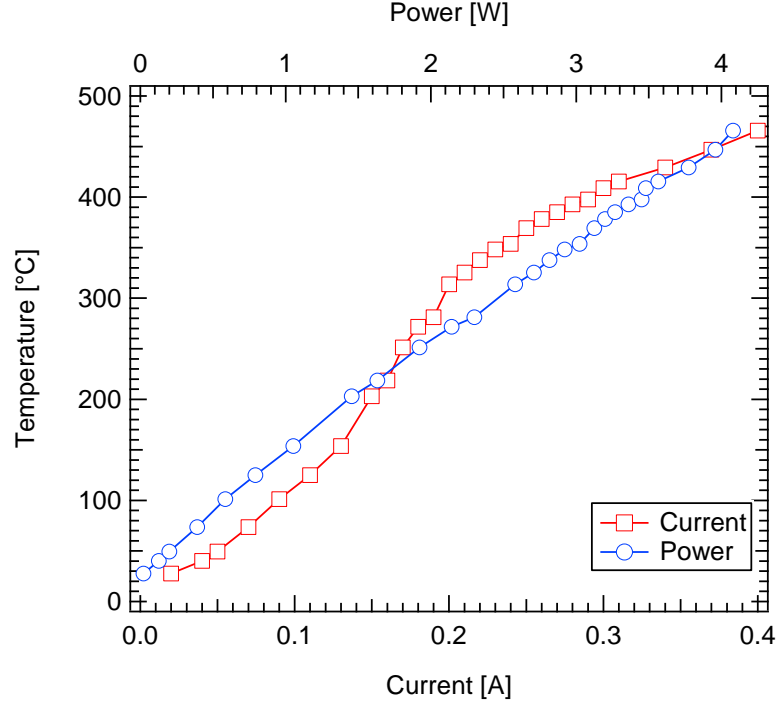


Figure 3.1. Temperature measurement of a sacrificial sample as a function of the current/power supplied to the sample. The sacrificial sample had a resistance across the sample holder of 104.9Ω , and a visual deep red glow at the sample was observed at 415°C .

The structure of the Mn wires was analyzed from both experimental images and modeling through collaboration with P. Kratzer and M. Hortamani of the University of Duisburg-Essen and the Max Planck Institute of Microstructure Physics, respectively. Effectively the models proposed with our collaborators are two bonding configurations and simulated STM images of those configurations. The simulated STM images were compared to experimental images to determine their validity in terms of the relative atom positions and the variation of image contrast as a function of bias voltage. The Mn wires on Si(100) were modeled using a periodically repeated slab in a (2x4) unit cell (with a periodicity of 2 lattice constants along the wire). Density functional theory (DFT) total-energy calculations are performed using the Perdew-Burke-Ernzerhof (PBE) functional for electronic exchange and correlation and the linearized augmented plan wave and local orbital (LAPW+lo) approach to electronic structure calculations, as implemented in the WIEN2k computer code [115]. The structures were fully relaxed until the

forces on each moveable atom are smaller than $0.05 \text{ eV}/\text{\AA}$. STM images were simulated within the Tersoff-Hamann approximation [85] by integrating the electronic density of states in an energy interval between the Fermi energy ε_F and $\varepsilon_F + V$, where V is the sample bias voltage. Subsequently, the height above the surface for an iso-contour surface of $8 \times 10^{-5} \text{ eV}/\text{\AA}^3$ was calculated and plotted.

Sample Label	Θ_{Mn} (ML)	T_{Anneal} ($^{\circ}\text{C}$)	RT Mn Structure
S115	0.04	115 ± 28	Clusters
S268	0.14	268 ± 30	Wires
S316	0.12	316 ± 38	Wires
S342	0.22	342 ± 38	Wires
S415	0.04	415 ± 44	Clusters
S600	0.4	600 ± 44	Wires/Clusters

Table 3-A List of sample parameters

The samples, which were used to study the temperature evolution of the Mn nanostructures, are listed in Table 3-A. The samples are labeled by their respective annealing temperature $S(T_{\text{anneal}})$. One additional sample was prepared by Mn deposition ($\Theta_{\text{Mn}} = 0.2 \text{ ML}$) on a heated substrate at 600°C , named SH600. The quality of the Si surface was characterized by the density of defects per unit area (nm^{-2}), the relative area of the surface occupied by defects and the quality of both types of step edges, S_A and S_B .

The step edge quality was evaluated by determining the dimer interaction energies using Boltmann statistics and counting the number of dimers between kinks of the step edge. The dimer interaction energies can be determined from real space images by counting the number of kinks with a given depth. The first nearest ($\varepsilon_{\text{Sa(b)}}$) and second nearest (δ) neighbor dimer

interaction energies for S_A and S_B type steps were determined from STM images following the procedure described by Zandvliet et al: [116,117]

$$\frac{\varepsilon_{Sa(b)}}{k_b T_f} = -\ln\left(\frac{n_{+1}n_{-1}}{n_0^2}\right) \quad 3.1$$

$$\frac{\delta}{k_b T_f} = -\ln\left(\frac{n_{\pm r}n_0}{n_{\pm(r-1)}n_{\pm 1}}\right), r \geq 2 \quad 3.2$$

The number of kinks, $n_{\pm r}$ of length $2ar$ ($2a$ is the center-to-center distance between dimers along the direction perpendicular to the dimer axis, r is the number of dimers in a kink), and the number of sites with no kinks, n_0 , were measured along S_A and S_B step edges. Two different kink directions are defined as following: a kink protruding towards the lower terrace as a positive kink (n_{+r}), and a kink protruding towards the upper terrace as a negative kink (n_{-r}). Representations of n_0 and n_{-r} in a diagram are shown below in Figure 3.2.

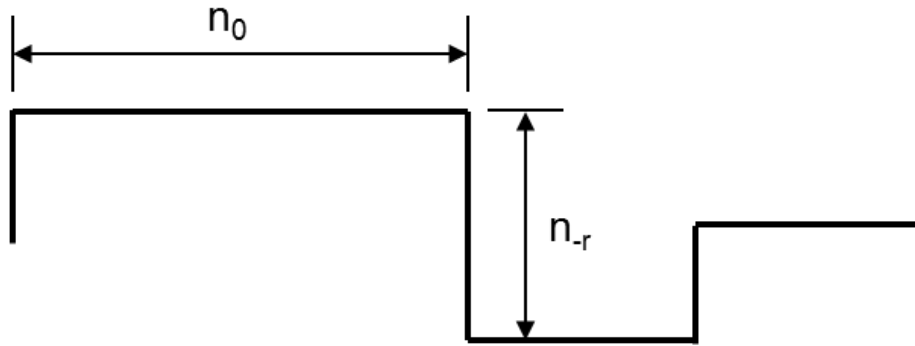


Figure 3.2. A diagram illustrating a step edge with kinks. A straight, unknicked, section of the step edge is measured and represented by n_0 . A negative kink, one protruding into the step edge, is measured and represented by n_{-r} .

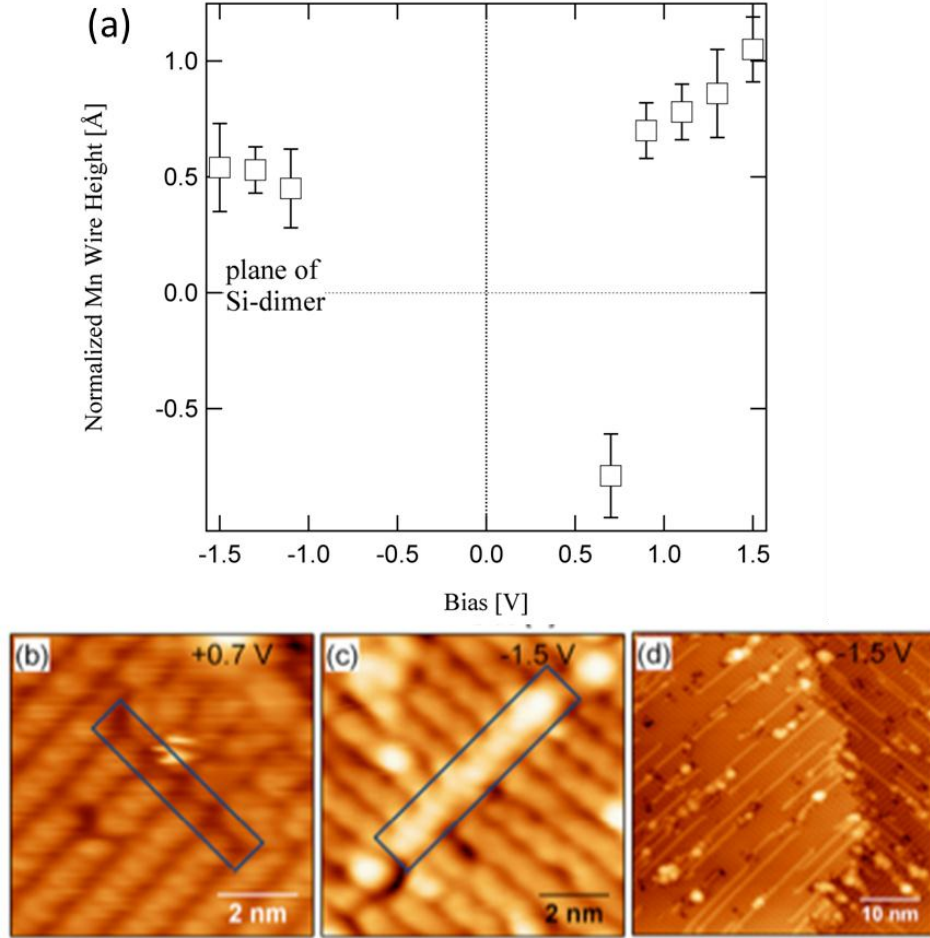


Figure 3.3. (a) The height of the Mn-wires is depicted as a function of bias voltage [empty (+) and filled states (-)]. The height is given with respect to the plan of the Si-dimers. The graph contains data from images measured in two independent experiments and the deviations between these two datasets is included in the error bar. In the region between 0.7 V and -1.1 V the image quality is insufficient to determine the Mn-wire height. (b) and (c) are representative experimental STM images for 0.7 V and -1.5 V; the wires are outlined with a box. Part (d) shows a larger scale image of Mn-wires on the Si(100)2x1 surface.

3.2. Mn Wire Structure

Figure 3.3 shows experimental images for the empty state (0.7 V, Figure 3.3(b)) filled state (-1.5 V, Figure 3.3(c) and (d)). The filled state image at -1.5 V delivers the best overall image quality, and the surface structure remains unchanged until the bias voltage drops below -1.0 V. The comparison of images recorded from -1.5 to 1.5 V in small increments is summarized in Figure 3.3(a) and reveals a contrast inversion around a bias voltage of 0.7 V (empty states). The quantitative analysis of the apparent wire height with respect to the plane of the Si-dimers is

included in Figure 3.3. The strong voltage dependence of the Mn-wire images was observed repeatedly for several samples and with different STM tips, and is independent of the local Si(100) reconstruction around the wire, which can adopt either a (2x1) or p(2x2) reconstruction. The same wire is imaged with different bias voltages and the contrast inversion is therefore characteristic of the specific LDOS and bonding configuration in the Mn-wire-Si system.

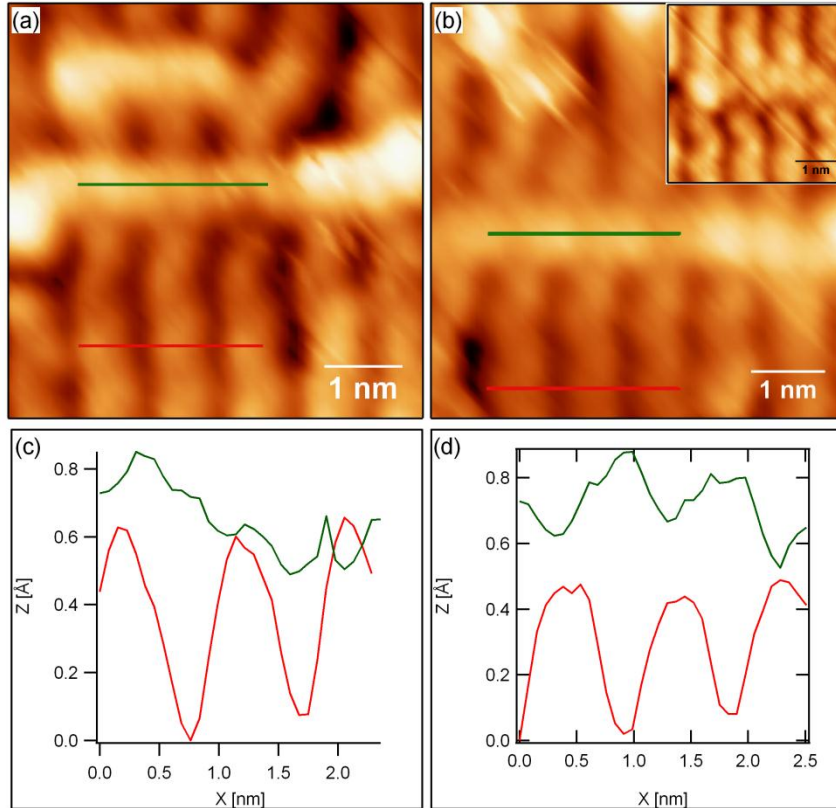


Figure 3.4. (a) Mn wire and (c) linescans across Si-dimer rows (red) and Mn-wire (green), which illustrates the lack of an offset between the Si-dimer rows and the Mn-wire maxima. (b) STM image of a Mn wire with an offset between the Mn wire and the Si dimers, the corresponding linescan shown in (d). An exceptionally well resolved Mn wire is shown in the inset of (b). All images at an imaging bias of -1.5V.

Figure 3.4 illustrates the relative position of the maxima of the Mn-wire with respect to the Si-dimer row, and the image, Figure 3.4(b), shows the most abundant type of Mn wire. The maxima in the Mn-wire structure are positioned “in between” the Si-dimer rows, as can be seen in the respective linescans (Figure 3.4(d)). Occasionally an exceptionally well-resolved Mn-wire image can be obtained, and the single atoms positioned along its backbone can be distinguished (Figure

3.4(b) inset). This image implies that the relatively large protrusions along the Mn-wire backbone are composed of two atoms each. The relative position of the Mn-wire maxima to the Si dimers rows are referred to as an offset between the Mn wire and the Si dimers.

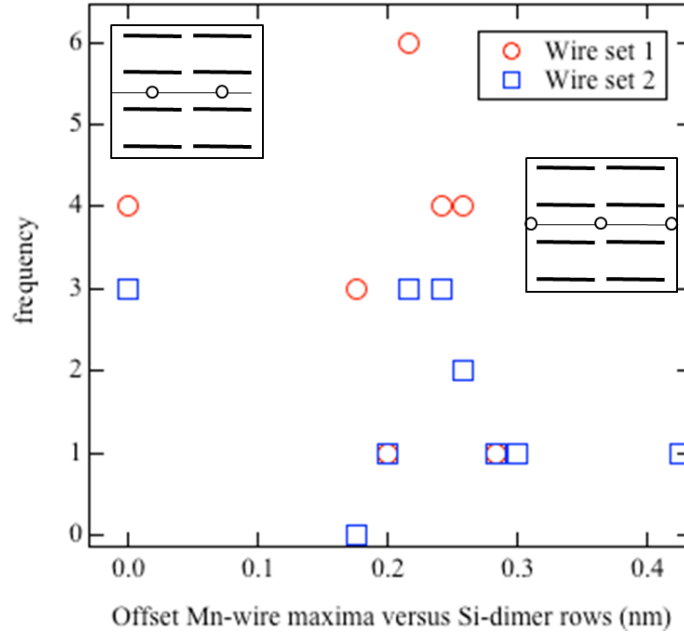


Figure 3.5. Distribution of wire offset for 37 wires from two independent experiment (“wire set 1”, “wire set 2”). The data point at 0 nm offset are Mn wires whose maxima are in registry with the Si dimer rows. The set of data point centered at 0.25 nm corresponds to the mean offset of Mn wire maximas relative the Si dimers. The error in the measurement is estimated to be about ± 0.02 nm.

The average offset of the Mn-related protrusions is 0.22 nm with a minimum offset at 0.18 nm and these results are summarized in Figure 3.5. The histogram of the offset represents a set of 37 wires measured in two independent experiments, which were performed about a year apart. A second type of wire, where the maxima in at least part of the wire-structure coincide with the maxima in the Si-dimer rows, is shown in Figure 3.4(a) and (c) and is observed with a frequency of about 20% of the total wire population. These wires might be best described as defective wires, where the preferred position of Mn-adatoms in between Si-dimers cannot be achieved. In Figure 3.4(a) the linescan for the Mn wire (green) shows a coincidence of Mn-wire and Si-dimer maxima for the first two Mn-adatoms, but not for the last adatom in the wire. This is indeed

typical, and the defective wires are sometimes positioned between defects or surface clusters, which strengthens our argument that they might be forced into an energetically unfavorable position by geometric constraints.

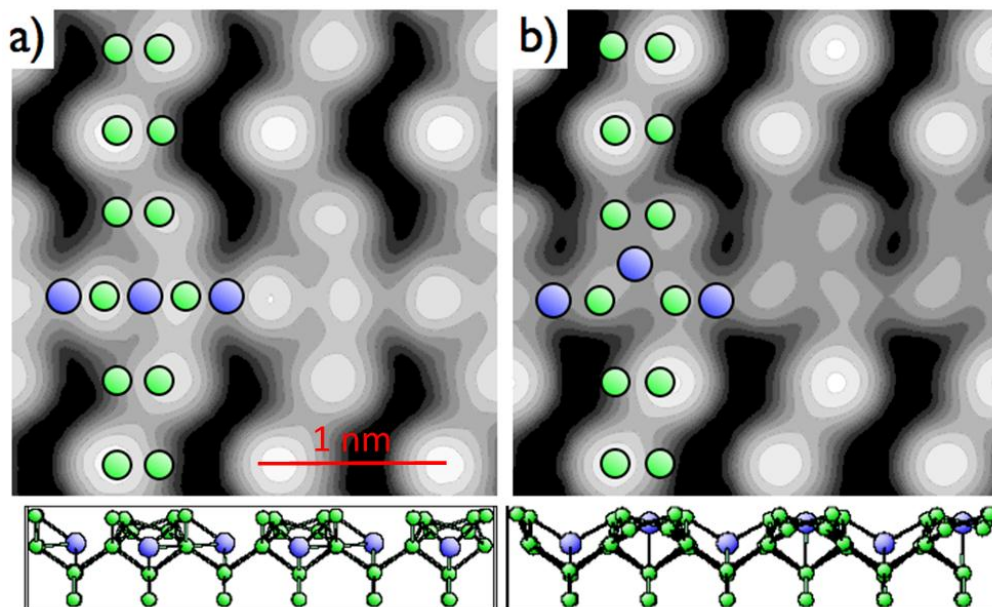


Figure 3.6. Simulated filled state STM images for a sample bias of -1.1 V for two Mn wire structures: (a) Mn in a subsurface and cave positions (sub-cave) and (b) Mn in hollow and cave positions (hollow-cave). The ball-and-stick models with Mn (blue circles) and Si (green circles) are seen as an overlay on the simulated STM images. A side view of the model is shown below (a) and (b) for each structure.

In order to find a structural model for the wires, five atomic structures with different chain-like arrangements of the Mn-atoms were analyzed by means of DFT calculations. After relaxation the sub-cave and the hollow-cave structure, shown schematically in Figure 3.6, emerged as the thermodynamically most stable structures. The wire is seen in these filled-state images (-1.1 V) as the feature running horizontally through the image, perpendicular to the Si dimer rows. The sub-cave structure, which is the thermodynamically most stable structure of the two, is a periodic chain of Mn atoms in the sub-surface site and in the cave-site. In the hollow cave structure, the second most stable structure, the Mn atoms alternatingly occupy the hollow

site and the cave site; for the terminology of the bonding sites we refer to previous work by Hortamani et al. [118] also as shown in Figure 3.7.

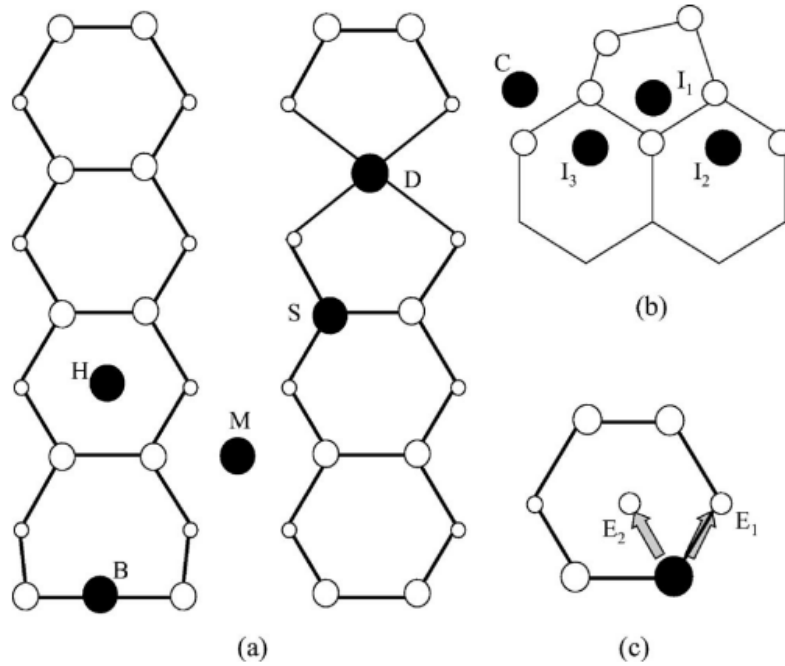


Figure 3.7. A schematic of the Si(100) surface (open circles) and the possible binding sites for Mn (filled circles) is illustrated. (a) A top down view of the Si(100)2x1 surface where Mn is located in a dimer vacancy (D), substitutional (S), a dimer long bridge (M), hollow (H) and a dimer short bridge (B) site. (b) A side view of the Si(100)2x1 surface and possible Mn binding sites. The cave site (C) is located between dimer rows and the interstitial site (I₁) sites one layer below the surface. The other two interstitial sites (I_{2,3}) are located within the third layer below the surface. (c) Depicts the displacement of a Si atom in the event of Mn entering a substitutional site [118].

The sub-cave structure shows a clear corrugation along the Mn-wire, which has about the same height as the plane of the Si-dimers, and it appears as a depression for empty states in a narrow voltage region around 0.7 V. The theoretical images reproduce to some extent the contrast change already described for the experimental images albeit the magnitude of the height change as a function of bias voltage is smaller. The origin of the disagreement between theory and experiment in the magnitude of the apparent height change with bias voltage remains unresolved, albeit we suspect that tip induced band bending might play a role.

The theoretical image for the sub-cave structure in Figure 3.6 shows a bright feature at an offset of 0.18 nm, which reflects the contribution from the Si-atom closest to the Mn-atom and is

the offset marked in Figure 3.5 for a direct comparison with the experimental results. These show on average a slightly larger offset, which can be attributed to a small contribution from the Mn-atom (positioned at the center between the Si-dimer rows) to the local density of states, and is not reflected in the theoretical images. The agreement between the experimental STM images and the sub-cave structure is relatively good, albeit we are currently not able to unambiguously resolve all remaining discrepancies.

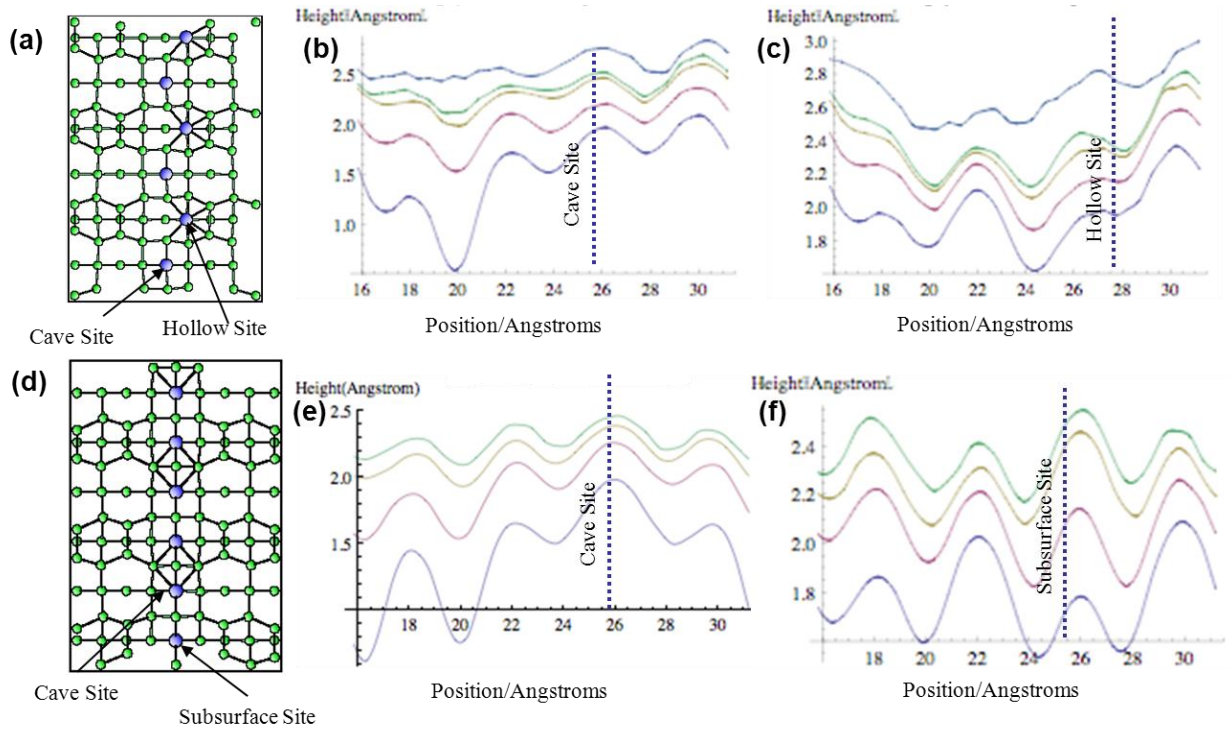


Figure 3.8 A summary of line scans across simulated structures are shown here. In (a) the top-down ball and stick model of the hollow-cave structure on Si(100) is shown. The associated line scans run perpendicular to the Mn wire structure and intersect with the respective Mn site. In (b) the line scans intersect with the cave site of the hollow-cave structure. The line scans are shown for different simulated bias voltages (top to bottom) from 1.3 V to 0.5 V in 0.2 V increments. Similarly in (c) line scans intersecting with the hollow site Mn is shown. In (d) the top-down ball and stick model for the sub-cave structure on Si(100) is shown. The line scans intersecting the (e) cave site Mn and (f) subsurface site Mn show varying simulated bias voltage (top to bottom) from 1.1 V to 0.5 V.

The bias voltage induced simulated structure dependence of the simulated structures is further illustrated in Figure 3.8. The ball and stick models for the hollow-cave and sub-cave structures are shown in Figure 3.8(a) and (d), respectively. Line scans across the two different Mn sites for

each structure are used to illustrate the contributions of the Mn wire and local bonding to the contrast. In Figure 3.8(b),(c),(e), and (f) the respective Mn site is noted with the vertical dotted line. For Figure 3.8(b) and (c) the bias voltage of the simulation is varied from 1.3 V to 0.5 V (top to bottom) in increments of 0.2 V. Similarly, Figure 3.8(e) and (f) line scans are varied in bias voltage from 1.1 V to 0.5 V (top to bottom) in increments of 0.2 V. The larger periodic protrusions in each set of line scans separated by 4 Å are the Si atoms of the dimers. Though one can see an influence of Mn in the structure across the line scans, the apparent height as a function of bias voltage is small.

3.3. Mn Wire Temperature Evolution

Following the room temperature deposition of Mn on Si(100)2x1, annealing steps lead to dramatic changes in the Mn nanostructures and bonding to the surface. A considerable modification of the Si-surface itself also occurs, and includes changes in the defect concentrations, dimer vacancy density, condensation of dimer vacancy lines and the step edge roughness. The changes in the Si surface at elevated temperatures are indicative of the specific interaction of Mn with a Si-surface and reminiscent of the interaction of Si(100) surfaces with Ni [112,113,119].

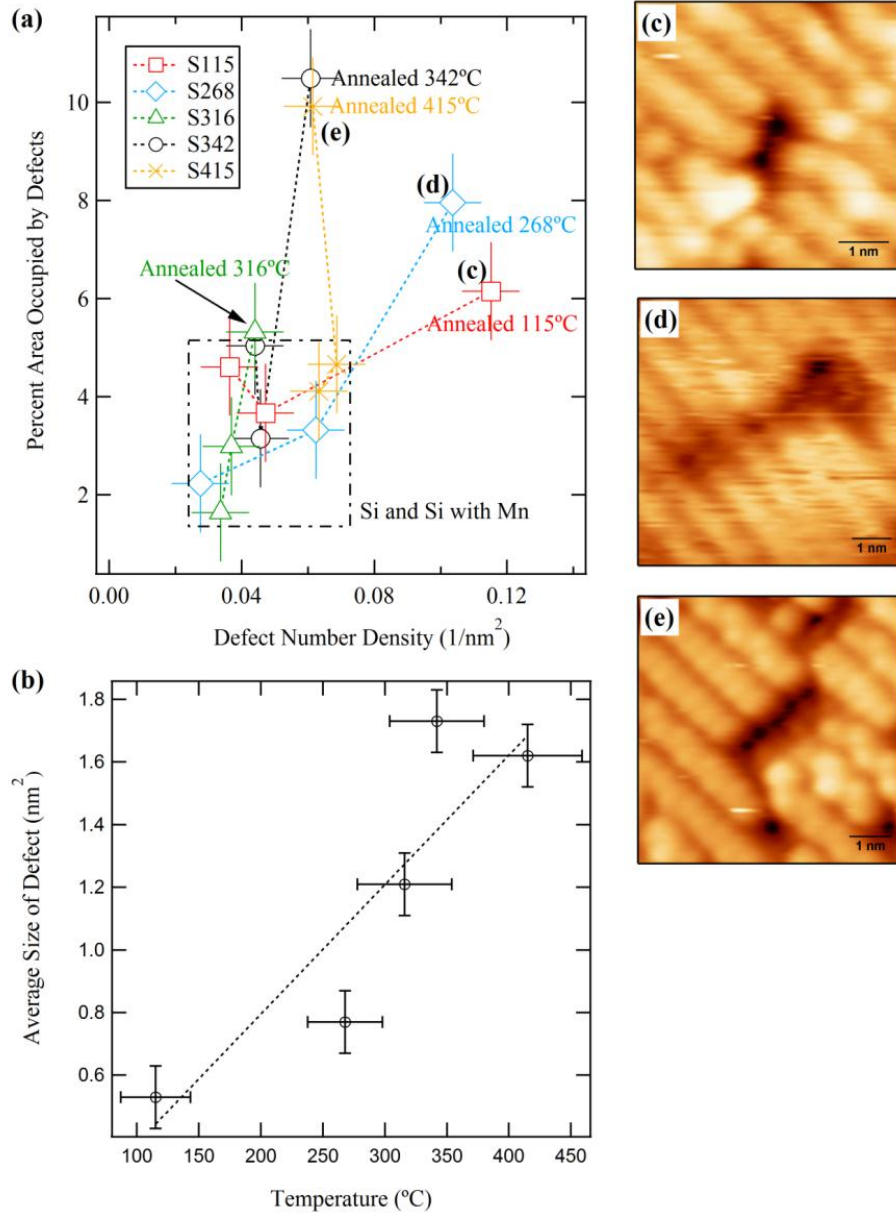


Figure 3.9. (a) Change in defect morphology characterized by defect number density and percent area covered by defects. The area enclosed by the box contains the measurements for the Si(100)2x1 surface before and after room temperature Mn-deposition. (b) Average defect size as a function of annealing temperature. A single dimer vacancy occupies an area of $0.309 \pm 0.028 \text{ nm}^2$. STM images of representative defect structures observed after annealing: (c) S268, (d) S316, and (e) S415. These defect images show the filled states (-1.5 V bias voltage).

3.3.1. Silicon Surface

The surface defect structures on Si(100)2x1 are quantified by their density, the percentage of surface area covered by defects, and the average defect size. These data are summarized in Figure 3.9(a) for samples S115, S268, S316 and S415 before and after the deposition of Mn and

after the annealing step. Prior to the Mn deposition the area defect densities lie between 1.5 and 4.5%, and the defect number densities were limited to 0.04 to 0.06 per nm². Representative images of defect structures are shown in Figure 3.9(c-e). A slight increase in the Si-defect density was observed after the deposition of Mn at room temperature. The defects are mainly single and double dimer vacancy defects, which have been described in detail in numerous publications [120–122].

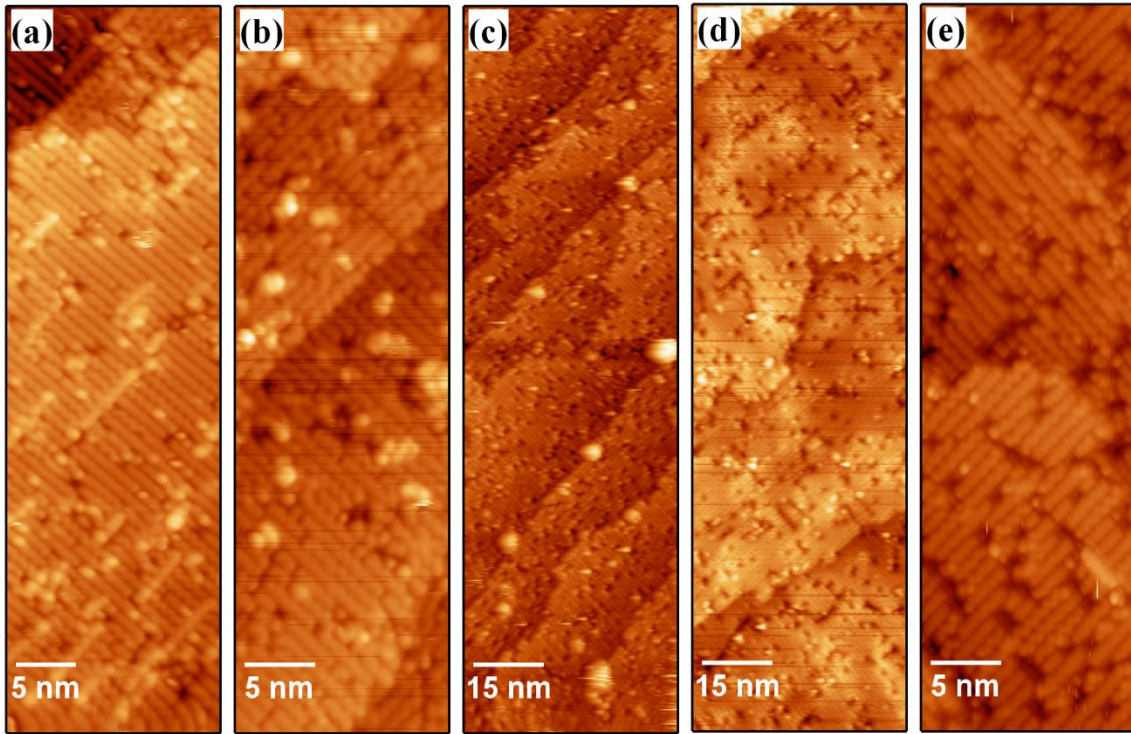


Figure 3.10. STM images of Si(100)(2x1) - Mn samples (a) before annealing of sample S316, after annealing: (b) S115 (-1.5 V), (c) S268 (-1.5 V), (d) S316 (+1.5 V), and (e) S415 (-1.5 V bias). All images acquired at room temperature.

As shown in Figure 3.9 for the first two annealing steps, S115 and S268, we observe a considerable increase in the number density of defects with annealing but the area occupied by those defects increases only slightly. As with the before annealing samples, the defects are generally isolated single and double DVs (dimer vacancies); for S268 an increase in defect area and size (Figure 3.9(b)) indicates the onset of defect agglomeration. The growth of defects and

condensation of DVs into Dimer Vacancy Lines (DVLs) continues for S316 (Figure 3.9(d) and Figure 3.10(d)) but this sample also exhibits a unique bonding situation for the Mn-Si surface, which might change defect formation and stability (see section 3.3.2).

For higher annealing temperatures, S342 and S415, the DVLs continue to grow, and the area occupied by the defects and defect size (Figure 3.9(b)) increases considerably, albeit the DVLs are still relatively short with many kinks and crooked sections (Figure 3.10(e)). The average size of the defects as a function of annealing temperature reflects the condensation of multiple DV structures into extended DVLs. This is most dramatically seen in S600, which is shown in Figure 3.11(a), where the DVLs extend almost across the entire width of the individual terraces.

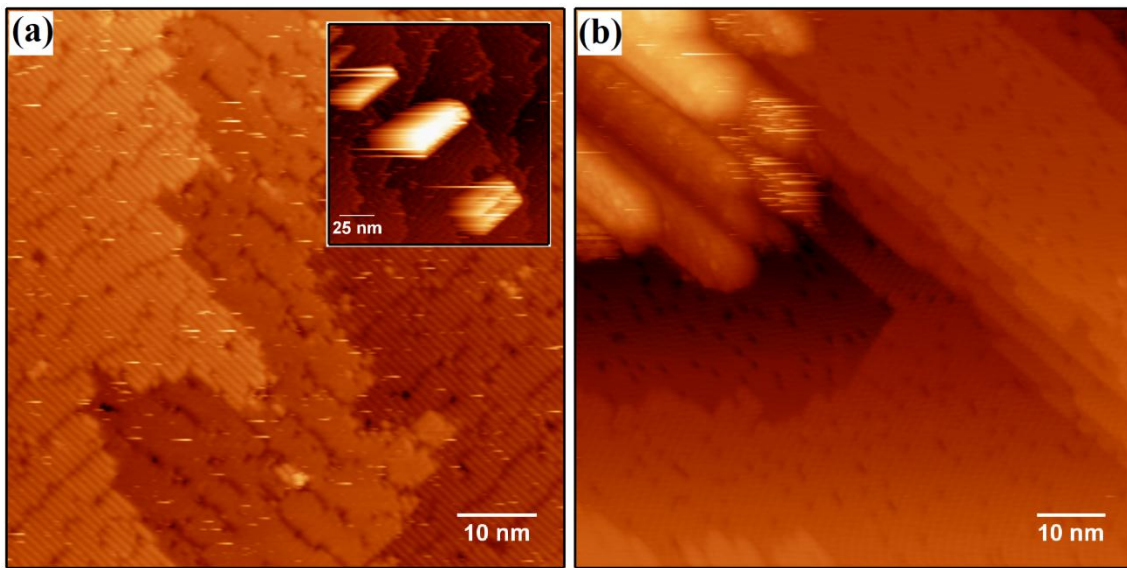


Figure 3.11. Representative STM images of the two high temperature samples (a) S600 and (b) SH600. All images were obtained at room temperature.

Figure 3.12(a) shows the average number of dimers between kinks for step edges S_A and S_B , and gives a measure of the roughness of the step edges as a function of annealing temperature. On the S_B step the number of dimers between kinks is small, and decreases from only 2.7 to 1.7 dimers between kinks with increasing sample temperature, while on the S_A step the unkinked length decreases by an order of magnitude over the same temperature range. This development is

also seen in the STM images shown in Figure 3.10. The dimer interaction energy was calculated to obtain a quantitative measure of the influence of Mn on the evolution of S_A and S_B step edges as a function of annealing temperature. The nearest neighbor interaction energies of a clean Si(100)2x1 surface are $(7.0 \pm 0.2)k_b T_f$ and $(3.9 \pm 0.2)k_b T_f$ for the S_A and S_B step edge, respectively, where T_f is the freeze-out temperature of step edge adatom mobility. The freeze-out temperature is a thermodynamic value where there is enough energy for the generation of kink pairs at the step edges. The values for dimer interaction energies (Equation 3.1) on the Si(100)2x1 surface prior to Mn deposition can be directly compared to the literature: the value obtained for the S_B step edge is in good agreement with the value reported by Zandvliet, $(3.6 \pm 0.2)k_b T_f$ [117]. However, our value for the S_A step edge exceeds the value given by Zandvliet $(5.7 \pm 0.3)k_b T_f$ [117], which corresponds to a smaller number of single kinks on our sample. Due to the low number of kinks on a S_A step edge, the nearly straight step edge on a clean surface, calculations of these energies terms can be difficult to compare across different samples and experiments.

Sample Label	Dimer Interaction Energy [eV/eV]	
	S_A Step Edge	S_B Step Edge
S115	5.5 ± 0.3	4.0 ± 0.3
S268	4.2 ± 0.3	3.4 ± 0.3
S316	3.6 ± 0.4	2.4 ± 0.4
S342	2.6 ± 0.4	3.3 ± 0.4
S415	2.8 ± 0.3	1.8 ± 0.3

Table 3-B Dimer interaction energies of S_A and S_B step edges

The freeze-out temperature for step edge on a pristine Si-surface is given as 350 to 450°C in the literature and below this temperature the step edge is stable [123–125]. However, the

substantial changes in the edge roughness at an annealing temperature below 350°C might be indicative of a lower freeze-out temperature and we can therefore not use the value of T_f of the pristine Si surface. All dimer interaction energies are therefore given as multiples of $k_b T_f$ (see Equation 3.1). The values listed in Table 3-B were determined for the samples after annealing with Mn.

Using these values, the step edge formation energy was calculated according to Equation 3.3 and Equation 3.4. In Figure 3.12(b) the step edge formation energies are illustrated as a function of sample annealing temperature. The S_A step edge formation energy remains at 0.9 eV/ $k_b T_f$ per kink atom constant within the margin of error, and is positioned at the higher end of literature values, which range from 0.74 – 0.9 eV/ $k_b T_f$ per kink atom [117]. For the S_B step, the formation energy decreases with increasing annealing temperature up to sample S342 where it reaches a steady state value of 1.29 eV/ $k_b T_f$ per kink atom.

$$\frac{E_{Sa}}{k_b T_f} = \frac{\varepsilon_{Sb}/k_b T_f}{2} + \frac{\delta}{k_b T_f} \quad 3.3$$

$$\frac{E_{Sb}}{k_b T_f} = \frac{\varepsilon_{Sa}/k_b T_f}{2} + \frac{\delta}{k_b T_f} \quad 3.4$$

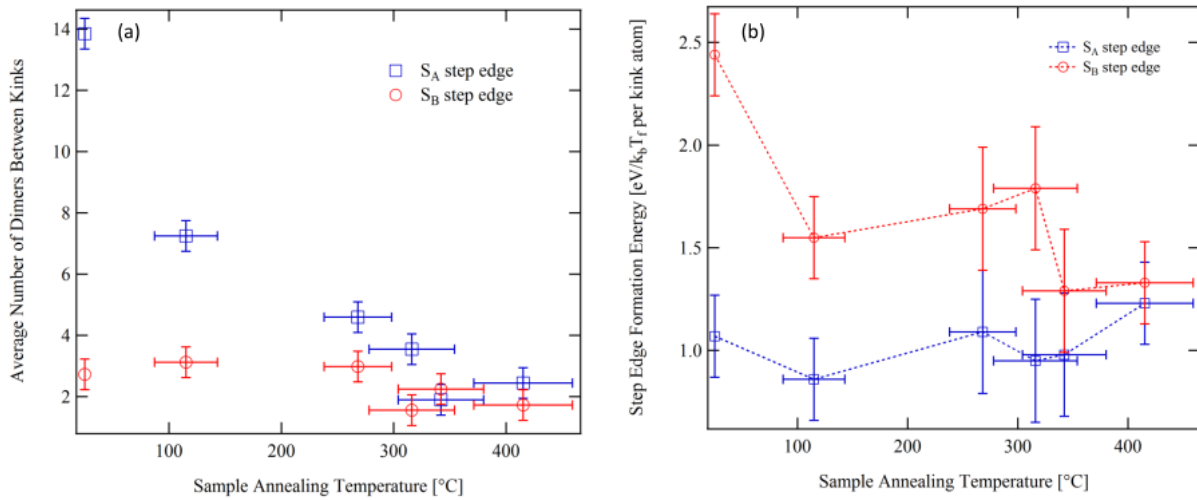


Figure 3.12. (a) The average number of dimers between kinks along an S_A and S_B type step edge. (b) Step edge formation energy of S_A and S_B steps as a function of the sample annealing temperature. The data point at 25°C corresponds to a representative clean Si(100)(2x1) surface after *in-situ* cleaning.

3.3.2. Manganese Surface Structures

The evolution of the Mn-surface structures with annealing (Figure 3.10) begins with a transition from the Mn-wire structures to clusters, which is followed by the movement of Mn into sub-surface sites. Finally, Mn transitions to forming larger crystallites. The Mn-wires and adatoms for all samples are distributed randomly on the Si-terraces prior to annealing. The ultra-small Mn-structures observed on S115 prior to annealing contain only 1-4 atoms (average size 0.22 nm^2) and can be considered the critical nuclei for wire formation if the Mn-deposition is continued. The subsequent annealing leads to the formation of larger islands with a broad size distribution, which extends from 0.22 nm^2 to clusters as large as 3.16 nm^2 . The clusters are distributed randomly across terraces, and did not display a preference for nucleation on the step edges. Measurement of exact cluster sizes in STM is rather unreliable for cluster diameters below 10 nm due to the convolution of the image with the tip shape. Fortunately, for S115 the smallest islands/clusters are only a single atom high, and the measurement of the diameter of these structures is still accurate. Clusters imaged on S268, were often much higher, and the

numbers given here present only a rough estimate of the cluster size. For S268 the average cluster size is considerably larger, the ultra-small clusters are missing, and the clusters range in size from 2.56 nm^2 to a maximum size of 36.25 nm^2 (23 clusters measured in total).

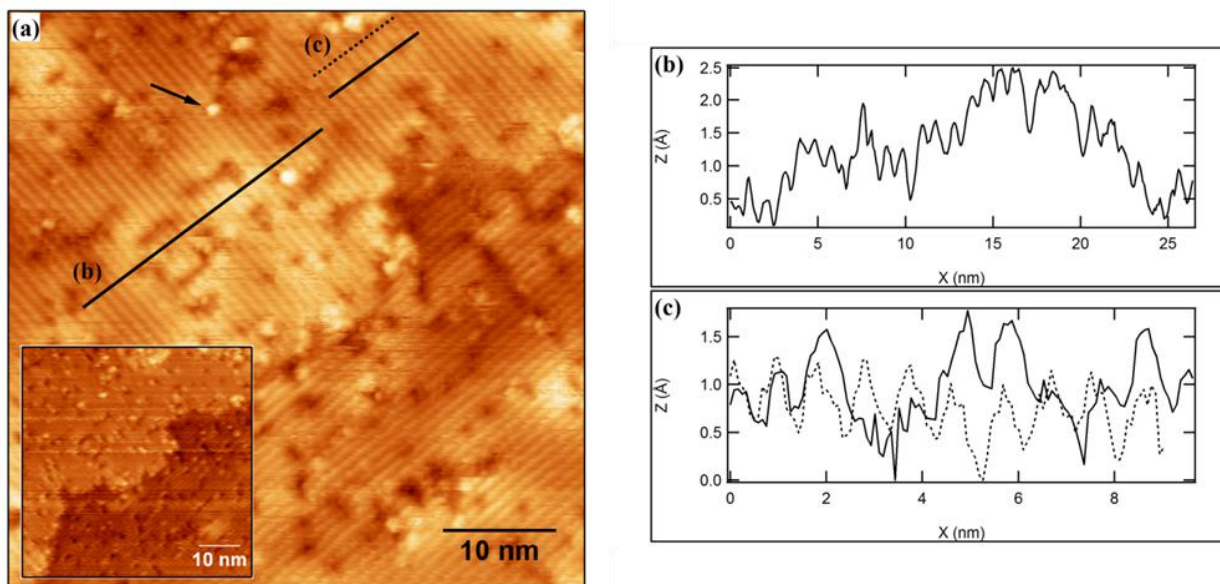


Figure 3.13. (a) STM image of S316 after annealing. The large image shows the empty states (+1.5V), and the inset depicts the filled state (-1.5V) image for the same area. (b) Representative line scan across a high contrast region, where the reconstruction is preserved and the apparent height is modified. The change in apparent height is indicative of subsurface Mn, which acts as an electronically active dopant. (c) Line scans across a region without enhanced contrast: the broken line is perpendicular to the dimer rows, the solid line crosses two dimer vacancy defects. The arrow marks a C-type defect.

S316 displays a different surface morphology, which is shown in Figure 3.13(a). This image is representative of the surface structure of S316 and taken at a bias voltage of +1.5 V, which probes the empty states. The filled state image taken at -1.5 V of the same area is shown in the inset; S316 is the only annealing stage where the filled and empty states exhibit marked differences. The majority of surface defects and extended defect structures are surrounded by regions of enhanced brightness in the empty state images (larger apparent height), which is also reflected in the line scans included in Figure 3.13(b,c). The extension of these areas is about 3-4 equivalent dimer widths, and the line scans clearly show that the Si-reconstruction is preserved. The appearance of the contrast pattern is markedly different from the representation of dangling

bonds, which are commonly observed at DV defects. Some of these spatially confined defects, C-type defects, can be seen in Figure 3.13(a) (marked with an arrow). The preservation of the dimer reconstruction and the pronounced differences between the filled and empty state images is commensurate with an electronic rather than a topographic modification of the surface.

For the next two annealing steps, S342 and S415, different surface structures coexist, which include large crystallites extending several tens to a hundred nanometers and small clusters similar to those observed at lower temperatures. These different surface structures are interspersed by large regions of Si(100)2x1 with extended DVLs. The STM itself is not sensitive to the chemical composition of the clusters, but previous studies, which focused on this high temperature regime, demonstrated the formation of silicide crystallites albeit of varying stoichiometry. [108,109] The coexistence of different crystallites and surface structures is characteristic of the high temperature regime, and is even more pronounced in S600 as shown in the inset of Figure 3.11(a). Sample S415 links the intermediate temperature regime, which is the focus of our study, to the high temperature regime described in several other publications. [109,126–128]

3.4. Discussion

The discussion section is presented separately for the portions reflecting the structure of the Mn wires, the changes in the silicon surface due to the presence of Mn, and the evolution of the Mn nanostructures with annealing temperature.

3.4.1. Mn Wire Structure

The contrast inversion is at first sight reminiscent of STM images of Si-dangling bond states, which form in the vicinity of a missing dimer or atom defect in the Si-dimer rows. The Si-dangling bonds contribute a well-defined narrow state close to E_F and are seen as protrusions

adjacent to a defect site in the empty state images, but are not visible in the filled state images [120]. The Mn-wire states, however, show the opposite behavior as summarized in Figure 3.3. Si-dangling bond states cannot be seen in images where the Mn-wire presents as a protrusion. The Mn-d-band is relatively flat and featureless in the vicinity of E_F and thus unlikely to be the origin of the rapidly changing local density of states on the wire with bias voltage. We therefore suggest that the states, which define the images of the wire structure are mixed Mn-Si states, either through a hybridization between the Mn d-states and the Si-p states, or backbonding from Mn-d electrons into the broken Si-dimer bond.

Previous theoretical studies focused on the bonding of isolated Mn structures [118,129] and Mn-layers to Si(100) surfaces. The sub-surface site for Mn was identified as the thermodynamically most stable bonding geometry [118,130] and annealing of Mn-clusters ($T > 300^\circ \text{C}$) indeed leads to the formation of these sub-surface structures [130], which coexist with silicide crystallites. The Mn-wires observed in the present STM study are characteristic for the room temperature deposition of Mn and present a distinctly different structure, which cannot be described by the high-temperature accessible sub-surface bonding sites [17]. It is, however, possible, albeit unlikely, that Mn is even at room temperature positioned in sub-surface sites and Si atoms are located on top of a sub-surface Mn-wire structure. The most recent publication by Wang et al. [131] establishes a library of stable wire structures with variable lengths and shows promising agreement with our experimental results for filled state images. However, one of the major features of the Mn wires is the contrast inversion in the empty state images, which has so far not been replicated in any of the theoretical models.

In the collaboration with P. Kratzer, one of the major features (as mentioned above) that we looked to replicate with the models was the contrast inversion in the empty state, positive sample

bias, images. Though the structure and bonding models of the Mn wires generated by our collaborators are simple and thermodynamically as energetically favorable models are an attractive match, they do not replicate this contrast inversion. The comparison between simulated STM images and experimental images is not necessarily straightforward; there can be additional effects not taken into account by simulations such as tip-induced band bending. However, the contrast inversion of the Mn wire at 0.7 V is a striking feature which should be reproducible with the correct model.

3.4.2. Temperature Evolution: Silicon Surface

The step edge is a source and a sink for defects and adatoms, and is in thermodynamic equilibrium with adatoms and defects on the terrace itself. The step edge therefore adopts an equilibrium shape, which is controlled by the interaction with the terrace until the diffusion of Si atoms along the step edge begins and the step edge thaws. The presence of Mn adatoms decisively influences the step edge formation energies and thus the roughness of the step edges, which was expressed in the number of dimers between kinks.

It can be seen in Figure 3.10, that the S_B step becomes more kinked with increasing temperature. Kinks on S_B steps are more readily formed due to the fact that the kinks run parallel to the dimer rows. Simply speaking, the kinks on the S_B step require breaking fewer bonds compared to kinks on the S_A step. The step edge formation energy of the S_B step is determined by the dimer interaction energy determined from the S_A step. Considering the S_A step edge, a kink must interrupt a dimer row of Si atoms. This results in a higher energy to form kinks on an S_A step edge hence the fewer number of kinks on this step edge. The step edge formation energy of S_A is lower due to the fact that the kinked portions of an S_A step are actually an S_B step edge, which has a lower formation energy than an S_A type step edge [21]. For samples S342 and S415

the step edge formation energy for the S_B step reaches a minimum. It is around this temperature that a step edge for pristine $\text{Si}(100)2\times 1$ is expected to thaw, and the number of kink sites will begin to fluctuate as dimer vacancies are generated and terminated at the step edge at an appreciable rate. The overall change in the step edge roughness is driven by an increase in the defect concentration on the surface, a change in the step edge formation energy and most likely also a modification of the freeze-out temperature of the step edge. However, all these parameters are connected, and driven by the interaction between Mn and the surface defects.

The behavior of the Si surface during the annealing process can be understood by the interplay of defect formation, their stabilization by Mn, the condensation of defects to DVLs and the interaction of the step edges with adatoms and defects. Annealing even at relatively low temperatures has a significant impact on the Si-surface, and the presence of Mn in sub-monolayer concentrations decisively impacts the defect formation and condensation into DVLs. The vacancy concentration surpasses by far that of a clean $\text{Si}(100)2\times 1$ surface especially at relatively low substrate temperatures, and DVL condensation begins far below the threshold temperature reported for a clean surface [132–134]. These observations are closely related to the effect of Ni, which is known to stabilize DVs and drive the condensation of DVLs [112,113,119]. We suggest that a similar mechanism is at work for Mn on $\text{Si}(100)2\times 1$ surfaces.

3.4.3. Temperature Evolution: Manganese Surface Structures

In the samples annealed at the lowest temperatures, S115 and S268, the formation of clusters located across terraces and decorated step edges are observed, respectively. The diffusion length of Mn adatoms therefore exceeds the terrace width, which is $15\text{ nm} \pm 5\text{ nm}$ for S268 and $13\text{ nm} \pm 5\text{ nm}$ for S115. The different location of the Mn-clusters on S115 and S268 can therefore be attributed to the increase in Mn adatom diffusion length with temperature.

A strong modulation of surface corrugation while the reconstruction is retained and is characteristic for the presence of sub-surface dopant atoms, which introduces additional states in the bandgap and shift the position of the Fermi energy within the gap [135–143]. For Si(100)2x1 the observation of dopants is usually hindered by the pinning of the Fermi level by surface states and as a result the dopant related state cannot be observed by changing the tip bias. The electronic signature of sub-surface dopants is therefore only seen on Si(100)2x1 if the modulation of the tip work function and local band bending are such that the dopant state can be filled and emptied during the tip-surface interaction as shown in Ref. [137–139].

The observation of dopants and their impact on the electronic structure is frequently reported for hydrogen passivated Si(100) which does not possess an extended surface state [135,142]. Mn has been studied extensively as a dopant in Ga(Mn)As; substitutional Mn can be imaged at the surface due to charge induced band bending which extends over large volumes relative to atomic length scales [140,141,144]. The images contain locally confined regions with strongly modified apparent heights whose characteristic shape reflects the interaction of Mn-dopants with the electronic system of the host matrix. The geometric structure of the surface is preserved in these regions [137,138]. Sub-surface Mn related structures on Si(100) have also been reported by Krause et al. [130], who described the formation of a specific local surface reconstruction, which coexists with large silicide crystallites in a high-temperature annealing experiment ($T = 650^{\circ}\text{C}$). However, the sub-surface states observed by Krause et al. are accompanied by a local modification of the surface reconstruction and are therefore most likely representative of the early stages of silicide formation rather than local doping.

Through a comparison with the literature on the detection and signatures of sub-surface dopants in STM images of semiconductors, we conclude that the regions with a larger apparent

height in S316 are related to the presence of electronically active sub-surface states caused by the presence of Mn dopant atoms [135–143]. The extension of the areas of larger apparent height is comparable to the observation of P and B acceptors on Si(100)2x1 described in the literature [135–139,143]. The sub-surface Mn therefore acts as an acceptor, which is of considerable interest for the formation of dilute magnetic semiconductors [145].

The true position of the Mn sub-surface atoms cannot be readily identified, but we can suggest two different scenarios that agree well with our observations. (1) The Mn sub-surface atoms are tied to the defects structures and positioned within the extended network of short DVLs. (2) Only those dopant atoms located in the vicinity of defects can be observed, due to a local perturbation of the surface state in the vicinity of defects and possibly local unpinning of the Fermi level, which enables imaging of the electronic signature of the electronically active Mn [120]. A rough estimate of the Mn-concentration in the three topmost Si-layers yields concentration on the order of 10^{18} cm^{-3} (0.1 ML deposited), which exceeds by far the solubility limit of Mn in bulk Si [146]. The supersaturation of the topmost layers of Si and Ge with Mn has been described previously, [147–150] but the mechanisms leading to the near-surface supersaturation are not well understood.

3.5. Summary

The fine structure of the Mn wires was investigated using STM. Two apparent bonding structures of the Mn wires was observed. The structures were identified by the offset between the Mn atom protrusion of the wire and the Si dimers. In one structure, the Mn atom protrusion aligns with the Si dimers and the other there is an offset of 0.25 nm, on average. Through collaboration with a theoretical modeling group that has done previous DFT work in Si and Mn, we presented some potential bonding models which describe two possible structures of the Mn

wires. Though the agreement between experiment and theory is reasonable at typical bias voltages (± 1.5 V), one feature of interest seen experimentally, contrast inversion of the Mn wires, was not replicated with the theoretical models.

In addition, we were able to identify the structural evolution of both the Si(100)2 \times 1 surface and Mn nanostructure within a temperature range not studied previously. Mn wires, which are produced during the initial room temperature deposition, are rather unstable and degrade rapidly to ultra-small clusters. One of the most important observations is the movement of Mn adatoms into sub-surface sites at about 316°C where Mn acts as an acceptor. This electronic interaction is expressed as a local modification of the apparent height in the STM images while the characteristic dimer-row reconstruction is conserved. In the high-temperature regime above about 400°C, the emergence of relatively large silicide crystallites dominates the surface. The concurrent modification of the defect population on the Si surface can be understood by the stabilization of surface defects by Mn adatoms and the interaction of defects with the step edges. This is expressed by the change in (1) step edge formation energy and (2) the number of dimers between kinks along the step edge with annealing temperature. A better understanding here of the interaction between the Si(100)2 \times 1 surface and Mn will better help us to not only understand the entrapment of Mn into sub-surface sites during Ge QD growth but also gives way to a route for a Si based DMS via delta doped layers.

Chapter 4. X-ray Photoelectron Spectroscopy of Mn Overlayers on Si(100)2x1 and a-Si

In the following section, XPS is used to help better understand the nature of the bonding that occurs between Mn overlayers and Si(100)2x1. This is accomplished by following, step-by-step, the deposition of Mn overlayer on Si through the analysis of the Si 2p and Mn 3p core levels. The modulation in bonding is expressed as a shift of the core level binding energies, which is then correlated with the interfacial reaction and thin film growth. The valence band reveals additional information on bonding albeit the interpretation of valence band spectra is complex. A portion of the following chapter is published in Applied Surface Science [18]. The experiments were performed at Brookhaven National Laboratory (BNL) with the assistance of Elio Vescovo. In this chapter, two sets of experiments were performed during different visits to BNL. Both sets of experiments investigated Mn overlayers on Si; one experiment used Si(100)2x1 as substrate and the other used an a-Si substrate.

4.1. Experimental Details

In the first set of experiments, a Si(100) wafer was cleaned by repeated annealing cycles reaching a temperature of about 1000°C, which was achieved by electron bombardment of the sample backside. The (2x1) reconstruction was confirmed by the presence of sharp reflexes in the low-energy electron diffraction (LEED) pattern, and the cleaning cycles were repeated until no further improvement was observable in the LEED pattern. Mn was subsequently deposited from an electron beam evaporation source (EFM3 Omicron Nanotechnology) and about 1 ML was deposited on the Si(100) sample. The coverage was determined by the XPS analysis of the relative peak areas of the Mn 3p and Si 2p core level using the excitation cross sections given by Yeh and Lindau [151]. The Fermi energy position or the position of the valence band maximum

is used as an energy reference for aligning the spectra to correct for small shifts in the photon energy.

In the second set of experiments, amorphous Si samples were prepared from originally crystalline Si(100) substrates. An amorphous Si surface was generated by Ar⁺ irradiation with a beam energy of 2 keV energy. The depth of the damage layer is about 5 nm and exceeds the information depth of the photoemission spectroscopy with energies of 160 eV to 40 eV. The amorphization is confirmed from the spectral shape of the valence band and the position and shape of the Si 2p core level. For the purposes of this experiment, generating an amorphous surface is sufficient. Samples were sputtered for short periods of time and the Si 2p peak was examined using XPS to determine if the Si 2p chemical shifts associated with the oxide are no longer detectable. The preparation chamber had a base pressure of 4.0×10^{-10} mbar and a partial pressure of 2.0×10^{-5} mbar was used during the sputtering with an energy of 2 keV and an emission current at the sputtering source of 4 – 8 μ A. Mn was deposited onto a single sample. The thickness of the Mn overlayers was calibrated using a quartz crystal rate monitor and the following total cumulative overlayer thickness were deposited: 1 ML, 2.5 ML, 5 ML, 10 ML, 20 ML, 40 ML and 120 ML.

The photoelectron spectroscopy for both series of experiments was performed at beamline U5UA at the National Synchrotron Light Source at Brookhaven National Laboratory [152]. U5UA is an undulator beamline, which is equipped with four gratings for optimum operation in the photon energy range between 15 and 200 eV. The light is linearly polarized in the horizontal plane, and the analyzer is fixed and its axis is at 45° with respect to the light incidence. The angle between sample surface normal and analyzer is modified by rotation of the sample, consequently

the angle between sample surface normal and the incoming light is modified at the same time. The geometry is shown in the insert in Figure 4.2.

For the fit of the core level peaks we use the program “fitt,” which employs the Marquard-Levenberg algorithm for the least square fit procedure [153,154]. The peaks are described by Doniach-Sunjic functions and Shirley background, and the quality of the fit is judged by the quality of the residual, the ability to describe sharp saddle points and the minima of the experimental curve [155,156]. A branching ratio of 0.6 and an energy separation of 0.5 eV was used for the Si 2p^{1/2} and Si 2p^{3/2} components. The smallest number of peaks, which gives a good fit of the experimental data, is used for analysis of the data.

4.2. Mn overlayers on Si(100)2x1

Figure 4.1(a) shows the Si 2p core level (solid lines) before and after the deposition of Mn for a photon energy of 160 eV and includes the results of the peak fit procedure (dotted lines). An excellent fit can be obtained for the Si(100) surface prior to Mn deposition by using four peaks. The results for both photon energies (140 and 160 eV) yield the same binding energies within a margin of ± 0.1 eV. A LEED diffraction pattern, given as the inset in Figure 4.1(a), confirms the presence of the (2x1) reconstruction and sharp well-defined diffraction spots are observed prior to the deposition of Mn. After the deposition of Mn, five peaks are required to achieve an equally excellent description of the Si 2p peak.

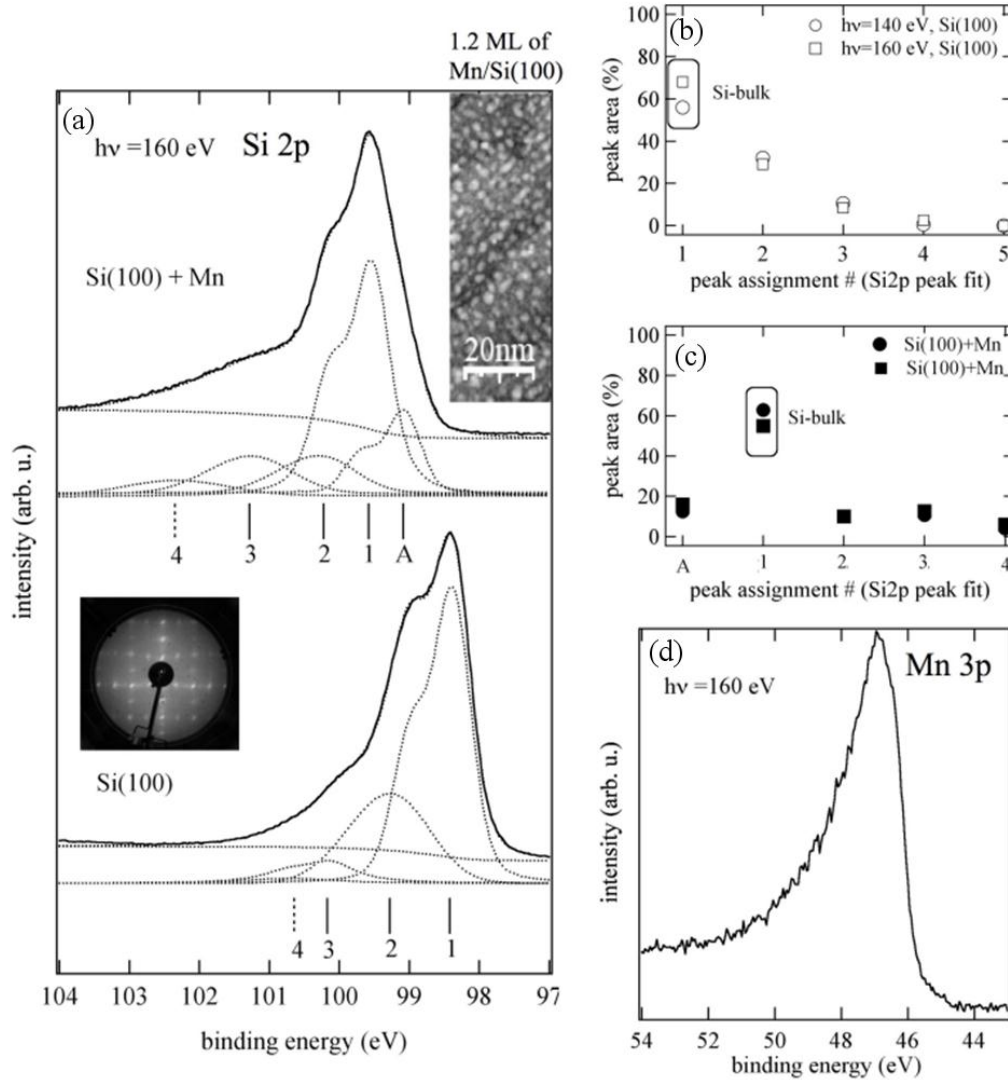


Figure 4.1. (a) Si 2p core level for the Si(100)2x1 surface, and after the Si2p after the deposition of Mn are shown. The results of the fit procedure are included and the labels of the peaks are indicated in the figure. The LEED pattern of the Si-surface is shown as an inset and confirms the presence of the (2x1) reconstruction. A second inset shows the STM image measured after the deposition of 1.2 ML of Mn on Si, which was described in detail in a recent publication. (b,c) The area of all fit-curves is shown before and after the deposition of Mn. (d) The respective Mn3p peak is shown at the bottom.

In Figure 4.1(b,c) the relative peak intensities of the Si 2p core level contributions are summarized, and the peak numbers begin with the most intense peak, which is positioned at 98.4 eV for Si(100) and at 99.1 eV after the deposition of Mn [157–159]. The contribution positioned at the lowest binding energy is the most intense peak for Si(100). After the deposition of Mn, an additional peak with a contribution of nearly 20% to the total peak area is observed on the low

binding energy side of the Si 2p peak, labeled A in the figure. The width of the Fermi edge/valence band edge is conserved for all measurements, and the changes in the Si 2p core level are therefore not caused by a modification of the spectral resolution. The Mn 3p core level, as shown in Figure 4.1(d), is positioned at 46.9 eV and cannot be described reliably by a fit procedure due to the presence of multiple overlapping peaks from the spin-orbit and multiplet splitting typical for 3d transition metals [160–163].

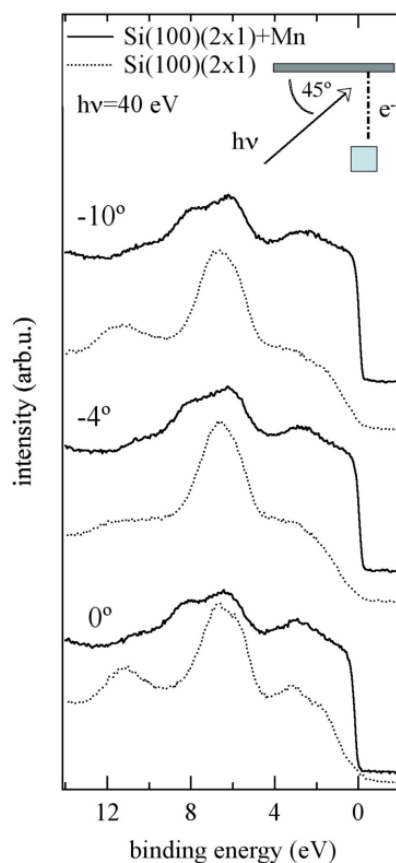


Figure 4.2. The VB spectra for the Si(100)(2x1) surface and the surface after the deposition of Mn are shown as a function of the angle between surface normal and analyzer. The inset illustrates the geometry for an angle of 0°.

As shown in Figure 4.1(a), the most intense peak (labeled #1) in the Si(100) spectrum is positioned at 98.4 eV, and the peaks labeled #2, and #3 are positioned at 99.1 eV, and 100.1 eV with a shift of 0.7 eV, and 1.7 eV with respect to the most intense peak (peak #4 at the highest binding energy of 100.54 eV has a very small contribution and its position is therefore not

reliable). These peak positions agree with the presence of sub-oxides as described by Himpsel *et al.* [159] and the most intense peak can be ascribed to the Si-bulk.

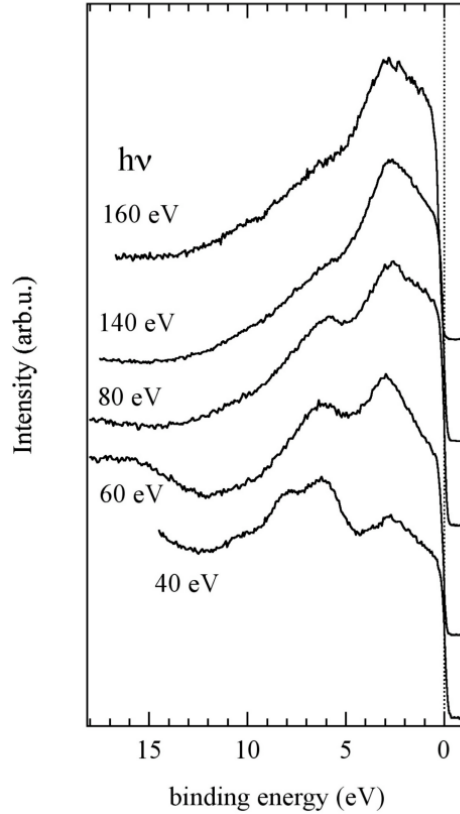


Figure 4.3. The VB spectra after the deposition of Mn as a function of the photon energy. An intense Fermi edge is present and confirms the metallic nature of the overlayer.

After the deposition of Mn, the Si-core level peak is shifted to higher binding energies. The most intense peak, which is representative of the Si-bulk atoms is shifted by +0.7–99.1 eV ($h\nu = 160$ eV), and by 0.4 eV for $h\nu = 140$ eV. The Gaussian and Lorentzian full-width at half maximum (FWHM) are 0.5 ± 0.05 and 0.04 ± 0.015 eV, respectively, and are identical for peak #1 before and after the Mn deposition. This supports the assumption that this component can indeed be attributed to the Si-bulk peak. All other peaks exhibit a larger FWHM, which can also be seen by inspection of the fit-curves in Figure 4.1. The high binding energy peaks related to the sub-oxides are shifted by the same amount for the respective photon energies. Peak #2 is slightly

shifted towards the Si-bulk peak, and the magnitude of the shift is right at the limit of the precision of the fit.

In Figure 4.2 a set of valence band spectra is shown for the original Si(100)2x1 surface and the Si(100) + Mn (solid and dotted lines, respectively). The geometry of the setup is included as an inset in Figure 4.2. The angle between the analyzer and the sample normal is varied in 28 increments and a representative selection of VB spectra is shown. [157,164] The direction of rotation corresponds to a measurement in the surface Brillouin zone along the direction from $\bar{\Gamma}$ to \bar{X} . The spectra of the Si(100) surface does not show a surface state related peak below 1 eV, which can be attributed to the presence of sub-oxides and the use of a relatively high photon energy, where the intensity of the surface state is relatively low. [165,166] The peaks positioned at 2.1, 3.2, and 11.2 eV are assigned to bulk states of the Si and they show no dispersion with the variation of the angle, albeit their relative intensities are modified. The double peak between 6.0 and 7.0 eV is a superposition of excitation from Si-bulk states, and the presence of surface oxides. This assignment agrees with results from the core level analysis. A further increase in the surface oxygen concentration leads to a VB spectrum dominated by the peak at 6.9 eV.

After the deposition of Mn, the spectra changed dramatically and an intense Fermi edge is observed. A low intensity peak is present at 3.2 eV, and two peaks at 6.9 and 8.2 eV are identified. The Si related contribution at 11.2 eV cannot be detected anymore; the spectrum in the region adjacent to the Fermi edge is dominated by the Mn-containing overlayer [162,167,168]. For further analysis of the overlayer we used the variation of the photon energy, which gives access to deeper lying states, and allows a comparison with α -Mn (Figure 4.3). This phase is obtained by the evaporation and condensation of Mn at room temperature, and the energy dependence of the valence band spectra has been discussed in detail in Irizawa *et*

al. [162]. The intense Fermi edge and the peak at 2.7 eV stem from the Mn d-band and overwhelm any residual contribution of the Si-p bands in this energy range. The peak at 17 eV which is only visible in the 60 eV spectra is related to the $M_{2,3}VV$ Auger band.

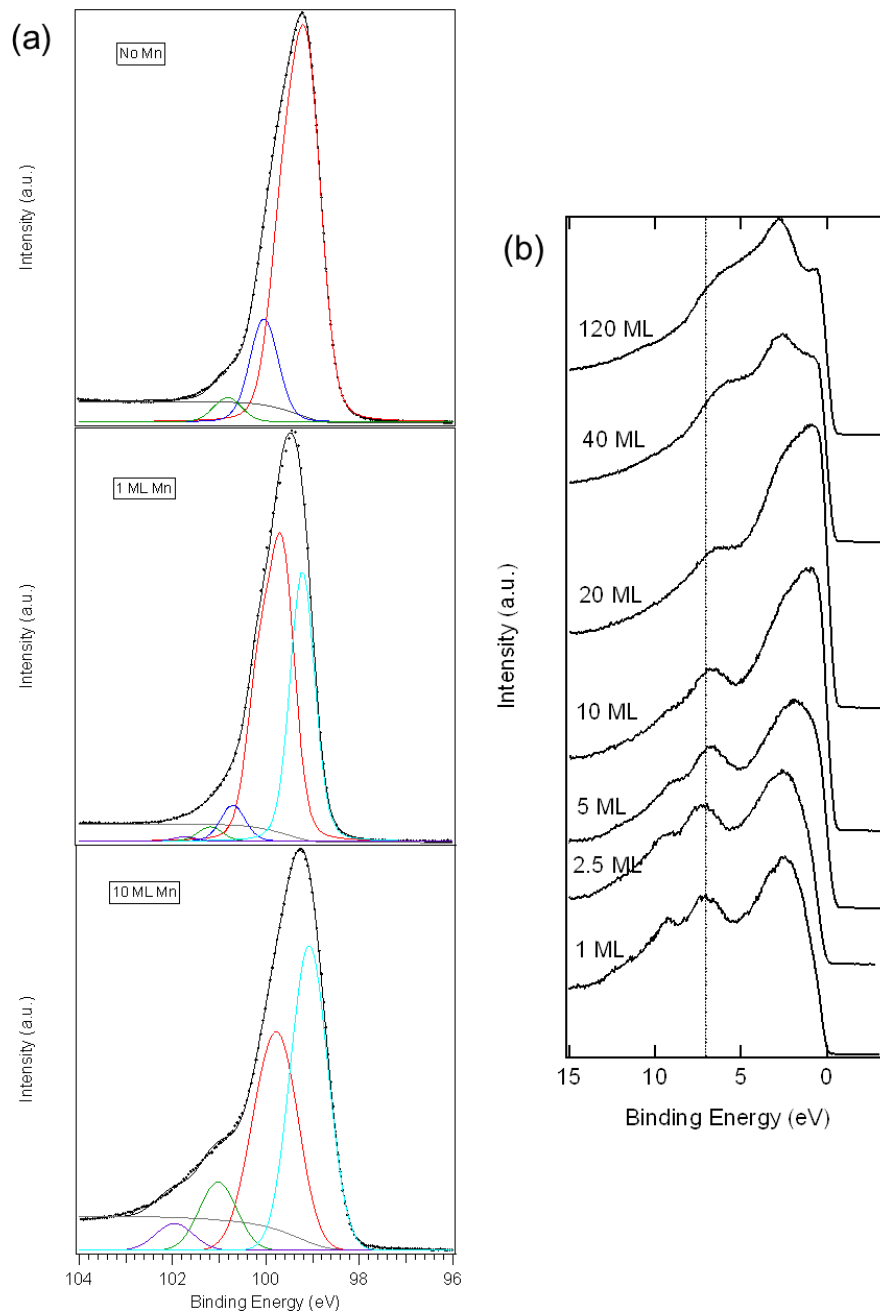


Figure 4.4. (a) Si 2p spectra and the resulting fitted peaks. The Si 2p peak is shown for 3 different states of the sample: (1) Si-substrate after Ar sputtering, (2) after 1 ML Mn deposition, and (3) after 10 ML Mn deposition. (b) The valence band spectra as a function of Mn coverage at an energy of 160 eV.

4.3. Mn overlayers on a-Si

In Figure 4.4(a) the Si 2p core level is shown with the peaks resulting from the fitting procedure. The Si 2p core level was measured before Mn deposition, after 1 ML Mn deposition and after 10 ML Mn deposition. The Si 2p core level before Mn deposition is described by three peaks. All peaks contain the Si 2p 3/2 and 1/2 spin-orbit split components as described in the previous section. The lower intensity higher energy peaks are within ± 0.1 eV of the Si^{1+} and Si^{2+} peaks as described by Himpsel [159]. The addition of Mn of 1 ML and 10 ML depositions requires an additional peak to describe the Si 2p core level. The new highest binding energy peak at +2.1 of the Si 2p 3/2-1/2 is close agreement with the Si^{3+} state. In addition, after Mn deposition an additional peak whose intensity scales with the amount of Mn develops on the low binding energy (LBE) side of the the Si 2p 3/2-1/2 peak. As seen in Table 4-A, the LBE peak varies in relative position from the Si 2p 3/2-1/2 peak from -0.3 eV to -0.6 eV. As seen in the Mn overlayers on Si(100)2x1 experiments, the Si 2p 3/2-1/2 peak shifts to a higher binding energy after Mn deposition, a change of +0.5 eV in the a-Si case.

The effect of Mn deposition on the VB at an energy of 160 eV is shown in Figure 4.4(b). Here all Mn deposition coverages are shown from 1 ML to 120 ML. With increasing Mn coverage, the emergence of a sharp Fermi edge indicates the presence of metallic layers on the surface. Within the valence band, peaks at 2.5 eV, 6.9 eV and 9.2 eV are observed. The peak at 6.9 eV with increasing Mn deposition decreases in contribution with increasing Mn coverage, likely diminished by the increasing contribution of the Mn 3d band to the VB.

Deposition	Peak 1 Si2p 3/2-1/2 (eV)	Peak 2 (eV)	Peak 3 (eV)	Peak 4 (eV)	Peak 5 (eV)	Peak LBE (eV)
No Mn	99.1	+0.9	+1.7	-	-	-
1 ML	99.6	+1.1	+1.6	+2.1	-	-0.4
2.5 ML	99.6	+0.9	+1.7	+2.4	-	-0.3
5 ML	99.6	+0.9	+1.3	+2.1	-	-0.6
10 ML	99.6	+0.8	+1.4	+2.3	-	-0.6
20 ML	99.6	+1.1	+1.6	+2.5	+3.5	-0.5
40 ML	99.6	+1.1	+1.6	+2.5	+3.5	-0.5
120 ML	99.6	+1.1	+1.6	+2.5	+3.5	-0.5

Table 4-A List of peak positions resulting from the fit procedure as a function of Mn deposition coverage. Peaks are denoted by their relative position to the Si 2p 3/2-1/2 peak.

The full range of Mn depositions and their effect on the Si 2p core level is shown in Figure 4.5(a). At the highest two Mn depositions, 40 ML and 120 ML, a fourth high binding energy peak emerges and in the 120 ML case dominates in intensity all other peaks. There is a small Si 2p 3/2-1/2 peak in the 120 ML spectra, but the intensity above the background is so minute that its position and intensity are unreliable. In the figure, the positions of the Si 2p 3/2-1/2 peak and the Si⁴⁺ peak are marked by a vertical dotted line across all spectra.

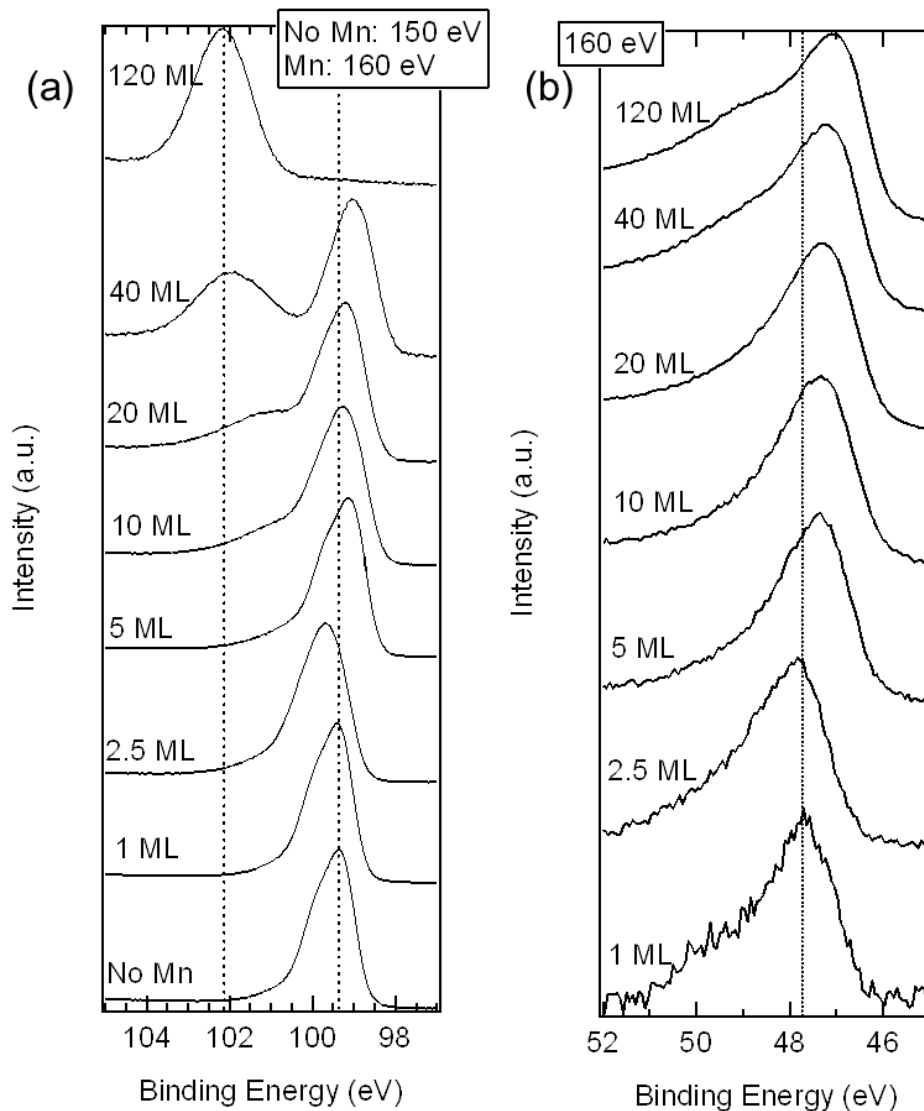


Figure 4.5. (a) Si 2p core level as a function of Mn deposition. Spectra obtained at 150 eV for the no Mn core level and 160 eV for all others. (b) Mn 3p level as a function of Mn deposition. All spectra obtained at 160 eV.

The effect of the increasing Mn deposition on the Mn 3p level is shown in Figure 4.5(b). After 1 ML Mn deposition, the peak is positioned around 47.7 eV. With increasing Mn deposition, the main peak can be seen to shift to lower binding energies to a minimum of 47.1 eV at 120 ML of Mn. In addition, a shoulder on the high binding energy side of the tail of the Mn 3p peak starts to appear in the 20 ML sample and become more prominent with increasing Mn coverage. As mentioned previously the multiplet nature of the Mn 3p level makes it difficult to decompose the chemical shifts of the 3p level. In Figure 4.6, the VB is explored further as a function of energy

for two Mn coverages, 1 ML and 10 ML for Figure 4.6(a) and (b), respectively. Here the variation of the 6.9 eV peak is shown as a function of energy, with increasing energy the relative contribution of this peak decreases with increasing energy in both Figure 4.6(a) and (b). When comparing the 1 ML and 10 ML results, the peak at 12.0 eV in the 1 ML case is either a standalone peak or a slight shoulder depending on the energy. In the 10 ML case, this peak is not present. The source for this peak is a Si contribution to the VB, and the contribution of this peak can be expected to decrease with increasing Mn coverage.

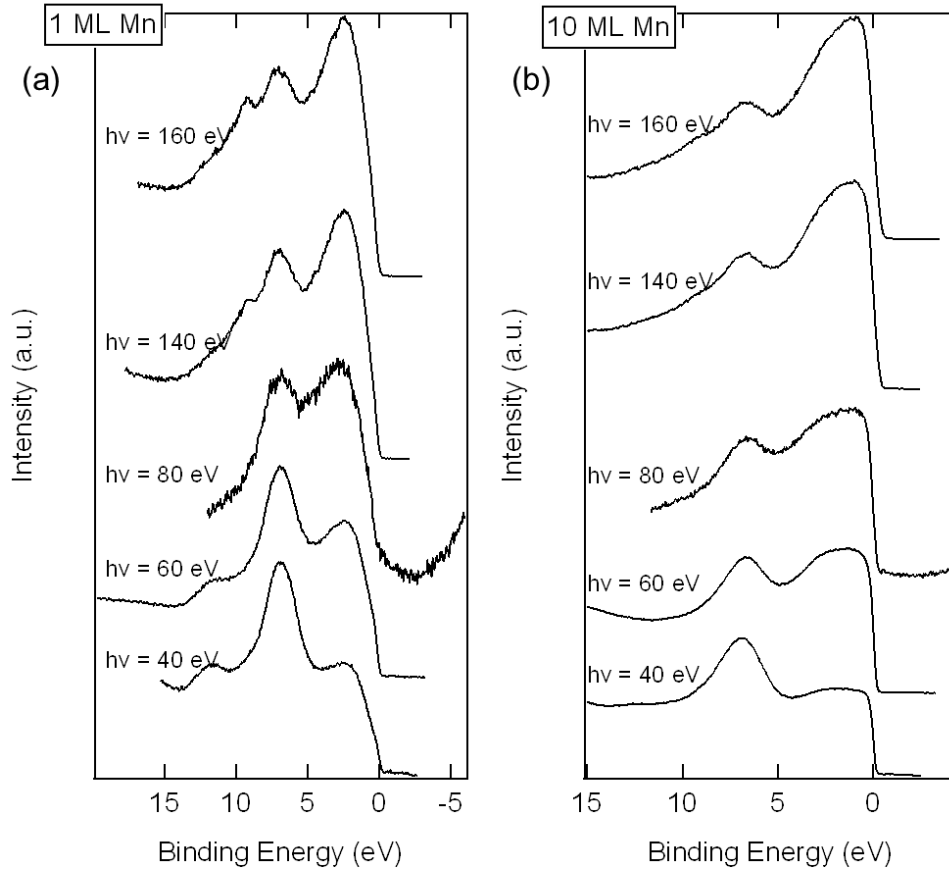


Figure 4.6. VB spectra depicting the energy dependence of the VB for two Mn depositions: (a) 1 ML and (b) 10 ML.

4.4. Discussion

The results given from the Si(100)2x1 Mn overlayer experiments of the Si 2p, Mn 3p, and VB reveals the interaction between Mn and Si. Starting with the Mn 3p peak, the position of the main peak is commensurate with either Mn or Mn-silicides or a mixture of both. The formation of Mn oxides, which introduces a large chemical shift denoted by the appearance of a shoulder on the high binding energy side of the Mn 3p peak, was only observed in samples stored for more than 12 h in vacuum.

The excitation cross section is larger for Si^{n+} oxidation states than for Si^0 , and the relative areas therefore overestimate the sub-oxide contributions. We cannot detect a surface core level state, which would be positioned on either side of the Si 2p peak, although we might be unable to separate the most intense surface core level peak from the first sub-oxide peak [165,166]. The shift for peak #2 after Mn deposition, which is also greatly reduced in intensity, might indicate a reaction with the overlying Mn-layer and incorporation of oxygen within the Mn silicide-matrix. The appearance of the silicide peak (labeled A) is coupled with a decrease in the intensity of the peak at +0.7 eV (labeled #2). A reaction of Mn with the surface might occur preferentially on the Si^{+1} sub-oxide sites and therefore account for the decrease in this peak's intensity, or a redistribution to the higher oxidation states occurs which peaks #3 and #4 do indeed exhibit overall a slight increase in intensity. The Si-sub-oxides [169] are highly reactive and often react by oxidation of the metallic overlayer, leading to the reduction of Si [170–173]. A similar reaction can be expected with Mn, which is easily oxidized, and has several stable oxidation states. Si_2^{+1}O is the most abundant sub-oxide on our surface, and offers a highly active reaction center for the Mn adatoms. The dramatic decrease in the intensity of the Si_2O peak (peak #2) indicates at first sight a preferential interaction with this oxidation state. However, the relative

contributions from the other oxidation states are only around 5% of the total peak area and as such are prone to a relatively large error in the fit procedure. Whether their contributions change by a relevant percentage can therefore not be stated with certainty. The addition of a Si 2p contribution on the low binding energy side is consistent with the formation of a silicide with the composition MnSi or a manganese rich phase, Mn_5Si_3 [167]. The binding energy shift with respect to bulk Si is indicative of a charge transfer from Si to Mn. The ratio of Mn to Si bound in silicide is 65:35, and has been determined from the peak areas for the silicide peak (label A) and the Mn 3p core level after correction for the respective excitation cross section. This leaves us with two alternative interpretations: firstly, the reaction of Mn with the Si surface leads to the formation of a Mn-rich silicide, or secondly, MnSi is formed at the immediate Mn–Si interface and the remaining Mn is present in its elemental state. The position of silicide related Si 2p core level agrees with both types of silicides. The angular dependence of the VB reveals that the Mn containing surface layer is polycrystalline due to the lack of change in the VB for the $\text{Si}(100)2\times 1 + \text{Mn}$ surface.

The VB spectra as a function of photon energy overall agree quite well with those reported for $\alpha\text{-Mn}$ as a function of photon energy [162]. The peak around 6.5 eV; however, has two overlapping contributions: one from Si bulk states and a second one which can be assigned to residual surface oxides. The peak at 6.5 eV undergoes intensity reduction considerably with higher photon energy and therefore a larger information depth and decreasing cross section.

Only the lack of a pronounced minimum at about 2 eV might indicate the presence of another material, and could be related to the contribution from Si-p valence band states, Mn–Si, or Mn–Si–O hybrid bands at the interface. However, most recent calculations of Mn-silicide density of states indicate that the hybridization leads to additional states at energies between 1 and 2

eV [167], which has been shown experimentally for Mn_5Si_3 single crystals. We therefore suggest as a tentative model that a silicide is formed at the boundary between Si and the Mn-overlayer, while the overlayer itself is dominated by metallic Mn. The STM images from our previous study (see Chapter 3) show that clusters rather than continuous layers cover the Si(100) surface after Mn deposition, which is in contrast to the layer-growth described for silicides on Si(111) [127]. These clusters would then consist of α -Mn and the contact area to the Si surface is a silicide of as yet unknown composition.

The Mn overlayers on a-Si results have presented us with several challenges in their interpretation and are still under discussion. The main points of contention is the origin of the large peak positioned at the high binding side of the Si $2p_{3/2,1/2}$ peak at high Mn coverages. By estimating the information depth with the Lambert-Beer Law, 95% of the electrons will be scattered when the film has a thickness around 9 nm to 15 nm for kinetic energies around 50 eV for the Si 2p core level. With the thickest Mn film around 15 nm, we are within the limit of detection for the Si peak. The fact that the Si 2p peak still has an appreciable intensity with our thickest film indicates that there is substantial intermixing between Si and Mn. However, this large peak is not identifiable as another species, including Ar used for initial surface cleaning. The intensity of this peak scales with the amount of Mn deposited on the surface, and is likely related to a specific Mn-Si bonding state. The contributions from oxides do not increase during the deposition, which is confirmed by the lack of an increase in the oxide peak located in the valence band spectra. The peak assignment remains uncertain although it is very likely related to a strongly reacted Mn-Si phase, which forms at the Si-Mn interface. The oxidation state of the Si in this interfacial phase is close to Si^{4+} .

4.5. Summary

In summary, the reaction of Mn with the Si(100) surface leads at room temperature to the formation of a thin silicide interface, presumably with MnSi stoichiometry. Mn, either as Mn-metal or as a Mn-rich silicide phase, dominates the grown overlayer. In contrast to Mn on the Si(111) (7x7) surface, the overlayer forms clusters rather than well-defined single silicide layers when considering our Mn-Si(100)2x1 results. The presence of surface sub-oxides, which were observed during the XPS study, can conceivably function as surface traps for Mn and might influence the interfacial bonding and extent of Fermi level pinning at the interface. The reaction at the interface, which forms an as-of-yet identified silicide characterized by a mystery peak at the Si^{+4} chemical shift energy of Si 2p. This reaction progresses further in the amorphous substrate case than the crystalline Si case. This peak was also observed in the Mn-Si(100)2x1 experiment but was much weaker.

The results from this chapter, describe the reaction and bonding between Mn overlayers and Si(100). Chapter 3 discusses specific nanostructures, Mn wires, that form on Si(100)2x1. Due to the presence of a partial oxide layer, it is unlikely that Mn wires formed during the experiments performed at BNL. However, without real space imaging the exact structure during the BNL experiments is unknown, but presumed to be clusters.

Chapter 5. Mn Islands on Ge Quantum Dots

Controlled annealing of Mn islands deposited at room temperature on Ge QDs is a surface driven method developed to avoid the formation of secondary phases and achieve incorporation of Mn into Ge QDs. Inspired by our previous work with Mn on Si(100), this chapter sets out to characterize the structure of low-coverage (sub-monolayer) Mn formations on the Ge(105) facets of Ge hut/pyramid QDs and the Ge wetting layer.

5.1. Experimental Details

Si(100)2x1 samples were prepared as described in Section 2.4. Ge quantum dots were grown on Si substrates at a temperature of approximately 450°C at a Ge rate of 0.005 Å/s using a Veeco effusion cell. Mn was evaporated from a Mo-crucible using a home built electron beam evaporation source at a rate of 0.025 Å/s. Mn-coverage (Θ_{Mn}) was in the sub-monolayer regime, 0.05 – 0.2 ML.

Imaging conditions of -2.0 V and +2.0 V gap voltages were used with a 0.03 nA current set point and imaging conditions can also be found in the figure captions. A number of STM images were recorded at elevated temperatures with the use of an Omicron Nanotechnology STM stage power supply to heat the samples by direct current heating. In addition the power supply applies a compensation voltage to offset the voltage drop across the length of the rectangular samples from the heating power supply to obtain the correct imaging gap voltage.

Scanning tunneling spectroscopy (STS) was performed as single point spectroscopy where while an image is acquired, through mouse selection, different points are selected to perform spectroscopy at structures of interest. In the voltage sweep of the spectroscopy, the starting voltage is selected to be the same polarity as the imaging bias or ideally exact same voltage. This helps in reducing artifacts in the beginning of the spectroscopy measurement. As discussed in

Section 2.2, ideally the tip is purely metal and can be idealized to have an abundance of electronic states to tunnel in and out of. In practice, this is not always the case. Tip contamination from oxides or other species can influence the states available at the tip and the resulting spectroscopy can be a convolution of the tip and sample

Image analysis was performed using ImageJ [110], WSxM [111] and Gwyddion [174] software packages. Mn structures on Ge QDs were characterized by their location on the QD, largest in-plane length, height, area and volume. To differentiate the location of the Mn structures on the QDs, the QD was divided into two regions: the facet region and the region extending approximately 1 nm beyond the edge where two facets meet called the edge region. The distinction between the edge and facet regions is introduced because the edge region is typically a highly reactive site, which can serve as a primary nucleation and attachment site for surface structures. The largest in-plane length and height, which is an apparent height in the STM, were measured using line scans across the Mn structure.

The area of the Mn structures were measured by first isolating the Mn structures from the background using n^{th} -order polynomial flattening processes (n was adjusted as needed to achieve optimum results where the Mn structures were visually separated from the surroundings with minimal distortion, typically an 8^{th} -order polynomial). The flattening process or background subtraction eliminated the geometric distortion due to the Mn island location on an inclined surface plane. Following the background subtraction, a binary mask, which is defined by height thresholding, generated an image containing only the Mn structures, and the total area occupied by this binary mask was measured. Similarly, the volume of the Mn structures was found by generating a mask including only the Mn structures and using a built-in function of Gwyddion to report the volume of the generated mask.

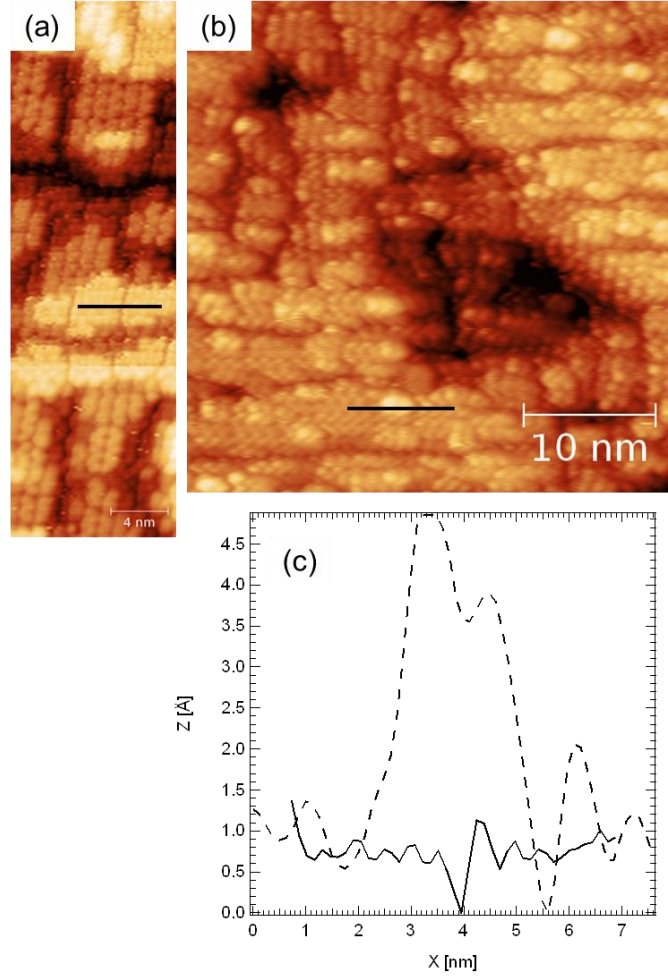


Figure 5.1. STM images of the Ge(100) wetting layer (a) prior to Mn deposition and (b) after Mn deposition. (c) Line scans from (a) and (b) were taken from representative areas on each image and are indicated by the black bar within each image. Both line scans are shown on the same scale for comparison. In (c) the dotted line represents the line scan from (b) and the solid line from (a). Both images were obtained with a sample bias of -2.0 V.

5.2. GeQDs and Mn Islands: As Deposited

The following results are presented by first establishing the starting surfaces for the room temperature Mn deposition experiments and then proceeds to the results and discussion for the behavior of Mn and the Ge(100) wetting layer followed by Mn and Ge(105) facets of GeQDs. The Ge surfaces prior to the room temperature deposition of Mn are shown in Figure 5.1(a) for the Ge(100) wetting layer and Figure 5.2(a) for the Ge{105} QD facets. The room temperature deposition of Mn yields small, typically elongated, flat islands on both the wetting layer and the

Ge{105} QD facets. However, the Mn islands located on the wetting layer are more difficult to properly identify and characterize due to the inherent roughness of that surface. Typical STM images of the islands on the Ge wetting layer and Ge QDs are shown in Figure 5.1(b) and Figure 5.2(c,d), respectively.

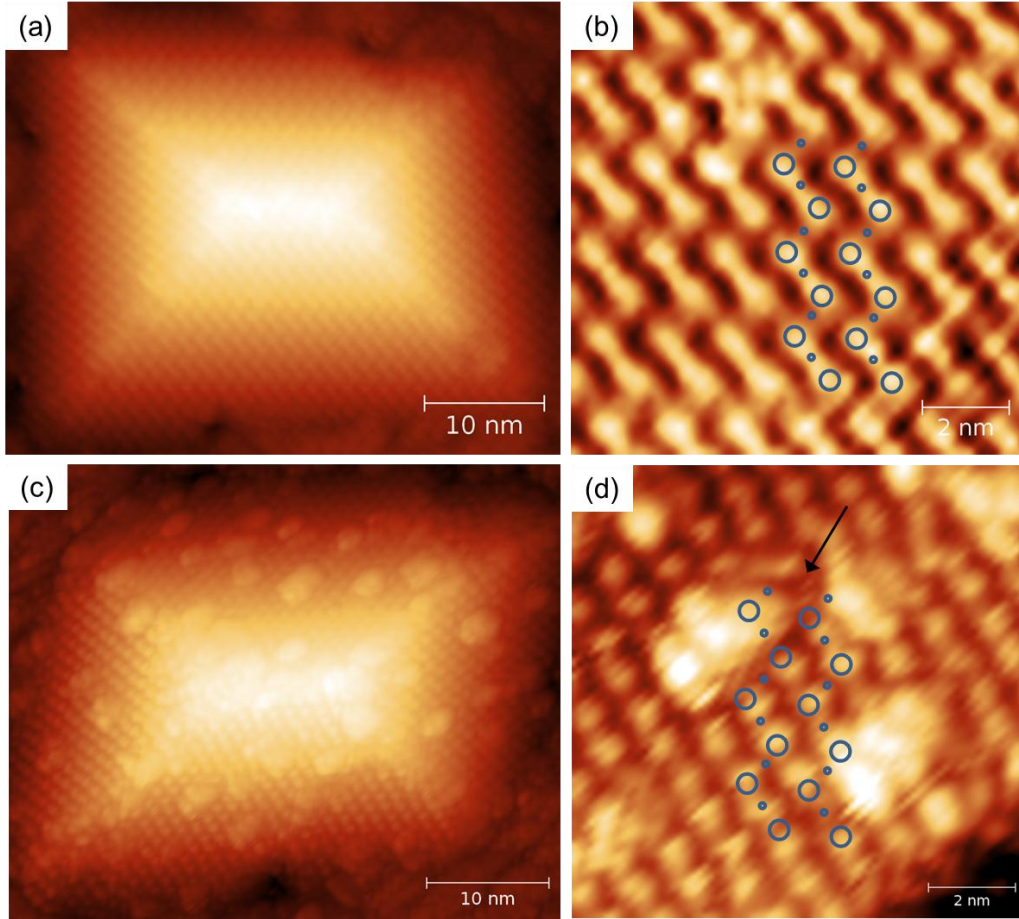


Figure 5.2. STM images of a single Ge QD (a) prior to Mn deposition and (b) a smaller scale image of a QD facet containing an overlay of the Ge(105) 2x1 rebonded step reconstruction. A second STM image of a Ge QD (c) after Mn deposition containing Mn islands decorating the facets and facet edges of the QD and (d) a smaller scale image of a QD facet with an overlay of the Ge(105) 2x1 rebonded step reconstruction. All images were obtained with a sample bias of -2.0 V.

The structure of the Ge wetting layer after QD growth is shown in Fig. 1(a). The Ge wetting layer consists of regions of reconstructed, (2x1) and c(4x2), atoms surrounded by DVLs dividing the surface into tile-like regions of the two different orientations of reconstructed atoms [175,176]. After Mn deposition, one of the most notable difference in the structure is the

apparent roughening of the wetting layer surface as shown in Figure 5.1(b). Linescans in Figure 5.1(c) depict the typical structure across Mn adatoms on the Ge wetting layer compared to the wetting layer without Mn. The Mn islands have an apparent height over the Ge atoms of 0.25 – 0.35 nm. Due to the roughening of the wetting layer, it is not possible to unequivocally distinguish Mn islands from the roughened Ge(100) wetting layer.

Compared to the wetting layer, islands on Ge QD facets were more readily apparent. The islands had two general shapes: circular and elongated islands. Of the elongated islands, approximately two thirds of the islands were elongated in the $[\bar{5}11]$ direction on the Ge{105} facets. In addition, islands were evaluated based on their position on the Ge QDs. Two regions on the QD were identified: one consisting of the face of Ge{105} facets and a second region consisting of the area surrounding the edges where the {105} facets meet. The density of islands on the facet faces and edges are 0.014 ± 0.001 islands/nm² and 0.022 ± 0.0011 islands/nm², respectively. The number of islands located in the region surrounding the edges and the facet faces were normalized to the respective available areas of each region. Seventeen QDs and 179 Mn islands were analyzed in this process.

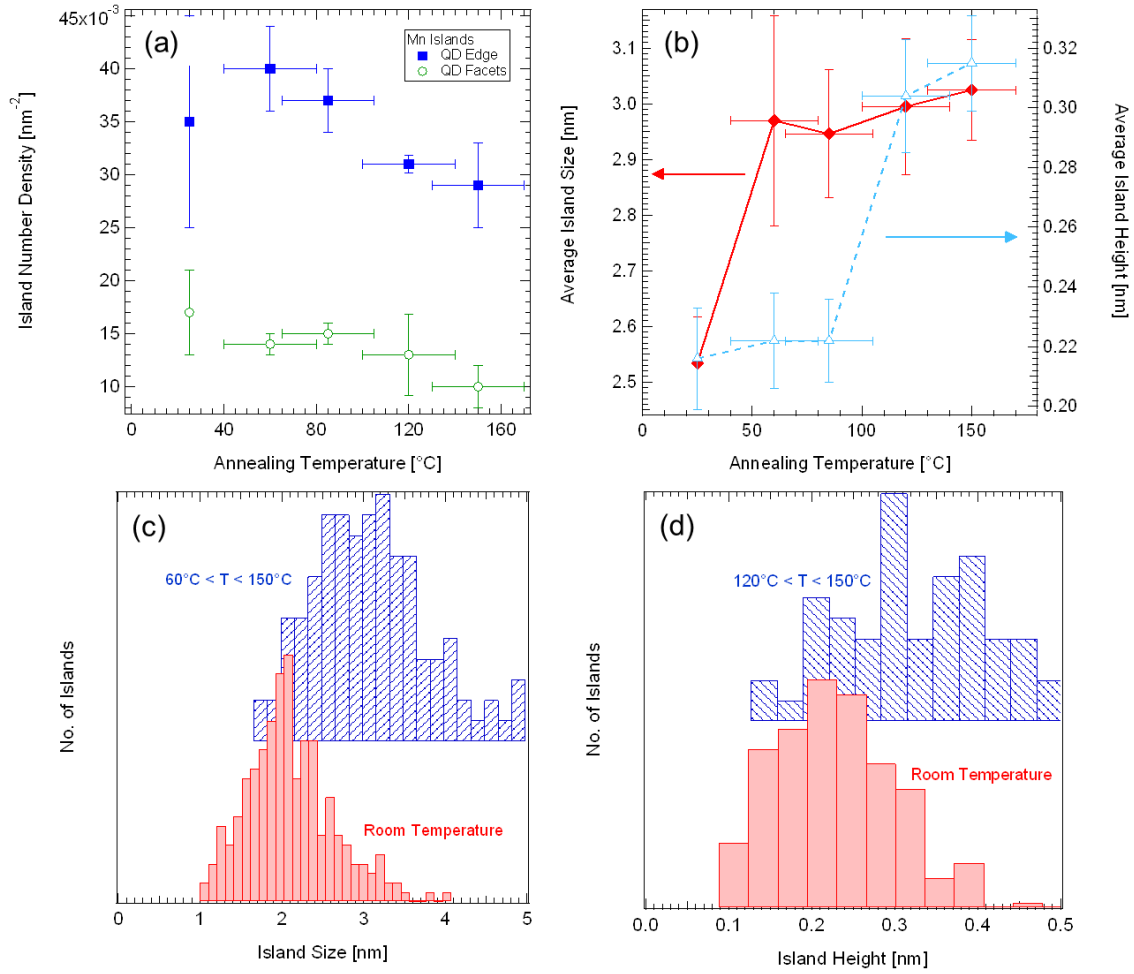


Figure 5.3. (a) The number density of Mn islands on Ge QDs facets and facet edges is plotted and how it varies with increasing annealing temperature from room temperature to 150°C . (b) Mn island average size (left axis) and average height (right axis) are shown as a function of annealing temperature from room temperature to 150°C . (c) Distribution of Mn island size at room temperature compared to the island size distribution between 60°C and 150°C . (d) Distribution of Mn island height at temperature compared to the island height distribution between 120°C and 150°C .

5.3. GeQDs and Mn Islands: Temperature Evolution

The evolution of the Mn islands with increasing annealing temperature from room temperature up to 400°C were characterized for island number density, apparent height, long-axis length and volume. First, we will cover the results from annealing the Mn islands up to a temperature of 150°C . The effect of annealing a sample up to a temperature of 150°C on the density of islands located on the facet edges and the facet face is shown in Figure 5.3(a). With

increasing annealing temperature, the number of islands on both the facet edge and facet face decreases though the trend is more pronounced for islands located on the facet edge. Figure 5.3(b) contains the island size and island height (apparent height) as a function of temperature. At 60°C the island largest dimension length shows an abrupt increase and at 80°C the island height shows an abrupt increase. In both cases, the length and height as a function of annealing temperature leveled off after their respective abrupt increases.

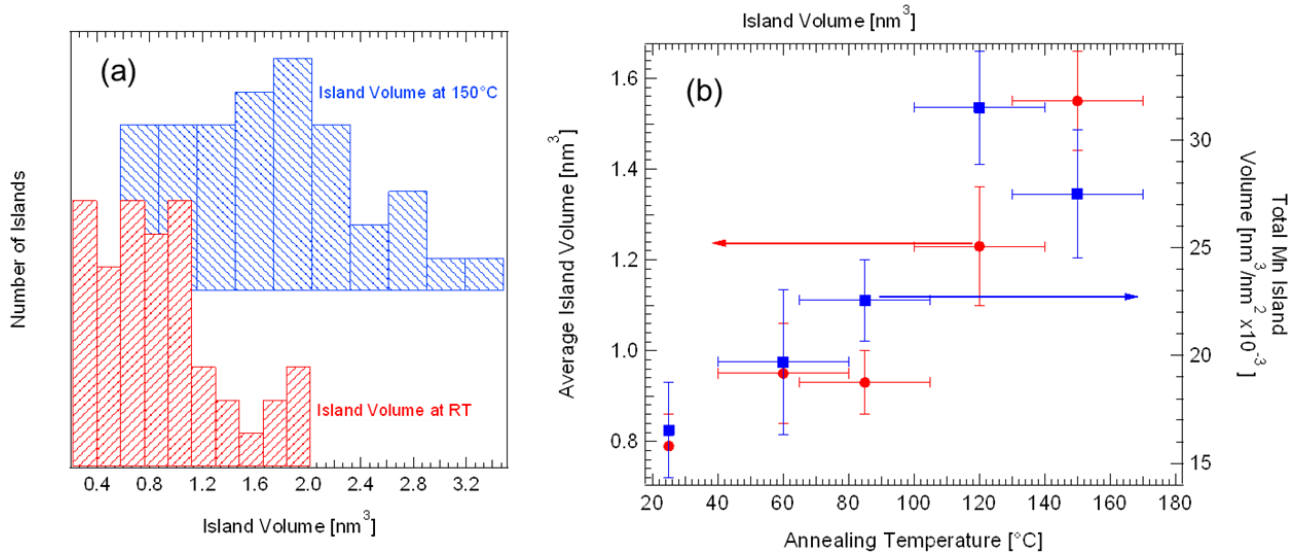


Figure 5.4. The volume of the Mn islands represented as (a) distributions at room temperature and 150°C, and (b) as a function of annealing temperature. In (b) the left axis and gives the average island volume and the right axis gives the total Mn island volume normalized to the image area.

The distribution of long-axis length of the islands at two different temperatures is shown in Figure 5.3(c). Shown are the room-temperature distribution and a group of elevated sample temperatures from 60°C to 150°C. As can be seen in Figure 5.3(b) this group of sample temperatures have similar island long-axis lengths. At room temperature the peak of the distribution is around 2.1 nm and shifts to approximately 3.0 nm in the 60°C to 150°C range. In Figure 5.3(d) the distributions of island heights at room temperature and a group of sample temperatures from 120°C to 150°C are shown. The Mn islands at room temperature has a peak in

the distribution at approximately 0.2 nm and the 120°C to 150°C sample temperature range distribution does not necessarily have a clear peak due to the small sample size. However, it is clear that the distribution widens and possibly becomes more symmetric. As seen in Figure 5.4, the average and total volume and volume distribution of Mn islands is plotted versus annealing temperature. In Figure 5.4(a), volume distributions are shown for Mn islands after the room temperature deposition and during in-situ annealing at 150°C. The distribution at elevated temperatures is shifted to higher values and is broadened when compared to the room temperature island volume distribution. Figure 5.4(b) shows the effect of sample annealing temperature on the average per island volume and total volume of Mn islands per unit area. As a function of temperature, both values are shown to increase from room temperature up to 150°C. The average island volume increases from 0.79 to 1.55 nm³ and the total volume of islands per unit area increases from 0.017 to 0.028 nm.

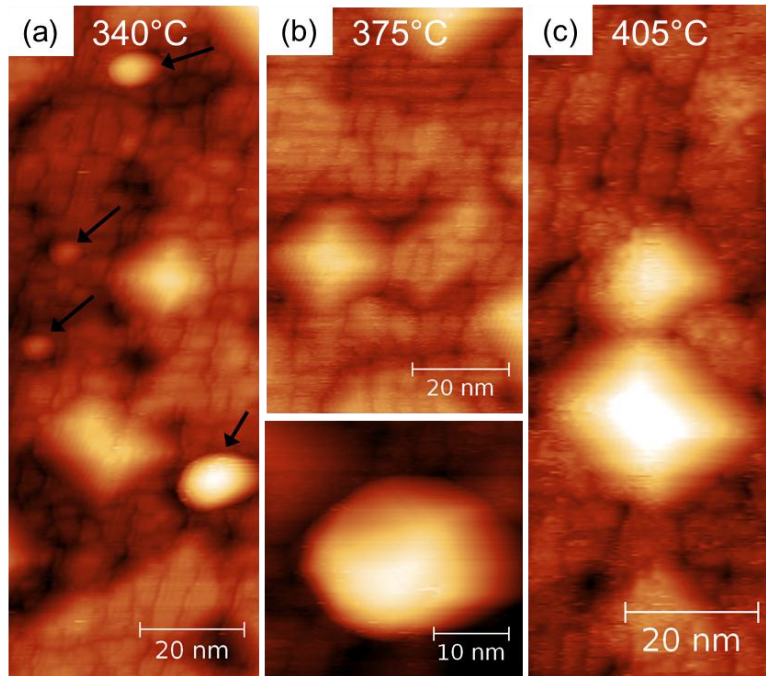


Figure 5.5. STM image of sample annealing temperatures at (a) 340°C, (b) 375°C, and (c) 405°C show Ge QDs alongside secondary structures. In (a) secondary structures are noted by an arrow. All images were obtained with a sample bias of -2.0 V.

As shown in Figure 5.5(a-c), at increasing annealing temperatures, from 340°C to 405°C, small Mn islands are no longer found on the surface. In addition, the quality of the wetting layer recovered and the wetting layer roughness, which was initiated by the Mn deposition, is no longer present. The QD's structure and morphology is preserved up to these temperatures. New structures are observed on the surface which are thought to be a Mn containing secondary phase. In Figure 5.5(a) these secondary structures are pointed out with an arrow and in Figure 5.5(b) a large secondary structure is shown in a higher resolution image. As an initial model we can assume that the Mn diffused out of the wetting layer and lead to the formation of the secondary structures.

5.4. GeQDs and Mn Islands: Scanning Tunneling Spectroscopy

In Figure 5.6, a series of STM images is shown, where the bias voltage was varied between +2.0 V and -2.0 V. This voltage dependent series of images can reveal variations in the local density of states and is sensitive to the bonding state at the surface. The same approach was used to study the bonding of the Mn wires on the Si(100) surface, which is discussed in Chapter 3. In the case of the Mn islands on Ge QD, there were no dramatic changes in the structure of the islands. There are slight changes to the apparent size of the islands, most notably in Figure 5.6(e). Unrelated to the Mn islands, one can note the change in the apparent structure of the Ge QD facet background from a buckled structure for the filled state images, Figure 5.6(a-d), to an apparent square lattice for the empty state images, Figure 5.6(e-g). This observation reflects the variation in the local density of states for the empty state images from the dangling bonds of the dimerized structure [177].

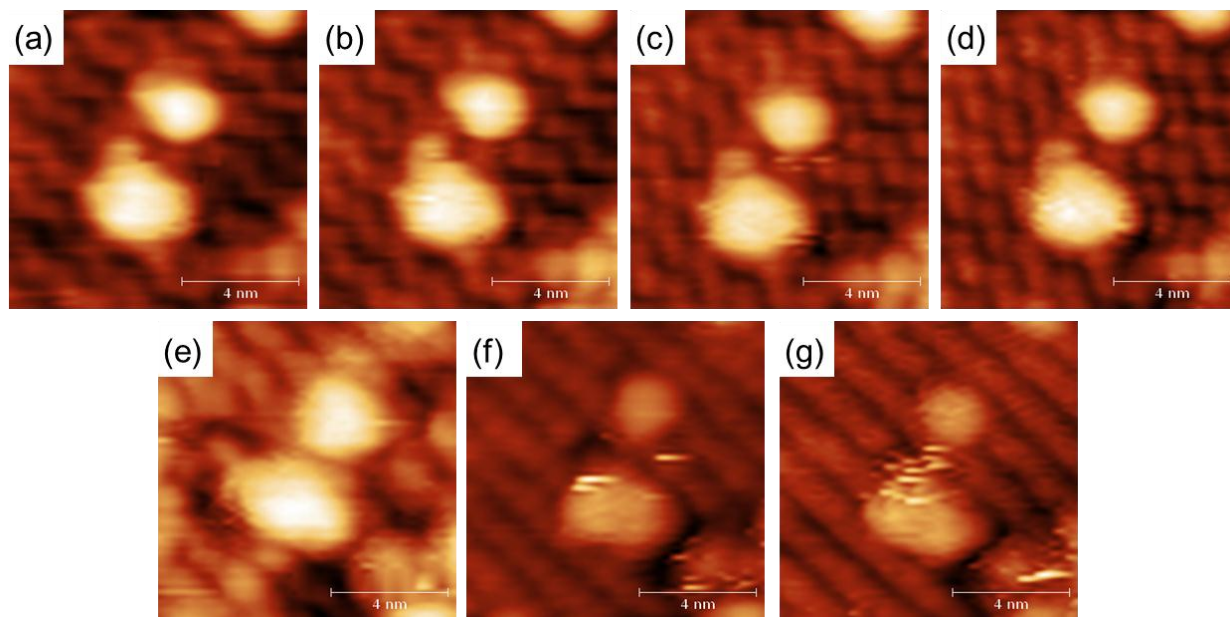


Figure 5.6. A collection of STM images at varying sample biases of the same two Mn islands on a Ge QD (105) facet. The sample biases are as follows: (a) -1.4 V, (b) -1.6 V, (c) -1.8 V, (d) -2.0 V, (e) +1.6 V, (f) +1.8 V, and (g) +2.0 V.

In Figure 5.7, scanning tunneling spectroscopy (STS) of the Ge QDs and wetting layer without and with Mn across the different experimental steps are shown. The STS here was obtained by performing point spectroscopy. During the acquiring of a standard STM image, points are selected and a spectrum is acquired defined by preselected parameters. The spectra are taken -1.5 V to +2.0 V with 50 increments. An example STM image where several point spectroscopy measurements were taken is shown in Figure 5.7(a). Throughout Figure 5.7(b-d), each set of spectra measured per image were averaged across 20 – 30 separate point spectroscopy measurements. The STS spectra are measured as an I-V curve and were differentiated, dI/dV , and plotted versus the sample bias.

The spectra displayed in Figure 5.7(b) were taken from Ge QDs and the surrounding wetting layer before the Mn deposition. The sudden decrease in dI/dV around -1.4 V is a measurement artifact. The band gap of the two different surfaces are effectively identical at about 1.6 eV. Compared to literature values, the band gap measured here is twice as high. Comparatively, the two other sets of spectroscopy data, Figure 5.7(b) and (c), have a noticeably smaller band gap, on the order of 0.7 eV. The source of the larger band gap is not clear; an oxide on the tip that disrupts spectroscopy measurements would do so consistently despite changes in the band gap or electronic structure of the surface. For this reason and the consistency of the spectroscopy measurements across several points and images, the tip does not appear to have an oxide layer present which disrupted the spectroscopy measurements.

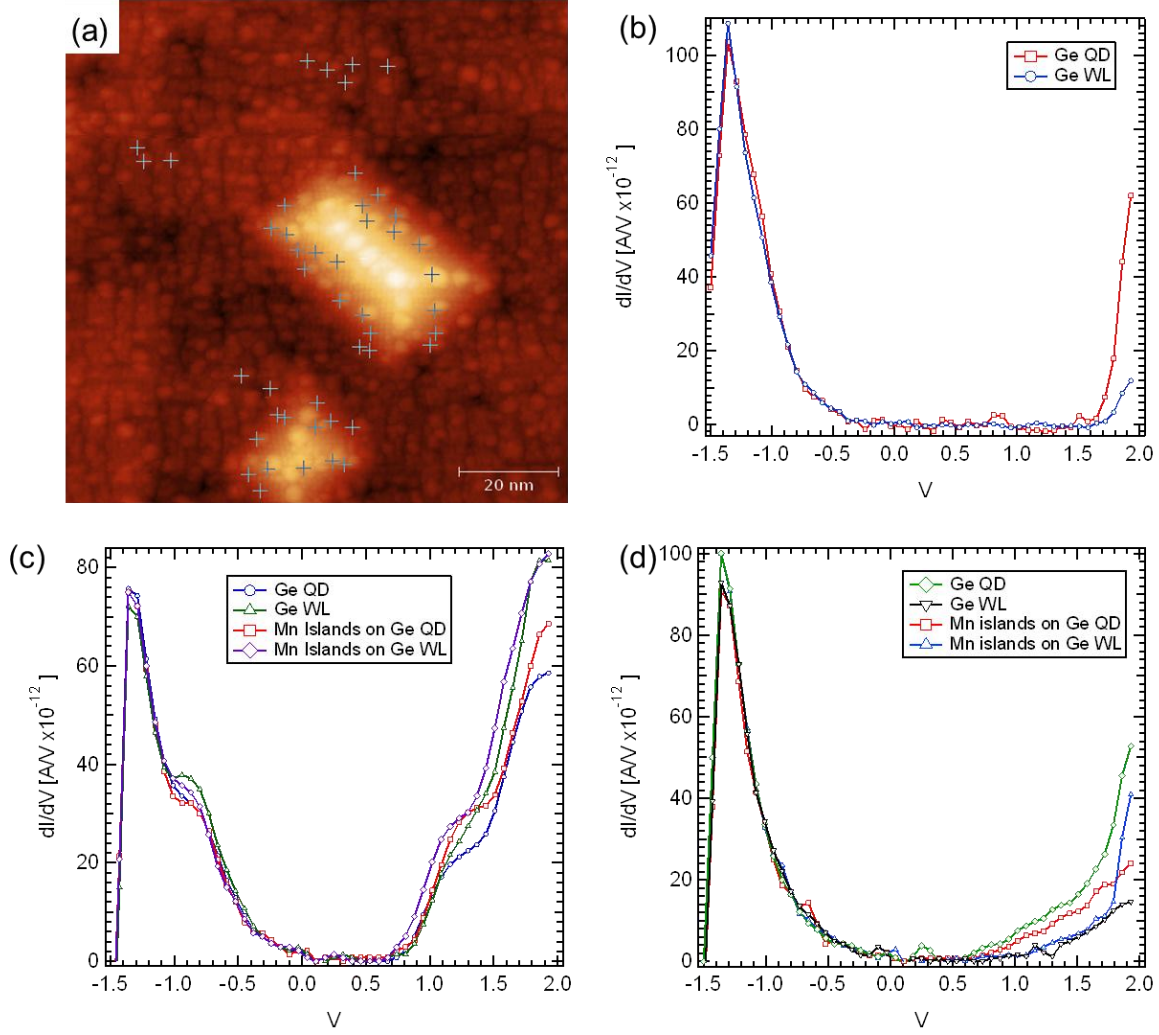


Figure 5.7. (a) An STM image with points marked where spectroscopy was measured. Point spectroscopy of (b) Ge QDs and WL before Mn deposition, (c) Ge QDs, WL, and Mn after Mn deposition, and (d) Ge QDs, and Mn islands after anneal.

Spectra after Mn deposition, as seen in Figure 5.7(c), were obtained from Mn islands on the Ge wetting layer and on Ge QD facets. Spectra from the exposed, uncovered, Ge wetting layer and Ge QDs are also plotted. The structure of the spectra are similar across the different structures. One should also note the structure change, the addition of a shoulder, to the spectra when comparing Figure 5.7(b) and (c). The presence of the shoulder also effectively reduces the band gap with the addition of Mn. In Figure 5.7(d), the structure of the spectra changes again. A distinct shoulder on the filled state portion is no longer present and similarly on the empty state

portion there is a tail of states extending into the band gap. The evolution of the band gaps for the Ge and Mn will be discussed further in the following section.

5.5. Discussion

The distribution and shape of the Mn islands on the Ge QD facets can be used to infer several aspects of the interaction of Mn with the underlying Ge. To start, the Mn islands are flat and have an apparent height which indicates the islands are 1-2 atoms tall. Mn islands displayed a preference for adsorbing on the facet edges, which can be expected since the edge atoms of the Ge QDs are at a higher energy state since not all bonds are satisfied. The adsorption site preference of the Mn islands indicates that the room temperature mobility of Mn is still appreciable. The distribution of the Mn islands also showed no preference for adsorbing across the strain field of the QDs. In addition, the shape of the Mn islands, a preference for elongated flat islands, could also indicate an influence from the Ge{105}-(2x1) reconstruction due to preferential diffusion pathways or confinement due to bonding with the underlying Ge reconstruction. Predominately the islands were elongated along the $[\bar{5}11]$ direction on the (105) facet. The $[\bar{5}11]$ direction is a crystallographically relevant due to the Ge dimers and the direction of the bonds between the atoms that make up the dimers is the same.

The reconstruction of the {105} Ge QD facet has only been accurately described in recent years [177,178]. Currently theoretical work on the diffusion of adatoms on either an unstrained or strained surface have been limited to Ge and Si species [179,180]. In addition, as of yet, no work has been performed which describes the formation of islands or dimers/trimers of adatoms on this particular surface. In this work, we think that the elongation of the islands along the $[\bar{5}11]$ direction, indicates some anisotropy of diffusion for Mn on the Ge{105} surface. In comparison, the previously mentioned theoretical work on Ge diffusion on Ge{105} showed that

at 800K on an unstrained Ge{105} surface diffusion is isotropic between the [010] and $[\bar{5}01]$ directions [179,180]. The unstrained Ge{105} surface models the apex of a quantum dot; the authors also investigated a strained Ge{105} surface and reported isotropic diffusion for Ge as well [179]. Unfortunately additional work on the Ge{105} surface and diffusion of ad atoms is sparse and currently does not include any transition metals for comparison. However, previous work on Mn on Ge(100) substrates and previous work by our group of Mn on Si(100) substrates has revealed some aspects of the behavior of Mn on semiconductor surfaces [16,103,181]. Zeng et. al. showed that the room temperature deposition of Mn on a Ge(100) substrate resulted in the formation of clusters [181]. The authors indicated that the clusters had an apparent height of approximately 0.35 nm compared to an average height of 0.22 nm for our clusters on Ge(105) QD facets. In comparison, our previous work on room temperature deposition of Mn on Si(100)-(2x1) showed that Mn is mobile enough to assemble into wire structures only 1 or 2 atoms wide [16,103]. In addition, the work by Zeng et. al. showed that the Mn had little influence on the reconstruction immediately surrounding the clusters. This is in contrast to the room temperature deposition of Mn on the strained Ge(100) wetting layer which leads to substantial roughening.

One point of interest is the substructure of the Mn islands and degree of interaction with the underlying Ge QD facets. Two specific islands imaged with particularly well resolved Mn islands indicated a strong interaction with the Ge facets, see Figure 5.2(d). Both islands in the smaller scale image show the higher contrast region of the island ending abruptly where the Ge{105}-(2x1) reconstruction periodicity ends. In addition, around one island the absence of a Ge atom is noted, pointed out with an arrow. These results indicate that Mn islands can distort and interrupt the Ge surface reconstruction. This is indicative of a strong interaction with surface.

It is not likely that the missing Ge is simply a defect since no point defects were imaged on Ge QD facets prior to Mn deposition.

The annealing portion of the experiments revealed the behavior and evolution of the Mn islands across several temperatures. Considering the average island height and average island long-axis length, there are two stages in the evolution of the Mn islands. The island long-axis length increases at a lower temperature before an increase in the apparent height of the islands can be detected. This indicates that in the attachment of ad atoms to Mn islands is anisotropic and two activation barriers can be distinguished: the first to overcome before an island will increase in lateral size and the second to overcome before an island will increase in height. This is indicative of a diffusion barrier for adatoms to move onto the island. Up to a temperature of 150°C, the projected area of the Mn islands stays constant, which implies a rearrangement of adatoms within a given island. From room temperature to 150°C, the Mn islands are shown to nearly double in total volume per unit area. This could indicate an intermixing of Ge and Mn or the change in lateral size and height are a result of substantial change in bonding.

The annealing experiments revealed that the Mn islands are relatively stable at low temperatures (up to 150°C), but larger round clusters with a size on the order of 12 nm and a height of 2 – 3 nm dominate for temperatures above 340°C and the small flat island have disappeared. The composition of the large clusters is unknown, but their appearance is uniquely linked to the presence of Mn on the surface. We currently do not have an analytical method which would determine in a reliable manner the Mn-concentration in small clusters with the required spatial resolution and element sensitivity. The Mn concentration in the Ge QDs and wetting layer is likewise not known at present and can be influenced by the loss of a fraction of Mn through re-evaporation.

The electronic structure of the Mn islands and the surrounding Ge was probed with STM images of varying sample biases and point spectroscopy. In image series across several sample biases, there were minor changes in the structure of the islands with sample bias. Due to poor imaging and insufficient contrast at lower sample biases, the sample biases utilized were limited to relatively high values, greater than -1.4 V for filled state images and 1.6 V for empty state images. In the 1.6 V sample bias image, the apparent projected size of the Mn islands increases, though there is no relative apparent height increase, relative to the Ge surface. This lateral size increase relative to images at other biases can indicate strong bonding between the Mn islands and the Ge. In addition, there are depressions surrounding the larger of the two Mn islands where in the filled state images there are clearly Ge dimers present. These effects do suggest bond formation between Ge and Mn after room temperature deposition.

The point spectroscopy data reveals more electronic structure changes with the Mn islands as a function of annealing. There are some inconsistencies with some key features of the spectroscopy data presented here when compared to other STS and theoretical studies. For instance, the band gap for the Ge surface without Mn from our study was found to be approximately 1.6 eV. Other studies have reported a band gap for Ge (105) thin films on Si(105) of 0.8 – 0.9 eV [178,182]. However, as discussed in the results section, the large band gap does not appear to be the result of an oxide layer on the tip. The source of the density of states changes in the spectroscopy measurements can be traced to the different experimental steps: Mn deposition and annealing.

5.6. Summary

In summary, the room temperature deposition of Mn on Ge QDs and the wetting layers leads to the formation of small, 1 – 2 atom high, islands. On the wetting layer, the Mn islands cause a

disruption in the reconstruction and this disruptions manifests itself as a roughening effect likely cause by strain relief. Notably, this roughening is recoverable after annealing samples above 200°C. Mn islands on QDs are shown to have preferential absorption at facet edge sites due to increased disorder at the facet edge. On the QD facets, the Mn islands were shown to cause bias dependent changes to the surrounding Ge atoms indicating bond formation between Ge and Mn after the room temperature deposition. The Mn islands were found to ripen with increasing annealing temperature, first increasing in projected size and subsequently in height at higher temperatures. Above 200°C, Mn islands increase sufficiently in mobility to begin the formation of larger, potentially Ge-Mn intermetallics, secondary structures.

Chapter 6. $\text{Mn}_x\text{Ge}_{(1-x)}$ Quantum Dots: Co-deposited Nanostructures and Magnetic Properties

A different method to achieve Mn doping in Ge QDs, is the co-deposition of Ge and Mn during a typical QD growth. In this section the formation of $\text{Mn}_x\text{Ge}_{1-x}$ QDs is studied using STM and SEM while the composition and magnetic properties are investigated using SAM and XAS/XMCD. Parts of this chapter were done in collaboration with colleagues at UVA and other institutions. The SEM/SAM work was performed at Brookhaven National Laboratory with Joseph Kassim with the assistance of Eli Sutter and Peter Sutter. Kiril Simov and Petra Reinke performed the XAS/XMCD experiments at Lawrence Berkeley National Lab with the assistance of Per-Anders Glans, Catherine Jenkins, and Elke Arenholz.

6.1. Experimental Details

Si(100)2x1 reconstructed substrates were prepared as described in Section 2.4. Ge and Mn were co-deposited onto a substrate held at 450°C. Ge was evaporated from a Veeco effusion cell at a rate of 0.03 Å/s. The Mn concentration in the co-deposited samples was controlled via the Mn flux. Mn was evaporated from a Mo crucible from an electron bombardment evaporator (Mantis Deposition Quad EV), and samples with Mn concentrations of 5, 8, 10 and 23 % (based on relative fluxes) were prepared. Most samples were capped with a 5 nm thick Ge film at room temperature before removal from the STM chamber.

Additional samples were grown and analyzed at the Center for Functional Nanomaterials (CFN) at Brookhaven National Laboratory using an Omicron Nanoprobe system equipped with a UHV Gemini Scanning Electron Microscopy (SEM) and Auger analyzer for Scanning Auger Microscopy (SAM) capabilities. The same Si substrates and cleaning procedure was used as described above in a preparation chamber attached to the analysis chamber with a base pressure

of 1×10^{-9} mbar. To compensate for the higher base pressure, Ge and Mn were co-deposited onto the substrate held at 450°C within five minutes following the final Si flashing step.

All STM images were obtained in constant current mode with a sample bias of -2.0 V (filled states) and +2.0 V (empty states) and a feedback current of 0.03 nA. Electrochemically etched W wire was used as a tip material. Imaging conditions can be found in the figure captions. Electrochemically etched W-wire was used as a tip material. Image analysis was performed using ImageJ, [110] WSxM [111] and Gwyddion [174] software packages.

The magnetic properties of the samples were tested using a Quantum Design Physical Property Measurement System operating in VSM mode. Samples were mounted on quartz paddles using wax which was tested separately and shown to have no ferromagnetic or paramagnetic response down to 5 K under a field of 2 T. The elemental specific magnetic measurements using XAS/XMCD were performed at beamline 6.3.1 at the Advanced Light Source at Lawrence Berkeley National Laboratory. The samples were held in a tunable field (± 2 T) with a circularly polarized soft x-ray beam (60% polarization) oriented at an angle of 60° with respect to the surface normal. Sample measurements at beamline 6.3.1 were cooled to 30 K using liquid He.

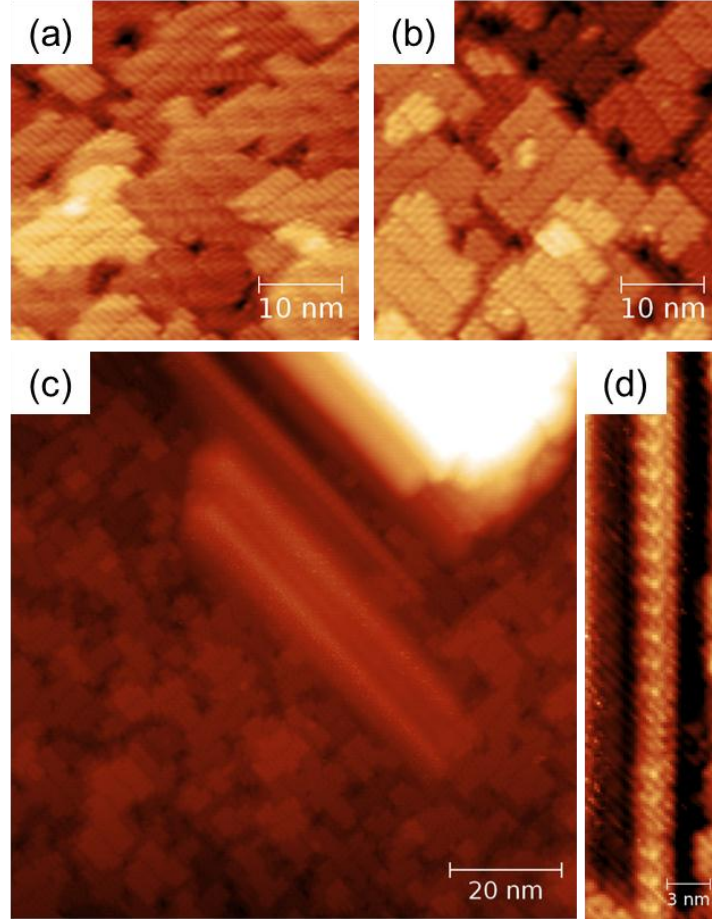


Figure 6.1. Several STM images of co-deposited Ge and Mn after 1.5 ML to 2 ML are shown. Mn concentrations of (a) 5 %, (b) 10 % and (c,d) 23%. All images were acquired with an imaging bias of -2.0 V.

6.2. STM Results of Growth

The results section is presented first discussing STM images of co-deposited Ge and Mn after 1.5 to 2 ML are deposited and after 4.5 to 5 ML are deposited. Figure 6.1 includes STM images of the $\text{Mn}_x\text{Ge}_{1-x}$ wetting layer where the growth was stopped after 1.5 to 2 ML were deposited. Mn concentrations of 5 % [Figure 6.1 (a)], 10 % [Figure 6.1 (b)] and 23 % [Figure 6.1 (c,d)] are depicted. Interrupted wetting layer growths are expected to show tile-like regions of 2x1 and 4x2 reconstructed Ge atoms. The reconstructed tile areas are bound by dimer vacancy lines (DVLs) which form within the first monolayer of epitaxial Ge growth on Si(100). In Figure 6.1, the

quality of the wetting layer and the surface reconstruction is independent of the Mn concentration. The quality of the wetting layer is characterized by the presence of the Ge(100)2x1 and 4x2 reconstructions on the surface, and the density of the dimer vacancy lines, which defines the size of the tile regions. Both features are not modified by the addition of Mn.

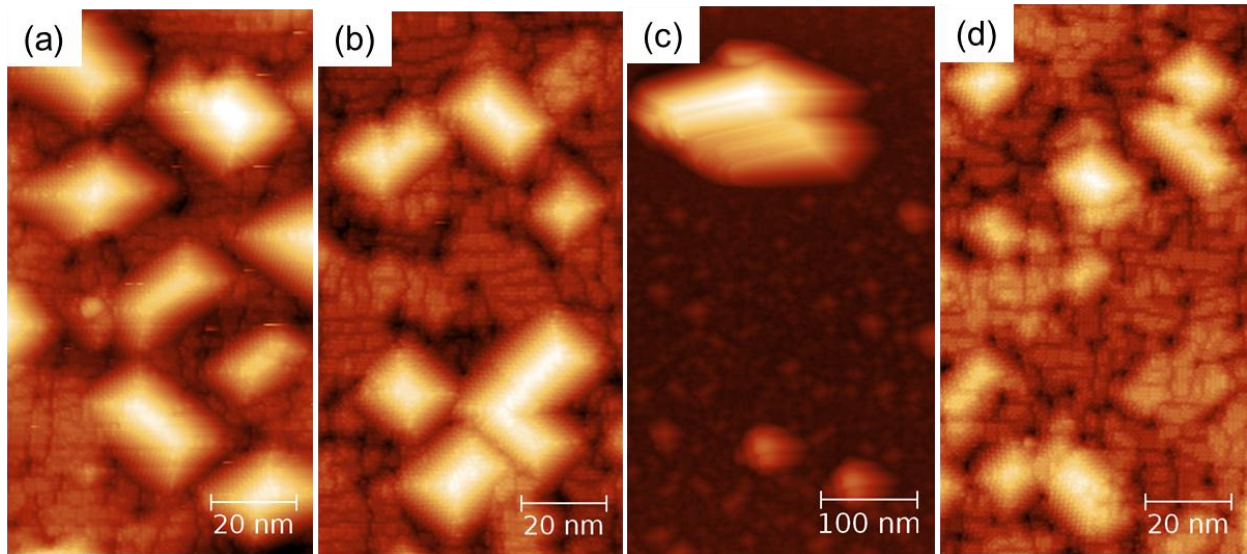


Figure 6.2. Several STM images of co-deposited Ge and Mn after 4.5 ML deposition are shown. Mn concentrations of (a) 8 %, (b) 10 % and (c,d) 23%. All images were acquired with an imaging bias of -2.0 V.

However, secondary structures form at higher Mn concentration, 23 % Mn. The secondary structures appear rod-like and in bundles. In the STM images, it is difficult to determine if the secondary structures are embedded in the Ge wetting or extend into the Si substate. Cross sectional TEM work by our collaborators, Joseph Kassim and Prof. Jerrold Floro, on similar films grown in a separate chamber indicate that the secondary structures do indeed extend into the substrate. The long axis of the rod structures are along the [110] direction, and a particularly well resolved image of the secondary structures is shown in Figure 6.1(d).

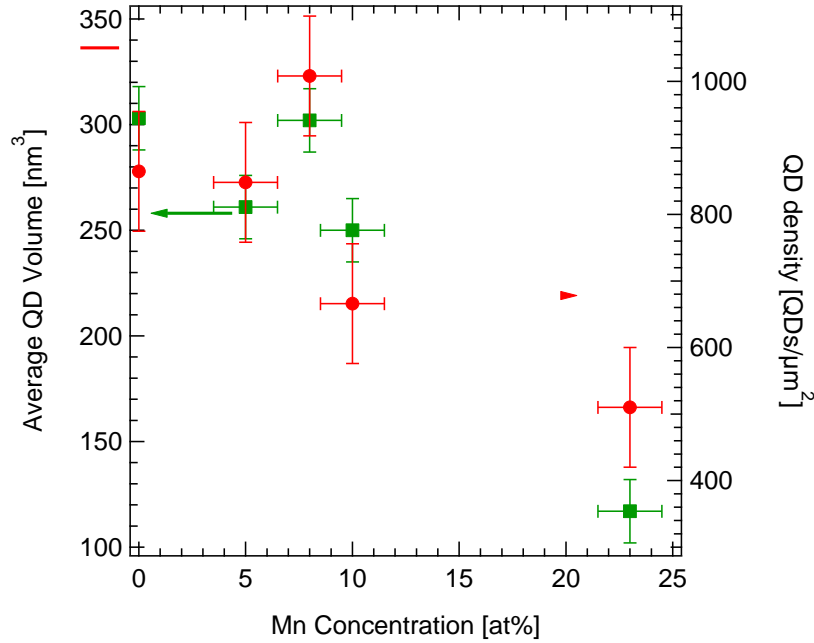


Figure 6.3. Plot of the average volume of QDs (left axis, green data points) and QD density (right axis, red data points) as a function of Mn concentration.

Full mature growths of $\text{Mn}_x\text{Ge}_{1-x}$ QDs, primarily consisting of hut/pyramid islands, are shown in Figure 6.2. The concentration of Mn varies from 8 % [Figure 6.2(a)], 10 % [Figure 6.2(b)] to 23 % [Figure 6.2(c,d)]. As can be seen in Figure 6.2(a,b,d), $\text{Mn}_x\text{Ge}_{1-x}$ hut/pyramid islands formed and are comparable to hut/pyramid islands seen for Ge-only depositions, qualitatively (see Figure 5.2 in Chapter 5). The quality of the QDs were evaluated based on the fidelity of the expected $\text{Ge}(105)2\times 1$ rebonded step reconstruction, the presence of defects on the facets, and the morphological properties of the QDs. The QDs for each growth, with otherwise near identical growth conditions, vary slightly with increasing Mn concentration. Notably at 23 % Mn, the QDs are noticeably smaller than those of the lower Mn concentration growths. As with the interrupted wetting layer co-deposition, at the highest Mn concentration studied, 23 %, secondary structures can be observed, shown in Figure 6.2(c). Such structures are difficult to resolve due to large height and steep sides even with slow scan speeds. The full QD growth secondary structures

appear to be rod-like bundles as with the secondary structures observed for the interrupted wetting layer sample, Figure 6.1(c). To further describe the effect of Mn on the growth of Ge QDs, quantitative analysis of the $\text{Mn}_x\text{Ge}_{1-x}$ QDs are shown in Figure 6.3. QDs were evaluated for number density and the average volume as a function of Mn concentration. As shown in Figure 6.3, with increasing Mn concentration both the average QD volume and QD density decreases. Within error, the QD density is seen to start to decrease at 10 % Mn and further so at 23 % Mn. Whereas the average QD volume tended to decrease with statistical significance only at 23 % Mn.

6.3. SAM Results of Growth

Separate samples were grown in an attached chamber to an Omicron Scanning Auger Microscope at Brookhaven National Lab (BNL). As with the samples grown at UVA in our STM chamber, several samples with varying Mn concentration were grown. Without a quartz crystal rate monitor at the BNL chamber, the Mn concentrations are estimated from rate calibrations on the STM chamber. Though the sources and materials used at Brookhaven for the depositions are the same used here at UVA, the error from this estimation could be large since the chambers have different geometries and background pressures.

Overview SEM images of two samples grown at BNL are shown in Figure 6.4. Shown at a magnification of only 15,000X, some structures can be difficult to identify, but the overall impression of the density of the rod-like structures (as seen in the STM studies) is well represented. In Figure 6.4(a) the sample has an estimated Mn concentration of 18 % Mn and Figure 6.4(b) has an estimated Mn concentration of 28 % Mn. Particularly in Figure 6.4(b) the rod-like structures are the dark linear structures that are 250 nm – 750 nm long.

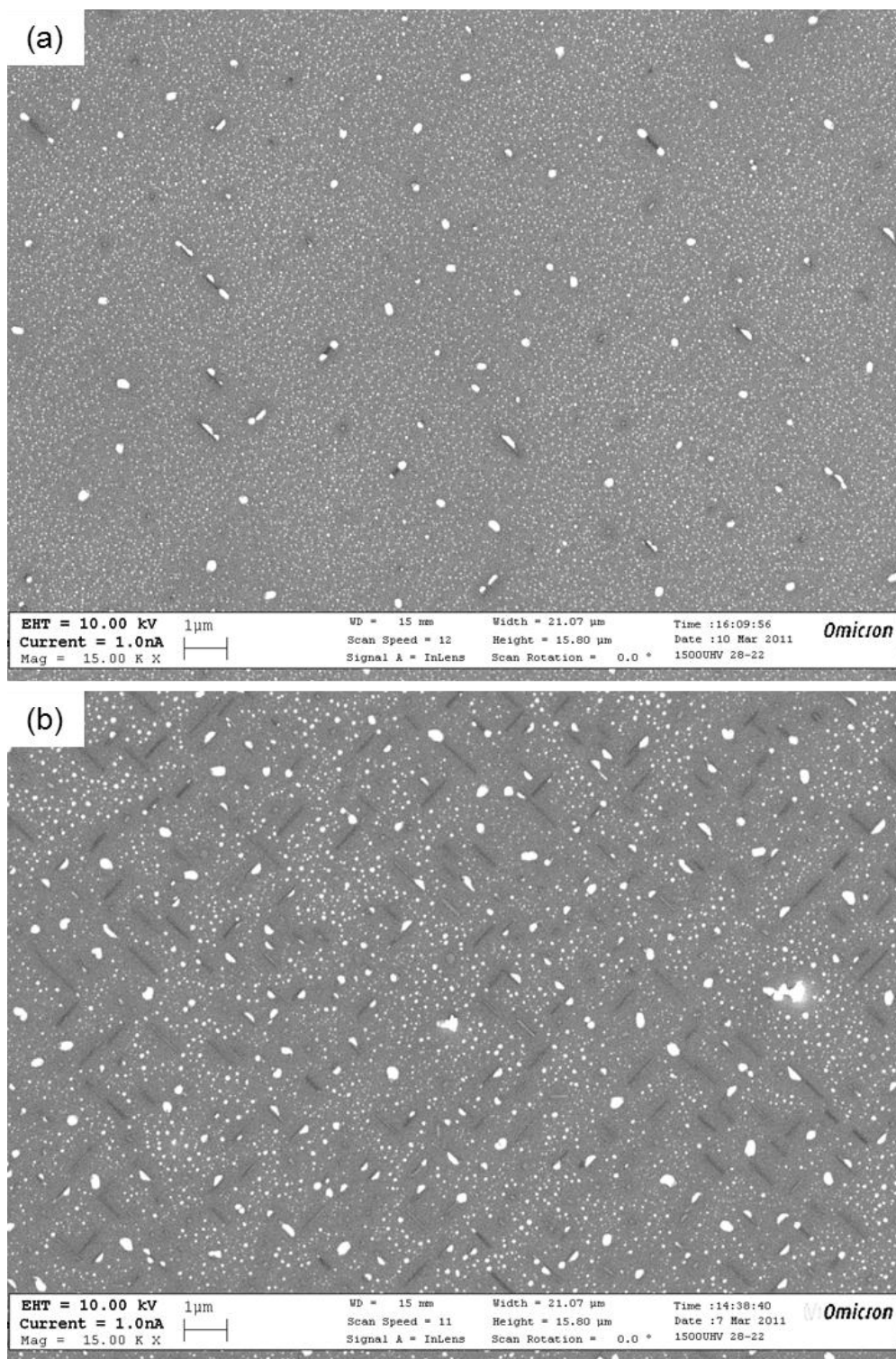


Figure 6.4. SEM images acquired at an acceleration voltage of 10 kV and probe current of 1.0 nA. Two Mn concentrations are shown: (a) 18 % Mn and (b) 28 % Mn.

Since thicker $\text{Mn}_x\text{Ge}_{1-x}$ films were grown, our growth regime of QDs included the formation of both hut/pyramid QDs and dome QDs. The huts are difficult to image and do not show up in the low magnification SEM images. The domes and some superdomes are the small, 50 nm and 100 nm across, bright features in the SEM images. Around the secondary structures, depletion zones are evident where very few QDs are present. The average distance between the secondary structures of the different Mn concentrations was found to be 1.8 μm (28 % Mn), 8.7 μm (18 % Mn), and 6.3 μm (10 % Mn). The thickness of material deposited for each sample varied as follows: 14 Å (28 % Mn), 9.6 Å (18 % Mn), and 14 Å (10 % Mn).

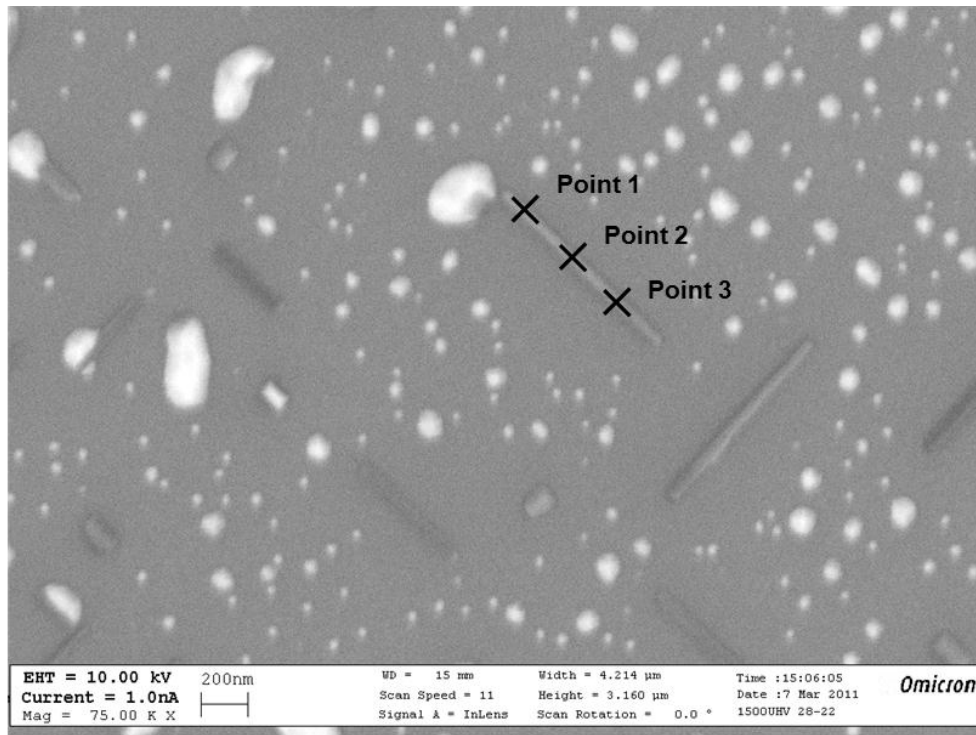


Figure 6.5. SEM image acquired at 10 kV with a probe current of 1.0 nA. The Mn concentration is 28 %. The three points indicated by their markers represent the points of interest selected to perform point Auger electron spectroscopy.

In Figure 6.5, an example of a high resolution SEM image is shown from the 28 % Mn sample. In the image, the rod-like secondary structures are shown along with dome and superdomes. On some QD structures some contrast between different facets is achieved. There

are three points marked in Figure 6.5 where point AES was performed. The Auger spectra obtained for the Ge LMM and Mn MNN peaks for “point 3” are shown in Figure 6.6(a) and (b), respectively. In order to calculate the concentration of Mn, the Ge peak was used as the reference to find the relative concentration of Mn. In the Auger spectra, the data was smoothed with an 11-point box averaging. The main peaks and their shoulders were included in numerical integration and the Mn concentration was calculated as the Mn peak area divided by the summation of the Mn and Ge peaks.

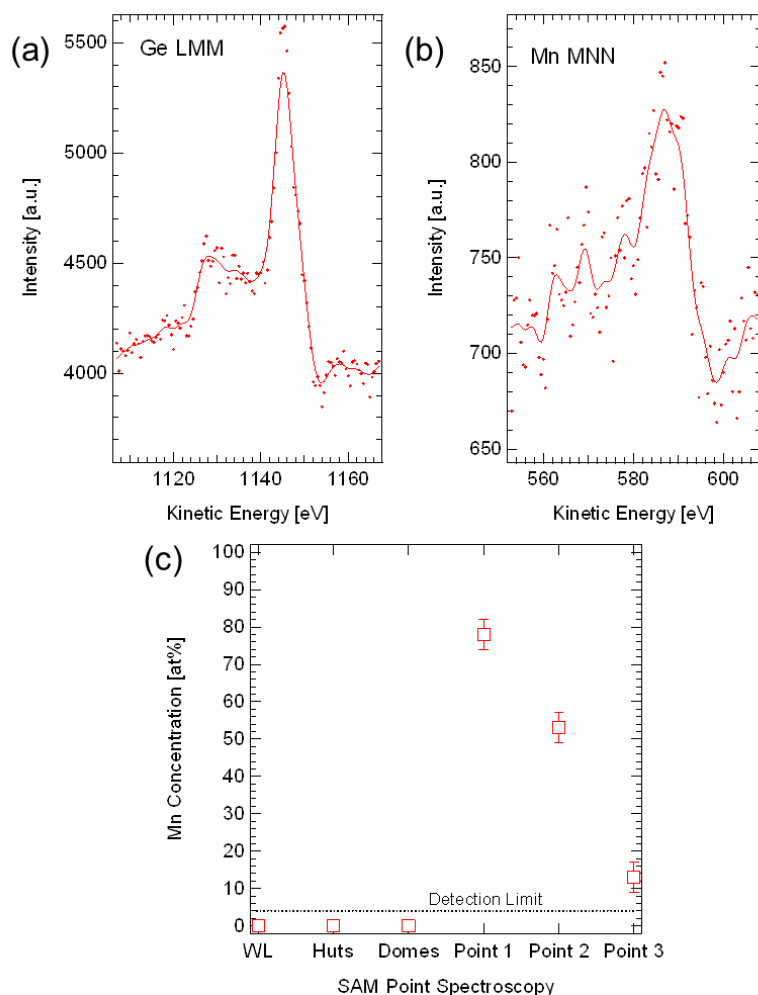


Figure 6.6. The (a) Ge LMM and (b) Mn MNN Auger peaks are shown for “point 3.” These two peaks are representative for other peaks used in the calculation of the Mn concentration of secondary structures. (c) The Mn concentration is plotted as a function of the selected point.

In Figure 6.6(c), the Mn concentration along the length of the rod structure from Figure 6.5 is plotted. The Mn concentration varies along the length of the rod from 13 % to 78 %. Other rod structures from this sample were probed at single points and a Mn concentration of 30 % was calculated. Other structures were probed as well among all samples such as the wetting layer, domes and superdomes. The Mn peak could not be identified in a reliable manner for the wetting layer, huts, domes or superdomes. The sensitivity of the Auger probe in this setup was estimated to be about 5 % based on the size of the probe (5 nm) and the limited probe current.

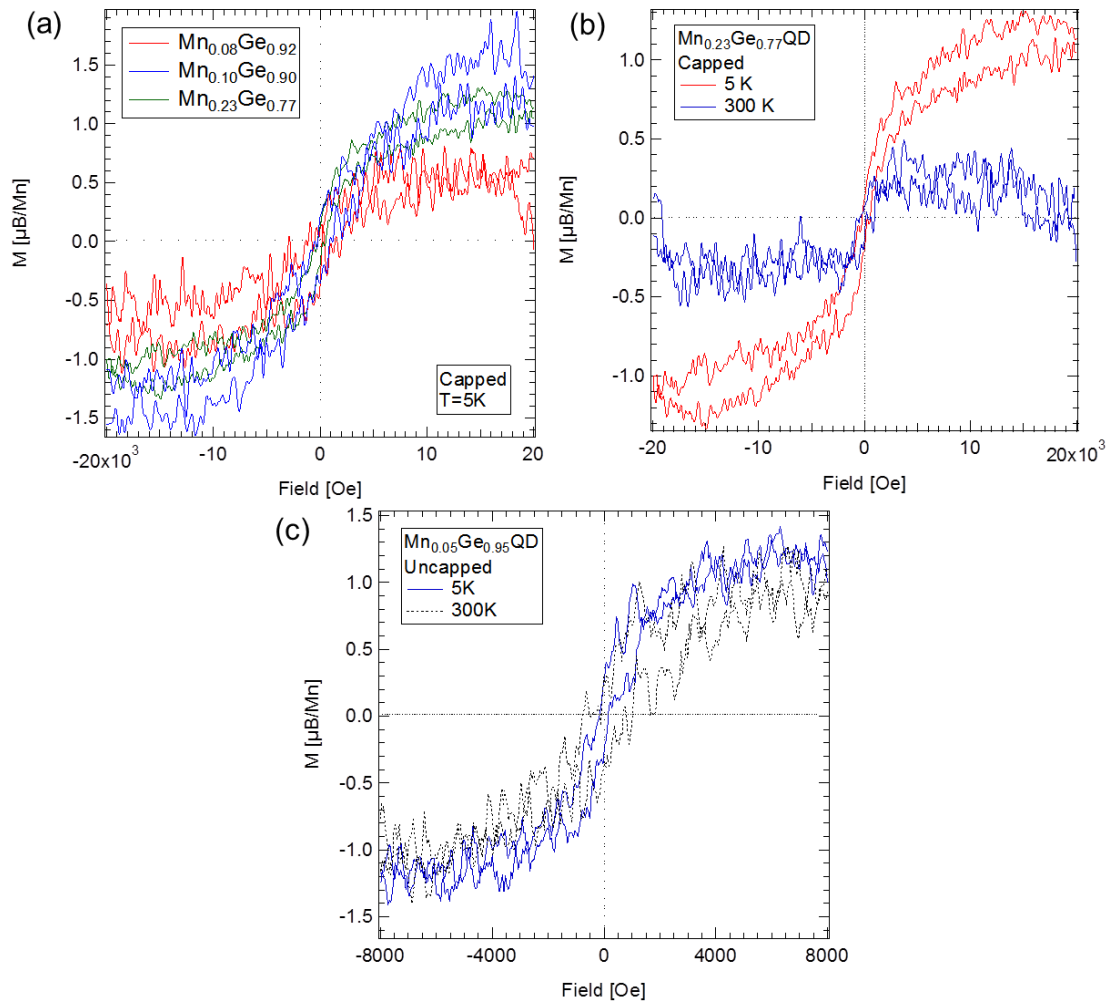


Figure 6.7. (a) VSM M-H loops (± 2 T) of 8 %, 10 %, and 23 % Mn capped samples at 5 K. (b) VSM M-H loops for (± 2 T) of 23 % Mn capped sample at 5 K and 300 K. (c) VSM M-H loops (± 0.8 T) of 5 % Mn capped sample at 5 K and 300 K.

6.4. Magnetism Results: VSM and XMCD

The magnetic properties of the co-deposited QDs were probed with VSM and XMCD. In preparation for magnetic measurements, most samples were capped at room temperature with a 5 nm thick Ge layer. One sample was completed without a capping layer and this sample was also studied with XAS/XMCD. VSM Magnetization vs. Applied Field (M-H) loop results of the capped samples are shown in Figure 6.7(a) and were obtained at 5 K. The low concentration, 8 % and 10 %, Mn samples have a T_C around 50 K and a magnetization of $0.5 \mu_B/\text{Mn}$ for the 8% Mn sample at 5 K. The highest Mn concentration sample has a T_C near 300 K. VSM of the uncapped sample shown in Figure 6.7(c) has the M-H loop at 5 K and 300 K. The saturation magnetization of the 5% uncapped sample is approximately $1.1 \mu_B/\text{Mn}$.

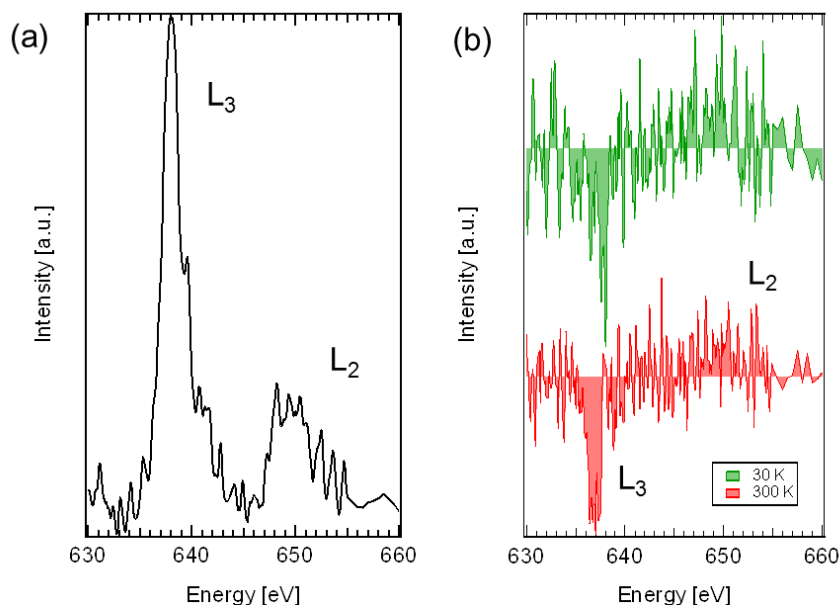


Figure 6.8. (a) XAS of the Mn 2p absorption peak. (b) XMCD of the Mn 2p absorption peak obtained at 30 K and 300 K.

Samples taken to Lawrence Berkeley National Lab were analyzed using XAS and XMCD to measure the element specific magnetism. Samples with 5%, 8%, 10%, and 23% were measured. Of these samples, the three higher Mn concentration samples received a capping layer and did

not return a significant Mn signal above the background since the capping layer thickness was on the same order as the information depth for this technique. The lowest concentration sample, 5% Mn, which was uncapped is the main focus of the following XAS and XMCD results and discussion. The x-ray absorption spectra for the 5 % Mn uncapped sample is shown in Figure 6.8(b). The Mn 2p, L₃ and L₂, peak is shown in the figure. After sampling the x-ray absorption spectra with two opposing applied magnetic fields, the spectra were aligned at the L₂ peak maximum and subtracted from each other. The result of the subtraction is XMCD as shown in Figure 6.8(b). The sample was measured at two temperatures, 300 K and 30 K. By convention, the L₂ response is shown as a negative peak and the L₃ response as a positive peak. Using Chen's sum rules the saturation magnetization due to Mn is 1.19 μ_B/Mn which is in good agreement with VSM data [91]. The spin and orbital components of the magnetization is found to be 1.06 μ_B/Mn and 0.07 μ_B/Mn , respectively.

6.5. Discussion

At growth temperatures typical for Ge QD growth, the addition of Mn to the system would be expected to form secondary phases and possibly alter the surface structure of the system. Though transition metal contacts are used often in Si-based technology, the formation of these contacts leads to far reaching changes of the surface. As discussed in Chapter 3 the introduction of Mn and other transition metals and temperatures similar to Ge QD growth temperatures produces highly defective surfaces. Dimer vacancy lines form with a spacing of a few nanometers and run the length or width of a terrace. In the growth of $\text{Mn}_x\text{Ge}_{1-x}$ QDs, the presence of Mn at low concentrations was demonstrated to have very little effect on the growth quality of the quantum dots. This contrasts with the effects seen from sub-monolayer depositions and high temperature annealing of Mn and other transition metals on Si(100) and Si(111).

By increasing Mn content in samples, the eventual formation of secondary phases can point to a supersaturation of Mn in the Ge matrix, which leads to, above a critical concentration, the nucleation and growth of secondary phases. For the low concentration samples, the lack of secondary phases indirectly indicates that Mn has been incorporated into the system. Additionally, it is known from the XAS data that Mn is indeed present in the sample for the 5 % Mn sample.

Considering the higher concentration samples, it is possible that the lower density and smaller quantum dots are a result of simple mass conservation required with the formation of secondary phases. It is assumed here that the secondary phases are comprised of purely Mn and Ge. As a first order approximation, assuming Ge-Mn only secondary phases, the amount of germanium in the secondary phases was estimated as the difference between the amount of germanium deposited and amount of Ge in the wetting layer and Ge QDs as shown in Figure 6.9(a). The wetting layer is assumed to be 3 ML thick and the volume occupied by the Ge QDs was obtained by flooding analysis of a large area (500 nm x 500 nm) STM image. However, the assumption of a purely Mn-Ge secondary phase is likely an oversimplification. There is evidence from our collaborators that the secondary phases are indeed ternary compounds of Ge, Si, and Mn. The chemical analysis of such structures is difficult on a Si substrate due to a constant Si signal. In the case of the Auger spectroscopy, we were unable to detect an appreciable Si signal difference between the secondary phases and the surrounding structures.

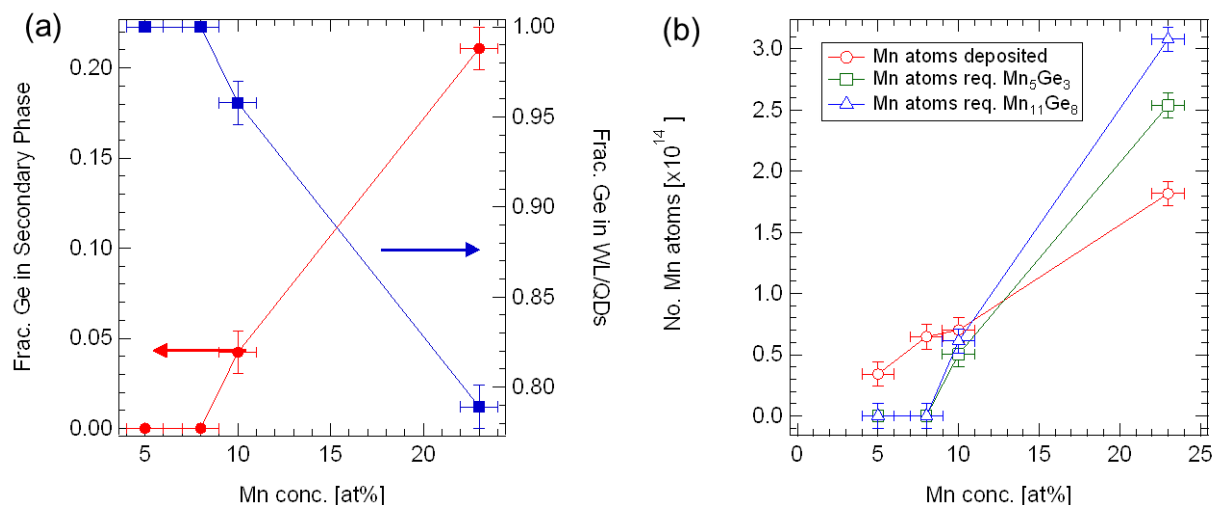


Figure 6.9. (a) Based on the known volume of material deposited and the volume of the QDs from STM images, the fraction of Ge in the secondary phases can be estimated. (b) A comparison between the known number of Mn atoms deposited as a function of Mn concentration and the number of Mn atoms required to form a stoichiometric Mn-Ge intermetallic compound.

A first order comparison between the amount of Mn in two possible secondary phases and the actual amount of Mn deposited is shown in Figure 6.9(b). If it is assumed that all deposited Mn is incorporated into the secondary phases, at 23 % Mn there is not enough Mn available to produce a stoichiometric compound for either germanide. However, at 10 % Mn, within error, there is enough Mn deposited to form stoichiometric germanides. Both Mn germanides are robust ferromagnets (relatively high coercivity) but our samples have a low coercivity as can be seen in the VSM M-H loop data. The Curie temperature of the 23 % Mn sample is within 15 K of the expected values for the Mn germanides, 280 – 295 K. Our results suggest that the secondary phases are Mn-poor or are ternary compounds and do have possess magnetic properties which closely describe the two Mn germanide compounds. However, little is known about the magnetism of non-stoichiometric germanides or the magnetism of Si-Ge-Mn ternary compounds.

The combination of a high vapor pressure for Mn and currently unknown sticking coefficient for Mn could point towards evaporation of at least a portion of the deposited Mn. Magnetic responses in the VSM data for the low concentration samples and XAS/XMCD data of the

uncapped sample confirm that Mn is indeed responsible for the magnetic properties of the samples. The 5% Mn uncapped sample is the only sample prepared which shows a room temperature magnetic response and, from inspection with STM, does not contain secondary phases. The shape of the XAS Mn $L_{3,2}$ peak does not show a shoulder on the low energy side of the L_3 peak, which would be indicative of an oxide. The peak shape is the most compatible with the calculations of Mn^{2+} presented by Kang *et. al.* [183]. In addition, all Mn oxides are antiferromagnetic and thus cannot be responsible for the ferromagnetic signature seen in our samples [184]. The XMCD results confirm that Mn is the magnetic species. When comparing the spin and orbital components of the magnetization to known values for Mn compounds, it becomes important to note whether the orbital component is quenched entirely. Our sample had an M_{orb} of $0.07 \mu_B/Mn$ which contrasts to Mn_5Ge_3 where the orbital component is quenched [185]. α -Mn has an orbital component of $0.06 \mu_B/Mn$ and Mn-doped InAs films have an orbital component of $0.04 \mu_B/Mn$ [186,187]. A second sample at a similar concentration, 8% Mn, did not show similar magnetic properties; however, this sample was capped whereas the 5% Mn sample was not. However, it is unclear whether the capping layer has any influence on the magnetic properties of the samples. As discussed above the uncapped sample did not display features in the XAS indicating an oxide.

6.6. Summary

In summary $Mn_xGe_{(1-x)}$ QD samples of varying concentrations have been prepared and characterized with STM. In all samples of varying concentrations, we were able to successfully grow Ge QDs. At the highest Mn concentration studied, secondary phases were observed which are in all likelihood Mn-poor non-stoichiometric germanides or ternary Si-Ge-Mn compounds. Despite the thermodynamically more favorable secondary phases, we were able to suppress the

formation of secondary phases simply by tuning the Mn concentration at a growth of 450°C. The 5% Mn uncapped sample in particular showed a room temperature ferromagnetic response in both VSM and XMCD which cannot be a result of Mn oxide formation. In addition, through a study using XAS/XMCD this sample indicated signatures which are consistent with doping when compared to $\text{In}_{1-x}\text{Mn}_x\text{As}$ and an unquenched orbital component to the magnetization which contrasts to the quenched orbital component of Mn_5Ge_3 . However, compared to other samples with a capping layer, it is not clear if the lack of a capping layer aided in the magnetic properties of the 5 % sample.

Chapter 7. Concluding Remarks

7.1. Conclusions

In the course of this work, we set out to investigate the interactions and segregation of Si, Ge, and Mn in the context of formulating methods to dope Ge QDs with Mn as a building block for spintronics devices. The three different methods to achieve Mn doping are as follows: (1) utilizing the surfactant effect of Mn pre-deposited onto the Si(100)2x1 during the Ge QD growth, (2) accessing sub-surface sites on Ge QDs via the annealing of Mn structures deposited at room temperature on Ge QDs, and (3) co-depositing Ge and Mn during the growth of Ge QDs. The challenges of doping group IV semiconductors lies in the low solubility of Mn which needs to be overcome by choosing kinetically driven processes and the competition to form secondary phases which can be detrimental to the desired magnetic properties.

Method (1) is based on a previous study of Mn on Si(100)2x1 and investigates the previously unexplored temperature regime from room temperature up to the Ge QD growth temperature of 450°C. As previously studied, the room temperature deposition of Mn on Si(100)2x1 results in wire-like nanostructure. In this work, we found that the wire structures dissolve at mild temperatures into clusters. At temperatures around 316°C, Mn is no longer directly observable on the surface and sample bias dependent features revealed Mn had moved into subsurface sites and was acting as an acceptor. Other traditional electronic dopants, such as boron and phosphorus, have been imaged by other researchers similarly as extended high contrast regions, but this was the first time Mn was shown to exhibit this behavior on Si(100)2x1. Beyond this temperature regime, Mn was found to cluster into structures, which likely serve as the nuclei for the subsequent formation of Mn-silicides.

Our experimental results, with the help of collaborators, were compared to theoretical models to determine the atomic structure of the wires. The two models obtained by our collaborators were the two most thermodynamically stable structures which gave good agreement when comparing simulated and experimental STM images. However, none of the models fully describe the experimentally observed wire structure. This is particularly apparent for a comparison of the contrast inversion in the apparent height of Mn wires as a function of bias voltage. In the case of Mn overlayers on a Si(100)2x1 surface, the photoelectron spectroscopy study revealed that the interface between Mn and Si is reminiscent of a Mn silicide. Subsequent Mn layers were shown to be Mn-rich silicides or Mn metal.

In method (2), Mn was deposited at room temperature onto Ge QDs grown to produce primarily hut/pyramid structures. At room temperature, Mn formed into small 1 – 2 atom high islands. The islands formed on both the Ge QDs and the wetting layer. The Mn islands on the wetting layer roughened the surface and proved to be difficult to analyze due to the inherent roughness of that surface on the length scales of the Mn islands. The Mn islands on the QDs were found to cause local disruptions of the surrounding Ge atoms indicating bond formation between the Mn islands and the underlying Ge QD surface atoms. The stability and mobility of these islands were investigated with annealing conditions from approximately 100°C to 450°C. The Mn islands ripen with increasing annealing temperature and up to 150°C the Mn islands undergo small changes in size and position. Above 200°C, Mn islands increase sufficiently in mobility and form larger, potentially Ge-Mn intermetallics, secondary structures. From the STM images, there was no direct evidence that Mn moved into sub-surface sites.

In method (3), Mn and Ge were co-deposited at a typical Ge QD growth temperature to produce $\text{Mn}_x\text{Ge}_{1-x}$ QDs of varying concentrations. The co-deposition method, by our hypothesis,

had the highest risk of forming secondary phases during the growth. However, as shown in this work, we were able to suppress the formation of the secondary phases by growing films with low Mn concentrations, specifically 5 % and 8 % Mn. The uncapped 5% Mn sample in particular showed a room temperature ferromagnetic response in both VSM and XMCD which cannot be a result of Mn oxide formation or a ferromagnetic contaminant such as Fe or Ni. In addition, through the study using XAS/XMCD this sample indicated signatures which are consistent with doping when compared to (In,Mn)As films and also an unquenched orbital component of the magnetization which contrasts to the quenched orbital component of Mn_5Ge_3 . At increasing Mn concentrations, secondary phases did indeed start to form. Our results indicate that we were able to incorporate Mn into the Ge matrix beyond the solid solubility limits, likely resulting from kinetic limitations to the formation of secondary phases.

7.2. Suggested Work

From the one co-deposited Ge-Mn QD sample, there are a few questions that remain. One is location of the Mn within the system. The experiments thus far point to Mn being incorporated in substitutional sites, but it is not known whether there is any segregation of Mn within the wetting layer, quantum dot, or the interfaces. The work of our collaborators will aid in describing this behavior. In regards to the magnetic properties of the 5 % Mn uncapped sample, the above room temperature ferromagnetism this sample possessed is unique among other low Mn concentration samples. It is unclear at the moment whether the lack of a capping layer is a source for these magnetic properties. An additional series of samples at low Mn concentrations with and without capping layers and changing the capping layer material between Ge and Si could help answer this question.

From our study of the co-deposition of Ge-Mn during the growth of $\text{Mn}_x\text{Ge}_{1-x}$ QDs, one question that arose is the exact composition of the secondary phases formed at higher Mn concentrations. Joseph Kassim has performed some work using TEM and EDS that has indicated that these structures are likely ternary MnGeSi compounds. In this thesis, the high Curie temperature, about 300 K, of the 23% Mn co-deposited sample was attributed to the secondary phases, Mn_5Ge_3 or $\text{Mn}_{11}\text{Ge}_8$. The Curie temperature of these two intermetallic compounds is close to room temperature. However, if we indeed are forming ternary compounds, one question that arises is how the substitutional incorporation of Si in the Mn_5Ge_3 structure affects the magnetic properties.

In addition, this study primarily focused on using snapshots of the co-deposition growth at two different stages in the growth to ascertain the influence of the Mn on the QDs. With the knowledge that secondary structures do form at higher Mn concentrations, it would be useful to observe in real-time the influence of these secondary phases on the QD growth kinetics. Using the low-energy electron microscopy (LEEM) we could achieve real-space imaging of the growth in real-time. The LEEM does have resolution limitations (5 nm resolution) compared to the STM and other electron microscopy techniques, but the secondary phases are large enough (as well as the QDs) to be imaged. Ideally the growth would need to be slow enough, over the course of approximately 10 minutes, to make on-the-fly imaging adjustments as the growth progresses. A LEEM study would aim to explore the mechanisms that form the secondary phases. A critical question that has been posed is whether once the secondary phases form, whether they are germanides or ternary compounds, does the Mn in the system become scavenged by the secondary phases and to what extent.

Studying the formation and stability of Mn nanostructures on Si(100)2x1 lead to achieving structures which indicate Mn in sub-surface sites and being electronically active. Further studies into if these sub-surface structures can be preserved and characterized *ex-situ* would be an avenue for future research. The ability to use the sub-surface Mn as a route for Ge QD doping requires further investigation as well. The sub-surface Mn was found to require an annealing temperature of around 316°C which is lower than the required temperatures for Ge QD growth. Further investigation into the stability of the sub-surface structures is warranted to determine if the structures can be preserved up to temperatures required for Ge QD growth.

References

- [1] G. E. Moore, *Electronics* **38**, 114 (1965).
- [2] S. A. Wolf, D. D. Awschalom, R. A. Buhrman, J. M. Daughton, S. von Molnar, M. L. Roukes, A. Y. Chtchelkanova, and D. M. Treger, *Science* **294**, 1488–1495 (2001).
- [3] I. Žutić, J. Fabian, and S. Das Sarma, *Rev. Mod. Phys.* **76**, 323 (2004).
- [4] D. D. Awschalom and M. E. Flatte, *Nat. Phys.* **3**, 153–159 (2007).
- [5] K. W. Edmonds, *Curr. Opin. Solid St. M.* **10**, 108–113 (2006).
- [6] C. Hirjibehedin, C. P. Lutz, and A. J. Heinrich, *Science* **312**, 1021–1024 (2006).
- [7] H. Ohno, *Physica B* **376**, 19–21 (2006).
- [8] S. Kuroda, N. Nishizawa, K. Takita, M. Mitome, Y. Bando, K. Osuch, and T. Dietl, *Nat. Mater.* **6**, 440–446 (2007).
- [9] H. Ohno, *Science* **281**, 951–956 (1998).
- [10] B. Beschoten, P. A. Crowell, I. Malajovich, D. D. Awschalom, F. Matsukura, A. Shen, and H. Ohno, *Phys. Rev. Lett.* **83**, 3073 (1999).
- [11] K. W. Edmonds, G. van der Laan, A. A. Freeman, N. R. S. Farley, T. K. Johal, R. P. Campion, C. T. Foxon, B. L. Gallagher, and E. Arenholz, *Phys. Rev. Lett.* **96**, 117207 (2006).
- [12] R. Nakane, J. Kondo, and M. Tanaka, *Jpn. J. Appl. Phys.* **46**, L755–L757 (2007).
- [13] A. M. Nazmul, T. Amemiya, Y. Shuto, S. Sugahara, and M. Tanaka, *Phys. Rev. Lett.* **95**, 017201 (2005).
- [14] I. Appelbaum, B. Huang, and D. J. Monsma, *Nature* **447**, 295–298 (2007).
- [15] K. Moon and P. Lyu, *Eur. Phys. J. B* **36**, 593–598 (2003).
- [16] C. A. Nolph, H. Liu, and P. Reinke, *Surface Science* **605**, L29–L32 (2011).
- [17] C. A. Nolph, K. R. Simov, H. Liu, and P. Reinke, *J. Phys. Chem. C* **114**, 19727–19733 (2010).
- [18] C. Nolph, E. Vescovo, and P. Reinke, *Appl. Surf. Sci.* **255**, 7642–7646 (2009).
- [19] K. Oura, V. G. Lifshits, A. A. Saranin, A. V. Zotov, and M. Katayama, *Surface Science* (Springer-Verlag Berlin Heidelberg, Germany, 2003).
- [20] E. A. Wood, *Journal of Applied Physics* **35**, 1306–1312 (1964).
- [21] D. J. Chadi, *J. Vac. Sci. Technol.* **16**, 1290–1296 (1979).
- [22] D. J. Chadi, *Phys. Rev. Lett.* **43**, 43–47 (1979).
- [23] J. Nogami, B. Liu, M. Katkov, C. Ohbuchi, and N. Birge, *Phys. Rev. B* **63**, (2001).
- [24] J. H. G. Owen, K. Miki, H. Koh, H. W. Yeom, and D. R. Bowler, *Phys. Rev. Lett.* **88**, 226104 (2002).
- [25] H. Omi and T. Ogino, *Appl. Phys. Lett.* **71**, 2163 (1997).
- [26] D. Lee and S. Kim, *Appl. Phys. Lett.* **82**, 2619 (2003).
- [27] A. Baski, K. Saoud, and K. Jones, *Appl. Surf. Sci.* **182**, 216–222 (2001).
- [28] B. C. Harrison and J. J. Boland, *Surf. Sci.* **594**, 93–98 (2005).
- [29] Y. Chen, D. A. A. Oehlberg, and R. S. Williams, *J. Appl. Phys.* **91**, 3213 (2002).
- [30] D. K. Lim, S.-S. Bae, J. Choi, D. Lee, D. E. Sung, S. Kim, J. K. Kim, H. W. Yeom, and H. Lee, *J. Chem. Phys.* **128**, 094701 (2008).
- [31] N. Frangis, J. Van Landuyt, G. Kaltsas, A. Travlos, and A. G. Nassiopoulou, *Journal of Crystal Growth* **172**, 175–182 (1997).
- [32] W. Zhou, S. Wang, T. Ji, Y. Zhu, Q. Cai, and X. Hou, *Jpn. J. Appl. Phys.* **45**, 2059–2062 (2006).

- [33] J. H. G. Owen, K. Miki, and D. R. Bowler, *Journal of Materials Science* **41**, 4568–4603 (2006).
- [34] C. Preinesberger, S. Vandre, T. Kalka, and M. Dähne-Prietsch, *J. Phys. D Appl. Phys.* **31**, L43 (1998).
- [35] J. Nogami, S. Park, and C. F. Quate, *Phys. Rev. B* **36**, 6221–6224 (1987).
- [36] K. Miki, D. R. Bowler, J. H. G. Owen, G. A. D. Briggs, and K. Sakamoto, *Phys. Rev. B* **59**, 14868 (1999).
- [37] H. Yeom, Y. Kim, E. Lee, K.-D. Ryang, and P. Kang, *Phys. Rev. Lett.* **95**, (2005).
- [38] N. Zaki, D. Potapenko, P. Johnson, and R. Osgood, *Physical Review B* **80**, (2009).
- [39] S.-C. Wang, M. B. Yilmaz, K. R. Knox, N. Zaki, J. I. Dadap, T. Valla, P. D. Johnson, and R. M. Osgood, *Phys. Rev. B* **77**, 115448 (2008).
- [40] P. Gambardella, M. Blanc, H. Brune, K. Kuhnke, and K. Kern, *Phys. Rev. B* **61**, 2254 (2000).
- [41] A. Dallmeyer, C. Carbone, W. Eberhardt, C. Pampuch, O. Rader, W. Gudat, P. Gambardella, and K. Kern, *Phys. Rev. B* **61**, 5133–5136 (2000).
- [42] V. Scheuch, B. Voigtländer, and H. P. Bonzel, *Surf. Sci.* **372**, 71–82 (1997).
- [43] A. M. Andrews, J. S. Speck, A. E. Romanov, M. Bobeth, and W. Pompe, *Journal of Applied Physics* **91**, 1933–1943 (2002).
- [44] H. Lüth, *Solid Surfaces, Interfaces and Thin Films*, 4th, rev. and extended ed. (Springer, 2001).
- [45] A. Rastelli and H. von Känel, *Surface Science* **515**, L493–L498 (2002).
- [46] G. Medeiros-Ribeiro, A. M. Bratkovski, T. I. Kamins, D. A. A. Ohlberg, and R. S. Williams, *Science* **279**, 353–355 (1998).
- [47] H. Munekata, H. Ohno, S. von Molnar, A. Segmüller, L. L. Chang, and L. Esaki, *Phys. Rev. Lett.* **63**, 1849 (1989).
- [48] H. Ohno, H. Munekata, S. von Molnár, and L. L. Chang, *Journal of Applied Physics* **69**, 6103–6108 (1991).
- [49] H. Ohno, H. Munekata, T. Penney, S. von Molnár, and L. L. Chang, *Phys. Rev. Lett.* **68**, 2664–2667 (1992).
- [50] K. C. Ku, S. J. Potashnik, R. F. Wang, S. H. Chun, P. Schiffer, N. Samarth, M. J. Seong, A. Mascarenhas, E. Johnston-Halperin, R. C. Myers, A. C. Gossard, and D. D. Awschalom, *Applied Physics Letters* **82**, 2302–2304 (2003).
- [51] D. Chiba, K. Takamura, F. Matsukura, and H. Ohno, *Applied Physics Letters* **82**, 3020–3022 (2003).
- [52] Y. F. Chen, W. N. Lee, J. H. Huang, T. S. Chin, R. T. Huang, F. R. Chen, J. J. Kai, K. Aravind, I. N. Lin, and H. C. Ku, *J. Vac. Sci. Technol. B* **23**, 1376 (2005).
- [53] Y. F. Chen, J. H. Huang, W. N. Lee, T. S. Chin, R. T. Huang, F. R. Chen, J. J. Kai, and H. C. Ku, *Appl. Phys. Lett.* **90**, 022505 (2007).
- [54] Y. Ohno, D. K. Young, B. Beschoten, F. Matsukura, H. Ohno, and D. D. Awschalom, *Nature* **402**, 790–792 (1999).
- [55] H. Ohno, D. Chiba, F. Matsukura, T. Omiya, E. Abe, T. Dietl, Y. Ohno, and K. Ohtani, *Nature* **408**, 944–946 (2000).
- [56] S. Cho, S. Choi, S. C. Hong, Y. Kim, J. B. Ketterson, B.-J. Kim, Y. C. Kim, and J.-H. Jung, *Phys. Rev. B* **66**, 033303 (2002).
- [57] Y. D. Park, A. T. Hanbicki, S. C. Erwin, C. S. Hellberg, J. M. Sullivan, J. E. Mattson, T. F. Ambrose, A. Wilson, G. Spanos, and B. T. Jonker, *Science* **295**, 651–654 (2002).

- [58] T. B. Massalski, editor, *Binary Alloy Phase Diagrams*, 2nd ed. (ASM International, 1990).
- [59] F. Xiu, Y. Wang, J. Kim, A. Hong, J. Tang, A. P. Jacob, J. Zou, and K. L. Wang, *Nat. Mater.* **9**, 337–344 (2010).
- [60] F. Xiu, Y. Wang, J. Kim, P. Upadhyaya, Y. Zhou, X. Kou, W. Han, R. K. Kawakami, J. Zou, and K. L. Wang, *ACS Nano* **4**, 4948–4954 (2010).
- [61] N. Pinto, L. Morresi, M. Ficcadenti, R. Murri, F. D’Orazio, F. Lucari, L. Boarino, and G. Amato, *Phys. Rev. B* **72**, 165203–7 (2005).
- [62] A. P. Li, J. F. Wendelken, J. Shen, L. C. Feldman, J. R. Thompson, and H. H. Weitering, *Phys. Rev. B* **72**, 195205 (2005).
- [63] T.-G. Le, D. N. H. Nam, M.-T. Dau, T. K. P. Luong, N. V. Khiem, V. L. Thanh, L. Michez, and J. Derrien, *Journal of Physics: Conference Series* **292**, 012012 (2011).
- [64] M. Jamet, A. Barski, T. Devillers, V. Poydenot, R. Dujardin, P. Bayle-Guillevaud, J. Rothman, E. Bellet-Amalric, A. Marty, J. Cibert, R. Mattana, and S. Tatarenko, *Nat Mater* **5**, 653–659 (2006).
- [65] T. Devillers, M. Jamet, A. Barski, V. Poydenot, P. Bayle-Guillevaud, E. Bellet-Amalric, S. Cherifi, and J. Cibert, *Phys. Rev. B* **76**, 205306 (2007).
- [66] S. Tardif, V. Favre-Nicolin, F. Lançon, E. Arras, M. Jamet, A. Barski, C. Porret, P. Bayle-Guillevaud, P. Pochet, T. Devillers, and M. Rovezzi, *Phys. Rev. B* **82**, 104101 (2010).
- [67] F. Xiu, Y. Wang, K. Wong, Y. Zhou, X. Kou, J. Zou, and K. L. Wang, *Nanotechnology* **21**, 255602 (2010).
- [68] A. Jain, M. Jamet, A. Barski, T. Devillers, C. Porret, P. Bayle-Guillevaud, S. Gambarelli, V. Maurel, and G. Desfonds, *Applied Physics Letters* **97**, 202502 (2010).
- [69] J. Deng, Y. Tian, S. Yan, Q. Cao, G. Liu, Y. Chen, L. Mei, G. Ji, and Z. Zhang, *Journal of Applied Physics* **104**, 013905 (2008).
- [70] L. Zeng, J. Cao, E. Helgren, J. Karel, E. Arenholz, L. Ouyang, D. Smith, R. Wu, and F. Hellman, *Phys. Rev. B* **82**, (2010).
- [71] L. Ottaviano, A. Continenza, G. Profeta, G. Impellizzeri, A. Irrera, R. Gunnella, and O. Kazakova, *Phys. Rev. B* **83**, 134426 (2011).
- [72] F. Xiu, Y. Wang, X. Kou, P. Upadhyaya, Y. Zhou, J. Zou, and K. L. Wang, *Journal of the American Chemical Society* **132**, 11425–11427 (2010).
- [73] G. Binnig and H. Rohrer, *Helv. Phys. Acta* **55**, 726–735 (1982).
- [74] G. Binnig and H. Rohrer, *Rev. Mod. Phys.* **59**, 615–625 (1987).
- [75] D. M. Eigler and E. K. Schweizer, , Published Online: 05 April 1990; | Doi:10.1038/344524a0 **344**, 524–526 (1990).
- [76] J. A. Strosio and D. M. Eigler, *Science* **254**, 1319–1326 (1991).
- [77] L. Bartels, G. Meyer, and K.-H. Rieder, *Phys. Rev. Lett.* **79**, 697–700 (1997).
- [78] J. W. Lyding, T. -C Shen, J. S. Hubacek, J. R. Tucker, and G. C. Abeln, *Applied Physics Letters* **64**, 2010–2012 (1994).
- [79] E. T. Foley, A. F. Kam, J. W. Lyding, and P. Avouris, *Phys. Rev. Lett.* **80**, 1336–1339 (1998).
- [80] S. Alavi and T. Seideman, *The Journal of Chemical Physics* **115**, 1882–1890 (2001).
- [81] G. Binnig, H. Rohrer, C. Gerber, and E. Weibel, *Phys. Rev. Lett.* **50**, 120–123 (1983).
- [82] C. J. Chen, *Introduction to Scanning Tunneling Microscopy*, 2nd ed. (Oxford University Press, New York, 2008).

- [83] E. Meyer, H. J. Hug, and R. Bennewitz, *Scanning Probe Microscopy: The Lab on a Tip*, 1st ed. (Springer, 2003).
- [84] J. Tersoff and D. R. Hamann, Phys. Rev. Lett. **50**, 1998–2001 (1983).
- [85] J. Tersoff and D. R. Hamann, Phys. Rev. B **31**, 805–813 (1985).
- [86] R. M. Feenstra, J. A. Stroscio, J. Tersoff, and A. P. Fein, Phys. Rev. Lett. **58**, 1192–1195 (1987).
- [87] R. Wiesendanger, *Scanning Probe Microscopy and Spectroscopy: Methods and Applications* (Cambridge University Press, Great Britain, 1994).
- [88] B. S. Swartzentruber, J. Vac. Sci. Technol. A **7**, 2901 (1989).
- [89] K. Hata, T. Kimura, S. Ozawa, and H. Shigekawa, J. Vac. Sci. Technol. A **18**, 1933–1936 (2000).
- [90] E. Beaurepaire, H. Bulou, F. Scheurer, and K. Jean-Paul, editors, *Magnetism and Synchrotron Radiation*, 1st ed. (Springer Heidelberg Dordrecht London New York, 2010).
- [91] C. T. Chen, Y. U. Idzerda, H.-J. Lin, N. V. Smith, G. Meigs, E. Chaban, G. H. Ho, E. Pellegrin, and F. Sette, Phys. Rev. Lett. **75**, 152 (1995).
- [92] P. Carra, B. T. Thole, M. Altarelli, and X. Wang, Phys. Rev. Lett. **70**, 694–697 (1993).
- [93] B. T. Thole, P. Carra, F. Sette, and G. van der Laan, Phys. Rev. Lett. **68**, 1943–1946 (1992).
- [94] E. Goering, Philosophical Magazine **85**, 2895–2911 (2005).
- [95] T. Saito, T. Katayama, T. Ishikawa, M. Yamamoto, D. Asakura, and T. Koide, Appl. Phys. Lett. **91**, 262502 (2007).
- [96] Y. Yonamoto, T. Yokoyama, K. Amemiya, D. Matsumura, S. Kitagawa, Y. Hamada, T. Koide, and T. Ohta, Journal of the Physical Society of Japan **71**, 607–612 (2002).
- [97] S. Foner, Review of Scientific Instruments **30**, 548–557 (1959).
- [98] G. W. Oosterhout, Applied Scientific Research **6**, 101–104 (1957).
- [99] B. D. Cullity and C. D. Graham, *Introduction to Magnetic Materials*, 2nd ed. (John Wiley & Sons, New Jersey, 2011).
- [100] A. Ney, T. Kammermeier, V. Ney, K. Ollefs, and S. Ye, Journal of Magnetism and Magnetic Materials **320**, 3341–3346 (2008).
- [101] M. Ohring, *Materials Science of Thin Films*, 2nd ed. (Academic Press, San Diego, 2002).
- [102] C. C. Chang, Surface Science **25**, 53–79 (1971).
- [103] H. Liu and P. Reinke, Surf. Sci. **602**, 986–992 (2008).
- [104] K. R. Simov, C. A. Nolph, and P. Reinke, J. Phys. Chem. C **116**, 1670–1678 (2011).
- [105] M. A. Albao, M. M. R. Evans, J. Nogami, D. Zorn, M. S. Gordon, and J. W. Evans, Phys. Rev. B **72**, 035426 (2005).
- [106] P. Kocán, P. Sobotík, I. Oscaront’ádal, M. Setvín, and S. Haviar, Phys. Rev. E **80**, 061603 (2009).
- [107] G. Brocks, P. J. Kelly, and R. Car, Phys. Rev. Lett. **70**, 2786 (1993).
- [108] M. R. Krause, A. J. Stollenwerk, M. Licurse, and V. P. LaBella, Appl. Phys. Lett. **91**, 041903 (2007).
- [109] J. Wang, M. Hirai, M. Kusaka, and M. Iwami, Appl. Surf. Sci. **113-114**, 53–56 (1997).
- [110] M. D. Abramoff, P. J. Magelhaes, and S. J. Ram, Biophotonics International **11**, 36–42 (2004).
- [111] I. Horcas, R. Fernandez, J. M. Gómez-Rodríguez, J. Colchero, J. Gómez-Herrero, and A. M. Baro, Rev. Sci. Instrum. **78**, 013705 (2007).

- [112] H. J. W. Zandvliet, H. K. Louwsma, P. E. Hegeman, and B. Poelsema, *Phys. Rev. Lett.* **75**, 3890 (1995).
- [113] J.-Y. Koo, J.-Y. Yi, C. Hwang, D.-H. Kim, S. Lee, and D.-H. Shin, *Phys. Rev. B* **52**, 17269 (1995).
- [114] A. P. Horsfield, S. D. Kenny, and H. Fujitani, *Phys. Rev. B* **64**, 245332 (2001).
- [115] P. Blaha, K. Schwarz, G. K. H. Madsen, D. Kvasnicka, and J. Luitz, *WIEN2k, an Augmented Plan Wave + Local Orbitals Program for Calculating Crystal Properties* (Techn. Univ. Wien, Austria, 2001).
- [116] H. J. W. Zandvliet, H. B. Elswijk, E. J. van Loenen, and D. Dijkkamp, *Phys. Rev. B* **45**, 5965 (1992).
- [117] H. J. W. Zandvliet, *Rev. Mod. Phys.* **72**, 593 (2000).
- [118] M. Hortamani, H. Wu, P. Kratzer, and M. Scheffler, *Phys. Rev. B* **74**, 205305–10 (2006).
- [119] A. Horsfield, E. Akhmatkaya, R. Nobes, J. Andzelm, G. Fitzgerald, and N. Govind, *Phys. Rev. B* **66**, 085309 (2002).
- [120] R. J. Hamers and U. K. Kohler, *J. Vac. Sci. Technol. A* **7**, 2854–2859 (1989).
- [121] P. Bedrossian and T. Klitsner, *Phys. Rev. Lett.* **68**, 646 (1992).
- [122] F.-K. Men, A. R. Smith, K.-J. Chao, Z. Zhang, and C.-K. Shih, *Phys. Rev. B* **52**, R8650 (1995).
- [123] N. Kitamura, B. S. Swartzentruber, M. G. Lagally, and M. B. Webb, *Phys. Rev. B* **48**, 5704 (1993).
- [124] C. Pearson, B. Borovsky, M. Krueger, R. Curtis, and E. Ganz, *Phys. Rev. Lett.* **74**, 2710 (1995).
- [125] B. S. Swartzentruber and M. Schacht, *Surf. Sci.* **322**, 83–89 (1995).
- [126] K. H. Kim, S. W. Han, J. D. Lee, J. J. Lee, K. J. Kim, B. S. Kim, S. C. Wi, S. S. Lee, G. Kim, and J. S. Kang, *J. Korean Phys. Soc.* **48**, 931–938 (2006).
- [127] A. Kumar, M. Tallarida, M. Hansmann, U. Starke, and K. Horn, *J. Phys. D Appl. Phys.* **37**, 1083–1090 (2004).
- [128] H. Lippitz, J. J. Paggel, and P. Fumagalli, *Surf. Sci.* **575**, 307–312 (2005).
- [129] H. Wu, M. Hortamani, P. Kratzer, and M. Scheffler, *Phys. Rev. Lett.* **92**, 237202 (2004).
- [130] M. R. Krause, A. J. Stollenwerk, J. Reed, V. P. LaBella, M. Hortamani, P. Kratzer, and M. Scheffler, *Phys. Rev. B* **75**, 205326–5 (2007).
- [131] J.-T. Wang, C. Chen, E. Wang, and Y. Kawazoe, *Phys. Rev. Lett.* **105**, 116102 (2010).
- [132] H. J. W. Zandvliet, H. B. Elswijk, E. J. van Loenen, and I. S. T. Tsong, *Phys. Rev. B* **46**, 7581 (1992).
- [133] H. J. W. Zandvliet, *Surf. Sci.* **377-379**, 1–6 (1997).
- [134] E. Kim and C. Chen, *Phys. Lett. A* **301**, 484–489 (2002).
- [135] L. Liu, J. Yu, and J. W. Lyding, *Appl. Phys. Lett.* **78**, 386–388 (2001).
- [136] J. K. Garleff, M. Wenderoth, R. G. Ulbrich, C. Surgers, H. v. Lohneysen, and M. Rohlfing, *Phys. Rev. B* **76**, 125322–5 (2007).
- [137] G. W. Brown, H. Grube, and M. E. Hawley, *Phys. Rev. B* **70**, 121301 (2004).
- [138] G. Brown, B. Uberuaga, H. Grube, M. Hawley, S. Schofield, N. Curson, M. Simmons, and R. Clark, *Phys. Rev. B* **72**, 195323 (2005).
- [139] M. Nishizawa, L. Bolotov, and T. Kanayama, *Jpn. J. Appl. Phys.* **2** **44**, L1436–L1438 (2005).
- [140] A. M. Yakunin, A. Y. Silov, P. M. Koenraad, J. H. Wolter, W. Van Roy, J. De Boeck, J.-M. Tang, and M. E. Flatté, *Phys. Rev. Lett.* **92**, 216806 (2004).

- [141] J.-M. Jancu, J.-C. Girard, M. O. Nestoklon, A. Lemaitre, F. Glas, Z. Z. Wang, and P. Voisin, *Phys. Rev. Lett.* **101**, 196801–4 (2008).
- [142] L. Liu, J. Yu, and J. W. Lyding, *IEEE T. Nanotechnol.* **1**, 176–183 (2002).
- [143] M. Nishizawa, L. Bolotov, and T. Kanayama, *Appl. Phys. Lett.* **90**, 122118–3 (2007).
- [144] J. F. Xu, P. M. Thibado, C. Awo-Affouda, F. Ramos, and V. P. LaBella, *J. Vac. Sci. Technol. B* **25**, 1476–1480 (2007).
- [145] T. Dietl, H. Ohno, and F. Matsukura, *Phys. Rev. B* **63**, 195205 (2001).
- [146] X. Luo, S. B. Zhang, and S.-H. Wei, *Phys. Rev. B* **70**, 033308 (2004).
- [147] L. Morresi, J. P. Ayoub, N. Pinto, M. Ficcadenti, R. Murri, A. Ronda, I. Berbezier, F. D’Orazio, and F. Lucari, *Surf. Sci.* **601**, 2632–2635 (2007).
- [148] Y. Wang, J. Zou, Z. M. Zhao, X. H. Han, X. Y. Zhou, and K. L. Wang, *J. Appl. Phys.* **103**, 066104 (2008).
- [149] N. Peng, C. Jeynes, M. J. Bailey, D. Adikaari, V. Stolojan, and R. P. Webb, *Nucl. Instrum. Meth. B* **267**, 1623–1625 (2009).
- [150] M. Ogawa, X. Han, Z. Zhao, Y. Wang, K. L. Wang, and J. Zou, *J. Cryst. Growth* **311**, 2147–2150 (2009).
- [151] J. J. Yeh and I. Lindau, *Atom. Data Nucl. Data* **32**, 1–155 (1985).
- [152] E. Vescovo, H.-J. Kim, Q.-Y. Dong, G. Nintzel, D. Carlson, S. Hulbert, and N. V. Smith, *Synchrotron Radiation News* **12**, 10 (1999).
- [153] K. Levenberg, *Q. Appl. Math.* **2**, 164 (1944).
- [154] D. W. Marquardt, *SIAM J. Appl. Math.* **11**, 431 (1963).
- [155] S. Doniach and M. Sunjic, *J. Phys. C* **3**, 285 (1970).
- [156] D. A. Shirley, *Phys. Rev. B* **5**, 4709 (1972).
- [157] U. A. Effner, D. Badt, J. Binder, T. Bertrams, A. Brodde, C. Lunau, H. Neddermeyer, and M. Hanbücken, *Surf. Sci.* **277**, 207–219 (1992).
- [158] Y. Enta, S. Suzuki, and S. Kono, *Phys. Rev. Lett.* **65**, 2704 (1990).
- [159] F. J. Himpsel, F. R. McFeely, A. Taleb-Ibrahimi, J. A. Yarmoff, and G. Hollinger, *Phys. Rev. B* **38**, 6084 (1988).
- [160] E. Magnano, E. Carleschi, A. Nicolaou, T. Pardini, M. Zangrando, and F. Parmigiani, *Surf. Sci.* **600**, 3932–3937 (2006).
- [161] A. von dem Borne, R. L. Johnson, B. Sonntag, M. Talkenberg, A. Verweyen, P. Wernet, J. Schulz, K. Tiedtke, C. Gerth, B. Obst, P. Zimmermann, and J. E. Hansen, *Phys. Rev. A* **62**, 052703 (2000).
- [162] A. Irizawa, A. Yamasaki, M. Okazaki, S. Kasai, A. Sekiyama, S. Imada, S. Suga, E. Kulatov, H. Ohta, and T. Nanba, *Solid State Commun.* **124**, 1–5 (2002).
- [163] M. Oku, S. Suzuki, N. Ohtsu, T. Shishido, and K. Wagatsuma, *Appl. Surf. Sci.* **254**, 5141–5148 (2008).
- [164] L. S. O. Johansson, R. I. G. Uhrberg, P. Mårtensson, and G. V. Hansson, *Phys. Rev. B* **42**, 1305 (1990).
- [165] E. L. Bullock, R. Gunnella, L. Patthey, T. Abukawa, S. Kono, C. R. Natoli, and L. S. O. Johansson, *Phys. Rev. Lett.* **74**, 2756 (1995).
- [166] E. Landemark, C. J. Karlsson, Y. C. Chao, and R. I. G. Uhrberg, *Phys. Rev. Lett.* **69**, 1588–1591 (1992).
- [167] E. Carleschi, E. Magnano, M. Zangrando, F. Bondino, A. Nicolaou, F. Carbone, D. Van der Marel, and F. Parmigiani, *Surf. Sci.* **601**, 4066–4073 (2007).

- [168] H. Sugawara, A. Kakizaki, I. Nagakura, and T. Ishii, *J. Phys. F Met.* **12**, 2929–2936 (1982).
- [169] L. Zhang and D. G. Ivey, *J. Mater. Res.* **6**, 1518–1531 (1991).
- [170] C. Anandan, *Appl. Surf. Sci.* **89**, 57–61 (1995).
- [171] N. Benouattas, A. Mosser, and A. Bouabellou, *Appl. Surf. Sci.* **252**, 7572–7577 (2006).
- [172] S. Iida and S. Abe, *Appl. Surf. Sci.* **78**, 141–146 (1994).
- [173] S. Kennou, S. Ladas, M. G. Grimaldi, T. A. Nguyen Tan, and J. Y. Veuillen, *Appl. Surf. Sci.* **102**, 142–146 (1996).
- [174] P. Klapetek and D. Nečas, *Gwyddion* (n.d.).
- [175] I. Goldfarb, J. H. G. Owen, P. T. Hayden, D. R. Bowler, K. Miki, and G. A. D. Briggs, *Surf. Sci.* **394**, 105–118 (1997).
- [176] U. Köhler, O. Jusko, B. Müller, M. H. Hoegen, and M. Pook, *Ultramicroscopy* **42-44**, 832–837 (1992).
- [177] Y. Fujikawa, K. Akiyama, T. Nagao, T. Sakurai, M. G. Lagally, T. Hashimoto, Y. Morikawa, and K. Terakura, *Phys. Rev. Lett.* **88**, 176101 (2002).
- [178] T. Hashimoto, Y. Morikawa, Y. Fujikawa, T. Sakurai, M. G. Lagally, and K. Terakura, *Surface Science* **513**, L445–L450 (2002).
- [179] F. Montalenti, D. B. Migas, F. Gamba, and L. Miglio, *Phys. Rev. B* **70**, 245315 (2004).
- [180] L. Huang, G.-H. Lu, F. Liu, and X. G. Gong, *Surface Science* **601**, 3067–3072 (2007).
- [181] C. Zeng, Z. Zhang, K. van Benthem, M. F. Chisholm, and H. H. Weitering, *Phys. Rev. Lett.* **100**, 066101–4 (2008).
- [182] Y. Fujikawa, T. Sakurai, and M. G. Lagally, *Applied Surface Science* **252**, 5244–5248 (2006).
- [183] J.-S. Kang, G. Kim, H. J. Lee, D. H. Kim, H. S. Kim, J. H. Shim, S. Lee, H. Lee, J.-Y. Kim, B. H. Kim, and B. I. Min, *Phys. Rev. B* **77**, 035121 (2008).
- [184] W. M. Haynes, editor, *Handbook of Chemistry and Physics*, Online ed. (CRC Press, 2011).
- [185] S. Tardif, I.-S. Yu, T. Devillers, M. Jamet, S. Cherifi, J. Cibert, A. Barski, P. Bayle-Guillemaud, and E. Bellet-Amalric, in *Proceedings of SPIE* (San Diego, CA, USA, 2008), p. 703615–703615–10.
- [186] Y. Yonamoto, T. Yokoyama, K. Amemiya, D. Matsumura, and T. Ohta, *Phys. Rev. B* **63**, 214406 (2001).
- [187] M. C. Richter, P. De Padova, C. Quaresima, P. Perfetti, R. Brochier, V. Ilakovac, O. Heckmann, L. Lechevallier, M. Zerrouki, C. Teodorescu, C. S. Fadley, N. Hamdan, and K. Hricovini, *Journal of Alloys and Compounds* **362**, 41–47 (2004).